

13427
NATIONAL LIBRARY
OTTAWA



BIBLIOTHÈQUE NATIONALE
OTTAWA

NAME OF AUTHOR... *Donald Alexander Johnston*
TITLE OF THESIS... *Travelling Wave and
Resonant Microwave Heating
Applicator Design*
UNIVERSITY... *University of Alberta*
DEGREE FOR WHICH THESIS WAS PRESENTED... *Ph.D.*
YEAR THIS DEGREE GRANTED... *Fall 1972*

Permission is hereby granted to THE NATIONAL LIBRARY
OF CANADA to microfilm this thesis and to lend or sell copies
of the film.

The author reserves other publication rights, and
neither the thesis nor extensive extracts from it may be
printed or otherwise reproduced without the author's
written permission.

(Signed) *Donald A. Johnston*

PERMANENT ADDRESS:

*# 306 - 111 30 - 57 Ave
Edmonton Alta
T6H 0Z8*

DATED *Sept 28* 1972

NL-91 (10-68)

THE UNIVERSITY OF ALBERTA

TRAVELLING WAVE AND RESONANT MICROWAVE HEATING APPLICATOR DESIGN

by



DONALD ALEXANDER JOHNSTON

A THESIS

SUBMITTED TO THE FACULTY OF GRADUATE STUDIES AND RESEARCH
IN PARTIAL FULFILLMENT OF THE REQUIREMENTS FOR THE DEGREE
OF DOCTOR OF PHILOSOPHY

DEPARTMENT OF ELECTRICAL ENGINEERING

EDMONTON, ALBERTA

FALL 1972

THE UNIVERSITY OF ALBERTA
FACULTY OF GRADUATE STUDIES AND RESEARCH

The undersigned certify that they have read, and recommend to the Faculty of Graduate Studies and Research, for acceptance, a thesis entitled Travelling Wave and Resonant Microwave Heating Applicator Design submitted by Donald Alexander Johnston in partial fulfillment of the requirements for the degree of Doctor of Philosophy.

W. Easton
.....
Supervisor
Wayne Tingo
.....
P. Harkin
.....
J. Vaneldik
.....
Alvan Hoegh
.....
External Examiner

Date... *August 31st 1972*

ABSTRACT

The dominant problems of travelling wave and resonant microwave heating applicators are uneven heating and reflected power respectively, although both problems occur with either type.

It is shown that a travelling wave applicator using the TEM rather than the more common TE_{10} mode gives, in principle, improved uniformity of heating for a wide range of web materials. Wave impedance and attenuation functions for the TEM rectangular structure are derived using the method of moments. The results show that a ten-to-one range of attenuation control is possible by varying the gaps between the sides and the centre conductor. This also permits control of reflected power and leakage. Efficiency and uniformity of heating in a batch-heated web in a travelling wave applicator are analyzed, using the initial equilibrium temperature of the web as an independent variable. Vapor pressure, standing wave effects and changes in wave velocity are included. It is shown that batch heating theory can be used to give bounds of inhomogeneity in moving wet webs. This permits the choice of an attenuation factor.

Reactive coupling of energy into resonant structures is analyzed. Reflections result when waves in the coupling element and the cavity travel in or near synchronism. This type of reflections, as well as the heating inhomogeneity, are reduced by a new slow wave coupler design. A cavity applicator providing multimode operation in a small volume and utilizing a system of interconnected TE_{m0n} resonators is designed. Tests with the slow wave coupler indicate that the frequency pulling effect can be minimized.

ACKNOWLEDGEMENT

I wish to thank Dr. W.A.G. Voss for his encouragement and assistance during the course of this project. The assistance of Dr. W.R. Tinga with several of its aspects is also thankfully acknowledged.

I am indebted to Mr. E. Buck and the technical staff of the Electrical Engineering Department for constructing the test structures and to Mr. A. Huizinga for helping to test them.

The assistance of the Toronto laboratory of Reichhold Chemicals (Can.) Ltd. with plasma cavities, of Mr. D. Warwaruk with the web drying computer program and of Mr. R. Rajotte in providing an opportunity to test the slow wave coupler in practice are all very much appreciated.

To Mr. H. Chaurasia and Mr. R. Tetarenko, I am grateful for many helpful discussions and for assistance with the manuscript. Mrs. B. Huizinga's forbearance in typing the manuscript is also appreciated.

The National Research Council of Canada provided a bursary and supported this project through Grant No. 2272, "Applications for High Power Microwave". To NRC and to the Electrical Engineering Department of the university I am grateful for the facilities provided.

I owe special thanks and deep gratitude to my wife, Mary, for her unfailing patience, encouragement and help.

TABLE OF CONTENTS

<u>CHAPTER 1</u>	MICROWAVE POWER APPLICATORS	1
	1.1 Introduction	1
	1.2 Applicator Parameters	7
<u>CHAPTER 2</u>	ATTENUATION CONTROL IN TRAVELLING WAVE APPLICATORS	12
	2.1 Conventional Techniques	12
	2.2 Circular Coaxial Applicator	17
	2.3 Variable Cross-Section TEM Applicators	20
<u>CHAPTER 3</u>	NUMERICAL ANALYSIS OF THE RECTANGULAR TEM APPLICATOR	24
	3.1 Characteristics of the Rectangular Structure	24
	3.2 A Mathematical Technique for TEM Structures	26
	(a) The Moment Method	26
	(b) Use of Image Charges	32
	(c) Calculation of the Average Voltage	34
	(d) Correction of Charge Placement	37
	(e) Calculation of Applicator Parameters	42
	3.3 Results	44
<u>CHAPTER 4</u>	INHOMOGENEITIES AND ATTENUATION IN TRAVELLING WAVE APPLICATORS	62
	4.1 Drying of Wet Webs	63
	4.2 Energy Deposition and Drying for Very Wet Webs	65
	(a) Power Applied	65
	(b) Drying Rate	66
	(c) Temperature Changes	67

		VI
	(d) Normalized Drying Time	69
	(e) Propagation Constant	71
	(f) Capacitance and Characteristic Impedance	71
	(g) Distributed Reflections	72
	(h) Finite Difference Equations for Reflections	78
	(i) Finite Difference Time Response of the System	74
	4.3 Exponential Heating Model and Meanderline Applicators	75
	4.4 Experimental Results	78
	4.5 Computer Results for Very Web Webs	81
CHAPTER 5	CONTROL OF REFLECTIONS FROM RESONANT APPLICATORS	89
	5.1 Microwave Heating in Resonant Cavities	89
	5.2 Reactance Coupling Theory	93
	(a) Coupling Capacitance Model	93
	(b) Results of Model	95
	(c) Distributed Coupling	98
	5.3 Results of Slow Wave Coupling	103
	5.4 Conclusions and Practical Design Considerations	110
CHAPTER 6	A SMALL MULTIMODE CAVITY FOR RODLIKE LOADS	113
	6.1 Microwave Heating of Rodlike Loads	113
	6.2 Metal Plates in a Rectangular Cavity	117
	6.3 Experimental Cavity	121
	6.4 Application of the Vaned Rectangular Cavity	125

<u>CHAPTER 7</u>	CONCLUSIONS	127
	References	129
	Appendix I - Limit of Validity of the Perturbation Analysis	136
	Appendix II - The Twin-line Applicator	140
	Appendix III - Correction for Line Charge Approximation	147

LIST OF TABLES

Table 4.1	Experimental Check on Attenuation Inhomogeneity	81
Table 5.1	Optimum Coupling Frequencies	103
Table 6.1	Single Resonator Resonances	123
Table 6.2	Modes per 100 MHz	123
Table 6.3	Frequency Bands for Test Cavity	123
Table 6.4	Correction for Strip Width	148

LIST OF FIGURES

Figure 1.1	Cross-section of Web in Applicators	11
Figure 2.1	Cross-section of TE_{10} Applicator	12
Figure 2.2	Bottom Half of TE_{10} Applicator	13
Figure 2.3	Currents and Dimensions for TE_{10} Applicator	14
Figure 2.4	TEM Fringing Field Applicator	16
Figure 2.5	TE_{10} Fringing Field Applicator	16
Figure 2.6	Circular Coaxial Applicator	17
Figure 2.7	Attenuation of Simple Structures	19
Figure 2.8	Elliptical TEM Applicator	21
Figure 2.9	Rectangular TEM Applicator	22
Figure 3.1	Rectangular TEM Applicator	26
Figure 3.2	Line Charges	29
Figure 3.3	Strip Charge	30
Figure 3.4	Image Charges	32
Figure 3.5	Voltages in TEM Applicator	46
Figure 3.6	Electric Fields in TEM Applicator	47
Figure 3.7	Filling Factor Normalized to Centre Conductor	49
Figure 3.8	Power Concentration in Web Regions	51
Figure 3.9	Power Concentration Filling Factor Product	52
Figure 3.10	Spacing for Constant Impedance	53
Figure 3.11	Power Concentration at Constant Impedance	55
Figure 3.12	Chart for Web Power Absorption Factor - No Gap	56
Figure 3.13	Effect of Gap on Power Absorption in the Web	58
Figure 3.14	Rectangular TEM Applicator Design	60
Figure 4.1	Double Discontinuity	73

Figure 4.2	Distributed Reflections	73
Figure 4.3	Inhomogeneity and Efficiency vs Web Loading	79
Figure 4.4	Moisture Content at Time 0.25, 0.5, 0.75, 1.0 etc.	82
Figure 4.5	I, Difference Between Min and Max Moisture Content	85
Figure 5.1	Microwave Oven Cavity	91
Figure 5.2	Various Coupling Elements	91
Figure 5.3	Stripline Slow Wave Coupler	92
Figure 5.4	Lumped Circuit Model for a Single Mode	93
Figure 5.5	Distributed Coupling	99
Figure 5.6	Experimental Cavity for Thawing Live Organs	104
Figure 5.7	Reflections from Experimental Cavity	104
Figure 5.8	Reflections from Slow Wave Coupler and Probe	107
Figure 5.9	Reflections, Probe, Strap and Slow Wave Coupler	107
Figure 5.10	Slow Wave Coupler: TE_{10}	109
Figure 6.1	TM_{010} Threadline Applicator	113
Figure 6.2	TE_{103} Plasma Cavity	117
Figure 6.3	Vaned Multimode Test Cavity	118
Figure 6.4	Coupling-Induced Multimode Behavior	118
Figure 6.5	Coupled TE_{101} Cavities	119
Figure 6.6	Rat-race Resonator	120
Figure 6.7	Vaned Cavity with Slow Wave Coupling Structure	121
Figure A2.1	Twin-line Applicator	140
Figure A2.2	Twin-line Power Concentration Effect	144
Figure A2.3	Shielded Twin-line Structure	145
Figure A2.4	Test Setup for Twin-line Applicator	146
Figure A3.1	Potential Due to a Strip of Charge	147

TABLE OF SYMBOLS

a - large waveguide width, outer coaxial line diameter, cavity dimension, twin-line spacing	(m)
b - small waveguide width, small coaxial line diameter, cavity dimension, segment of strip	(m)
B - boundary of web cross-section	(m)
\hat{B} - magnetic flux density	(Webers/m ²)
B_{in} - input susceptance	(1/ Ω)
c - (subscript) coaxial line	...
c - rectangular TEM applicator gap	(m)
c - speed of light	(m/sec)
c_w - specific heat of water	(Joules/kg)
\underline{C} - capacitance of TEM structures	(F/m)
C, C' - capacitances, hypothetical tank circuit	(F)
d - rectangular TEM applicator gap, cavity dimensions	(m)
\hat{D} - electric flux density	(Coul/m ²)
D - coupling capacitance	(F)
e, \bar{e} , e_ϕ - error for numerical analysis	(dimensionless(-))
\hat{E} , \hat{E}_0 , \hat{E}_f , \hat{E}_r - electric field	(V/m)
$\langle E \rangle$ - RMS spatially averaged electric field	(V/m)
f - (subscript) forward	...
f - frequency, ($\omega/2\pi$)	(Hz)
F - filling factor	(-)
F_1, F_2 - correction factor	(-)
g - (subscript) guide	...
g_w - density of water	(kg/m ²)

G_{in} - input conductance	(1/ Ω)
G - effective web conductance	(1/ Ωm)
h - distance increment	(m)
$\hat{H}, \hat{H}_0, \hat{H}_f$ - magnetic field	(A/m)
$i, j, k, m, n, p, r, s,$ - dummy indices	...
in - (subscript) input	...
I, I_α - inhomogeneity	(-)
$j - \sqrt{-T}$...
k_c, k_e - z dependence of coupling	(-)
k - field ratio, perturbation validity	(-)
k_{dry} - drying constant	(kg/sec m ² Torr)
K_G - mass transfer coefficient	(kg/sec m ² Torr)
K_1, K_2, K_3, K_4 - coupling coefficients (Ch.5)	(-)
\ln - naperian logarithm	...
L_{ij} - matrix element	(1/Farads)
L - inductance	(Hy)
m - web water density	(kg/m)
M - mutual inductance	(Hy)
n - total number of line charges	(-)
\hat{n} - normal unit vector	(-)
N - total number of web intervals	(-)
N_e - energy in the electric field	(J)
o - (subscript) original or characteristic	...
p - normalized Laplace variable	(1/sec)
$P_a, P_{fm}, P_w, P_{fs}, P_{ft}$ - partial pressures	(Torr)
P, P_f, P_r - power	(W)
P_{fw} - forward power in the web	(W)

P_0 - magnetron output power	(W)
P_{web} - power dissipated in web	(W/m)
\underline{P} - power dissipated in web	(W/m ²)
q - line charge density	(Coul/m)
Q - heat in web (Ch.4)	(Joules/m)
Q, Q_r, Q_e, Q_w - quality factor of cavity	(-)
r - (subscript) relative (ϵ_r) or reflected (\hat{E}_r)	...
r - radial coordinate	(m)
\hat{r} - radial unit vector	(-)
R - resistance	(Ω)
R - Reynolds number	(-)
S - cross-section, applicator	(m ²)
ΔS - cross-section, web region	(m ²)
S - Schmidt number	(-)
t - time	(s)
t' - web thickness	(m)
TE, TM, TEM - mode types, transverse electric, transverse magnetic, transverse electromagnetic	...
u - normalized radian frequency (Ch.5)	(-)
u - exponent of Reynolds' number (Ch.4)	(-)
u_j - unit n element vector	(-)
u_p - constant, 1 Torr	(Torr)
v - exponent of Schmidt number	(-)
v_p - phase velocity	(m/sec)
V - applicator volume	(m ³)
ΔV - load volume	(m ³)

w - strip width (Ch.3), width of centre conductor	(m)
x, y, z, x', y', z' - Cartesian coordinates	(m)
x, x_e, x_o - drying variables (Sec.4.2d)	(-)
Y_{in} - Input admittance	(1/ Ω)
z, z' - location on path of wave	(m)
z_m - web width	(m)
z_p - period of applicator	(m)
z'_p - applicator spacing	(m)
Z - impedance	(Ω)
Z_0 - characteristic impedance	(Ω)
\underline{Z} - normalized Smith chart variable	(-)
α - real propagation constant	(nepers/m)
α - coupling coefficient	(-)
β - numerical analysis acceleration factor (Ch.3)	(-)
β - imaginary propagation constant	(1/m)
β - coupling coefficient (Ch.5)	(-)
γ - sign variable, numerical analysis	(-)
Γ - reflection coefficient	(-)
δ - Dirac delta function	(-)
ϵ - dielectric constant	(F/m)
ϵ_0 - Dielectric constant of free space	(F/m)
$\epsilon_r' \epsilon_r''$ - relative dielectric constant, real part, imaginary part	(-)
$\epsilon_r' \epsilon_r''$ - " " " of water	(-)
η - waveguide wave impedance	(Ω)
η_0 - free space wave impedance	(Ω)
θ - temperature	($^{\circ}$ C)
θ_e - equilibrium temperature	($^{\circ}$ C)

λ_w - latent heat of evaporation of water	(J/kg)
λ_o, λ_g - wavelength	(m)
μ_o, μ - permeability	(Hy/m)
ξ^2 - electric field concentration factor (shape)	(-)
ρ - water filling factor in web	(-)
σ - charge density	(Coul/m ²)
τ - Normalized time	(-)
ϕ - voltage	(V)
ϕ_{ave} - average voltage for paired charges	(V)
ϕ_{diff} - voltage difference for paired charges	(V)
ψ^2 - electric field concentration factor (reflections)	(-)
ω - (radian) frequency	(1/s)
ω_n - resonant frequency, n'th mode	(1/s)
ω_c - waveguide cutoff frequency	(1/s)

CHAPTER ONE

MICROWAVE POWER APPLICATORS

1.1. Introduction

Efficient, high power magnetrons were developed for World War II radar technology. The power carried by a radar beam could be felt as heat and it was natural to wonder if this effect could not be used. One of the first practical heating applications was a microwave oven⁽⁵⁹⁾. In the intervening years between the first oven and the present, further applications and methods have been developed, and a small industry based on the heating effect of microwaves has been established.

In its production, microwave energy is far removed from that stored in the original fuel, particularly in terms of the capital expenditure involved. The usual production cycle starts with conventional electric power which is rectified, giving a high voltage pulsating direct current and then converted to microwave power by a device such as a magnetron. Magnetron depreciation, at one to five cents per kWh⁽⁶⁹⁾, is presently the largest cost factor. Although efficiencies are high, over 75% for many power sources, some power is lost at each conversion step. For these reasons microwave power is expensive and its use must be justified by factors such as improved product quality, increased capacity of a manufacturing process, or elimination of a difficult heat transfer problem. The cost of microwave power is steadily decreasing as the technology in the industry improves.

The uses of microwave power are now quite diverse⁽³⁴⁾. For example, the food industry has employed it in drying potato chips, proofing doughnuts, cooking chickens and roasting nuts. Institutional outlets can use microwave ovens for quick reheating of almost any food, usually with better flavor than can be produced by any other method. The forest products industry has employed microwave power in drying wood, veneer, paper and special products such as baseball bats. Other uses by the plastics, photographic, auto, drug and other industries are listed in books⁽⁵¹⁾ and review articles^{(3),(69)} on the subject. There is now enough experience with microwave power that it is becoming evident that some standard techniques should be refined.

Industry has concentrated a major part of its development effort on power sources. Radar magnetrons were designed to produce large but brief pulses of power. The original task was to produce devices which generated a waveform carrying more average energy. The resulting rugged magnetrons have served well^{(12),(16)}, but there are still two problems associated with these power sources. The most important is the cost, and secondly, their sensitivity to loading conditions. The sensitivity to loading conditions can be improved by using devices such as klystrons and triodes in lieu of magnetrons. Efficiencies of 70% are quoted for klystrons, at power levels competitive with magnetrons^{(53),(29)}. Triodes do not operate well at frequencies comparable to the inverse of the electron transit time. Nevertheless they have been advocated, at efficiencies of about 25%, to overcome the loading problem⁽²⁸⁾.

At the present time there is public concern about the effect on the environment of still another form of escaping man-made energy. Government agencies now control designs for leakage of microwave radiation^{(4),(49),(58)}. Work on biological effects of microwaves⁽²²⁾ should help in setting exposure standards. This concern is timely for the industry because the heaviest usage of microwave power is yet to come.

The communication industry is a far more advanced user of microwave technology than the microwave power industry. From standard methods in radar and communication engineering, the microwave power designer can obtain the underlying electromagnetic theory and the technology to transport power from place to place^{(2),(14),(56)}. However, he will find problems which are not encountered in communication systems. For example, most antenna techniques concentrate on the far fields, while the entire task of heating a load is usually done by the near fields, which in the absence of a load are mainly inductive and store energy, rather than radiating it.* Microwave power also involves other disciplines such as thermodynamics which are not treated in communications texts. Publications now exist which deal with unique aspects of microwave power^{(37),(51),(54)}.

Magnetrons are susceptible to damage from reflected power. Inside a magnetron there is a slow wave structure, around which the forward travelling wave propagates in the same direction as a

* The electromagnetic field of a dipole can be broken into components proportional to $1/r^n$, where r is the distance from the centre of the device. Far fields may be defined as those for which $n = 1$. These fields carry energy away, while the near fields, for which $n > 1$, contain stored energy. Alternative usage defines the far field region as distant enough that variations in r affect the relative phase, but not the amplitude, of fields originating from different parts of the antenna. In this usage the near fields would contain some radiating energy.

revolving electron cloud, which acts as an intermediate energy carrier. With the normal type of coupling between the slow wave structure and the external transmission line, the reflected power is divided equally into waves which travel both forward and backward around the internal structure. The backward travelling wave accelerates some of the electrons rather than absorbing their kinetic energy as the forward wave does. Back-bombardment of the cathode results, overheating it and causing sputtering of its active surface, thus shortening tube life. Most devices also fail to oscillate at some loading conditions⁽³⁷⁾.

To limit the effects of reflected power on magnetrons, either the magnetron must be made rugged or the rest of the system must be designed carefully. Magnetron manufacturers have not always been able to assume that the VSWR (voltage standing wave ratio) will be low. The higher the power level of a magnetron, the more difficult it is to design for high VSWR. In present microwave ovens the unpredictable VSWR necessitates a sacrifice in magnetron efficiency to extend its life⁽⁶⁴⁾. One low power (750 Watt) magnetron has been designed this way to tolerate 80% reflected power⁽¹¹⁾. At 18 kW a directionally coupled output has been used.* Automatic matching devices are available, but do not have the response speed to handle sudden faults if the magnetron power level is sufficient to cause it to arc internally⁽⁶⁶⁾. These attempts have not yet solved the problem satisfactorily.

Applicator design can degrade product quality as well as the magnetron life. In most processes in which microwave

* See JMP 4(2) p85 (June 1969).

energy is used, the final product should be evenly heated. Standing waves are inherent in almost all reflections*, and hot spots occur in a load at places where the electric field components are in phase and add, while cooler spots occur where they cancel. Another problem, skin effect, occurs in loads which absorb energy too rapidly, as the heating is concentrated near the surface of such a load. Both effects are treated in more detail in electromagnetic theory texts⁽⁶⁵⁾ and microwave power texts⁽⁵⁴⁾, and must be controlled in most applications. One of the advantages of microwave heating is that energy is absorbed by dielectric losses, becoming thermal energy inside the load. This is commonly called bulk heating and with care, it can be used to produce a rapidly and uniformly heated product.

In travelling wave applicators, heating is performed by a wave propagating in a waveguide structure. The load is a thin dielectric sheet, or web, which is inserted into the waveguide. Part of the energy propagates inside the web, giving bulk heating. However, as the energy travels, some of it is lost as heat in the load and the wave diminishes in amplitude, giving uneven heating as in skin effect. Only part of the energy is carried in the dielectric and the attenuation depends on the ratio between it and that carried in the rest of the applicator. Conventional design of these applicators does not allow for much control of attenuation**;

some loads may be heated nonuniformly while other lighter loads may give low efficiency. Reflected power is not usually severe.

* An exception could occur if cross-polarization should result.

** Fringing field applicators, which heat the load outside the waveguide, provide good attenuation control but may be dangerously leaky. See Chapter 2.

In Chapters 2, 3 and 4, a technique is found for obtaining attenuation control.

In resonant applicators the energy is injected into a cavity and stored until the load (or the walls) absorb it. Standing wave effects in such an applicator are unavoidable, but there are ways to prevent them from producing unacceptable product quality, scorched spots, for example. Multimode cavities are commonly used; large cavities with many modes which are resonant near the same frequency and which have differing field patterns. If energy can be coupled into the fields of several modes, rather than only one, the result is a more uniform electric field distribution^{(44),(38)}. An additional device for obtaining uniformity is the mode stirrer, which rotates or oscillates at a rate that is slow compared to the frequency of the power, but is fast compared to the heating rate. It can change the modal patterns throughout the cavity and as it moves, the electric field inhomogeneities are moved pseudorandomly over the load.

Conventional resonant structures have been designed to improve heating uniformity, to prevent leakage of energy⁽⁴⁶⁾, and to provide many resonant frequencies in the band in which the magnetrons must operate. It is not a simple problem to avoid reflected power when dealing with an applicator which is literally full of multiple reflections and which carries many different modal patterns. Some work has been reported^{(7),(23),(32),(38),(52),(75)} but the basic theoretical treatment of this coupling problem has not been published. In Chapters 5 and 6 of this thesis, cavity coupling theory and a working coupling structure are described. Both reflection coefficient and heating uniformity are improved in an operating system.

1.2 Applicator Parameters

In this thesis the dielectric constant is given by $\epsilon = \epsilon_0(\epsilon_r' - j\epsilon_r'')$, where ϵ_r' is the usual relative dielectric constant⁽⁵⁶⁾. Then Maxwell's equations, in phasor form, have no explicit conduction term. Both conduction effects and dipole effects are contained in ϵ_r'' .

Poynting's theorem can be derived by integrating the divergence of the vector $\hat{E} \times \hat{H}$ over a volume⁽¹⁴⁾. This gives

$$\int_V \nabla \cdot \hat{E} \times \hat{H}^* dv = \int_S \hat{E} \times \hat{H}^* \cdot \hat{n} dS = -j\omega \int_V (\hat{B} \cdot \hat{H} - \hat{E} \cdot \hat{D}) dv \quad (1.1)$$

where \hat{E} is the RMS electric field vector, $\hat{D} = \epsilon \hat{E}$ is the electric flux vector and the asterisk indicates the complex conjugate of a quantity⁵. Similarly \hat{H} and $\hat{B} = \mu \hat{H}$ are the magnetic field vector and flux vector respectively, where μ is the permeability. V is the volume, S is its surface, \hat{n} is a unit vector normal to S , and ω is the radian frequency. Taking real and imaginary parts,

$$\text{Re} \int_S \hat{E} \times \hat{H} \cdot (-\hat{n}) dS = \epsilon_0 \omega \int_V \epsilon_r'' \hat{E} \cdot \hat{E}^* dV \quad (1.2a)$$

$$\text{Im} \int_S \hat{E} \times \hat{H} \cdot (-\hat{n}) dS = j2\omega \int_V \left(\frac{\mu \hat{H} \cdot \hat{H}^*}{2} - \frac{\hat{E} \cdot \hat{E}^* \epsilon_0 \epsilon_r'}{2} \right) dV \quad (1.2b)$$

The left-hand side of Eq. 1.2a is the power flowing into the volume and the right-hand side is the dielectric loss, or heating effect, in Watts. The right-hand of Eq. 1.2b is the difference between the two types of energy stored in the volume, multiplied by 2ω . From Eq. 1.2b

Many texts also use \hat{E} and \hat{H} as the magnitude of $\hat{E} \exp(j\omega t)$ etc. Here they are the (time) RMS values, the magnitudes multiplied by $1/\sqrt{2}$, with the factor $\exp(j\omega t)$ understood.

it can be shown that the energy stored in a lossless cavity is equally divided between the electric and magnetic fields. μ is assumed to be real and equal to its free space value, which is true for the lossy dielectrics usually used as loads.

The bulk heating effect occurs inside any lossy dielectric object, that is, one for which $\epsilon_r'' \neq 0$. The power absorbed is given by Eq. 1.2a for the whole volume or any part of it. If the applicator is a resonant structure and is lossless the integration may be performed over the whole structure. The Q of the structure is defined as the ratio between the energy stored in it and the energy dissipated per radian. If the energy is equally divided between field components and ϵ_r'' is constant,

$$Q = \frac{\int_V \epsilon_r'' \hat{E} \cdot \hat{E}^* dV}{\int_V \epsilon_r' \hat{E} \cdot \hat{E}^* dV} = \frac{\epsilon_r'' \int_{\Delta V} \hat{E} \cdot \hat{E}^* dV}{\int_{V-\Delta V} \hat{E} \cdot \hat{E}^* dV + \int_{\Delta V} \epsilon_r' \hat{E} \cdot \hat{E}^* dV} \quad (1.3a)$$

and if $\Delta V \epsilon_r' \ll (V - \Delta V)$,

$$Q \approx \frac{\epsilon_r'' \int_{\Delta V} \hat{E} \cdot \hat{E}^* dV}{\int_V \hat{E} \cdot \hat{E}^* dV} \quad (1.3b)$$

where ΔV is the volume of the dielectric and V is that of the entire applicator. $V - \Delta V$ represents the empty volume.

The three factors which determine the absorbed power are ϵ_r'' , the volume of the load and the electric field strength inside the load. If ϵ_r'' is constant, the latter two factors can be conveniently expressed in terms of the filling factor F and the field concentration factor ξ . F is normally defined by

$$F = \frac{\Delta V}{V} \quad (1.4)$$

and the field concentration factor will be defined here by

$$\xi^2 = \frac{V}{\Delta V} \frac{\int_{\Delta V} \hat{E} \cdot \hat{E}^* dv}{\int_V \hat{E} \cdot \hat{E}^* dv} \quad (1.5)$$

This definition makes ξ equal to the ratio between the RMS (spatially averaged) electric field in the load and that averaged over the entire structure.

This pair of definitions simplifies Q:

$$Q = \epsilon_r'' F \xi^2 \quad (1.6)$$

if the applicator is lossless*. In Chapter 5 Eq. 1.6 will be extended to include the losses which occur in all practical applicators.

Travelling wave applicators are waveguide structures loaded by dielectric sheets. In this case Q is not a very meaningful quantity. What is more important is the ratio between the power absorbed in a section of waveguide and that transported through it. From Eq. 1.2a the power transported through S by a forward travelling wave is

$$P = \frac{1}{n} \int_S \hat{E} \cdot \hat{E}^* dS \quad (1.7)$$

where $n = E/H$ and is the characteristic impedance of the applicator.

The power absorbed in an infinitesimal length dz of a load with cross-sectional area ΔS is

$$\left(\frac{\partial P}{\partial z}\right) dz = -\omega \epsilon_0 \epsilon_r'' \left(\int_{\Delta S} \hat{E} \cdot \hat{E}^* dS\right) dz \quad (1.8)$$

where $\Delta V = \Delta S dz$ and E is nearly constant in dz . Dividing Eq. 1.8 by Eq. 1.7 and using Equations 1.4 and 1.5 we obtain

* ϵ_r'' contains the frequency dependence.

$$\frac{1}{P} \frac{\partial P}{\partial z} = -\omega \epsilon_0 \epsilon_r'' \eta F \xi^2 \quad (1.9a)$$

or

$$P = P_0 \exp(-\omega \epsilon_0 \epsilon_r'' \eta F \xi^2 z) \quad (1.9b)$$

where P_0 is the incident power at $z = 0$. The attenuation coefficient α (nepers per meter) in

$$P = P_0 \exp(-2\alpha z) \quad (1.9c)$$

is given by

$$\alpha = (1/2) \omega \epsilon_0 \epsilon_r'' \eta F \xi^2. \quad (1.10)$$

Thus heating uniformity and efficiency can be changed by varying the size and ϵ_r'' of the load or by varying ξ^2 .

In all previous cases ξ has been evaluated from electric fields existing in the loaded applicator. This presents a difficult computation problem if the loading conditions are variable. The field patterns of the unloaded applicator are usually easier to obtain and perturbation equations may be derived by taking vector products of these fields and the fields which would exist after the load is in place⁽²⁾. If F is small the effect is localized. Only the fields near the load will change, and they may be found, by using the local boundary conditions. Appendix I gives further information.

The load in travelling wave applicators is usually a thin sheet or web. If F is small and the web edges are parallel to the electric fields of the unloaded applicator, the fields will be almost unchanged by the load, while the flux \hat{D} is multiplied by ϵ_r' . The mode is called an LSE mode (longitudinal section electric) in this case while if the magnetic fields are parallel to the load the mode is called LSM (longitudinal section magnetic). LSE modes give higher attenuation than LSM modes, where ξ is reduced to ξ/ϵ_r' by the load.

In Figure 1.1 two common waveguides are shown. Thin webs inserted as shown will result in LSE modes with the same field patterns as the dominant modes. Let B be the total length (meters) exposed to the microwave energy in a cross-section and let t' be the web thickness. Then for nearly flat webs $S \approx Bt'/2$. The field concentration is nearly constant over the thickness and as long as the perturbation is small (See Appendix I) ϵ is independent of t' . Then for any length

$$\epsilon^2 = \lim_{t' \rightarrow 0} \frac{S}{\Delta S} \frac{\int_{\Delta S} E \cdot E^* dS}{\int_S E \cdot E^* dS} \quad (1.11)$$

This is the form used in the perturbation analyses in the next three chapters.

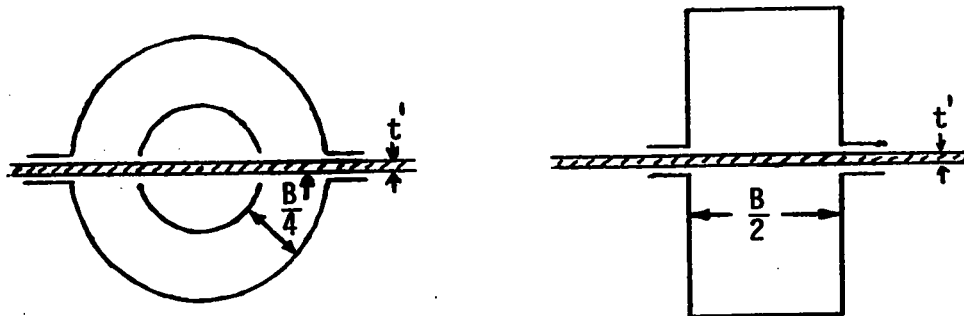


Figure 1.1 Cross-Section of Web in Applicators

CHAPTER TWO

ATTENUATION CONTROL IN TRAVELLING WAVE APPLICATORS

This and the next two chapters form a section dealing with web applicators. In this chapter conventional applicators are examined for attenuation control. Some new travelling wave applicators are then described and the rectangular TEM structure is singled out as the most promising, a detailed analysis of which will be given in Chapter Three.

2.1. Conventional Techniques

The use of rectangular TE_{10} waveguide is still very common for microwave heating of webs. The web passes through slots in the center of the broad side of the waveguide, as shown in Figure 2.1. Each time the guide passes across the web, part of the energy is deposited in the dielectric. To use the remaining energy, the wave must make several passes, as shown in Figure 2.2. This is a crosscurrent applicator, i.e. the web moves forward slowly while the microwave energy crosses it⁽³⁵⁾. (See Chapter 4.)

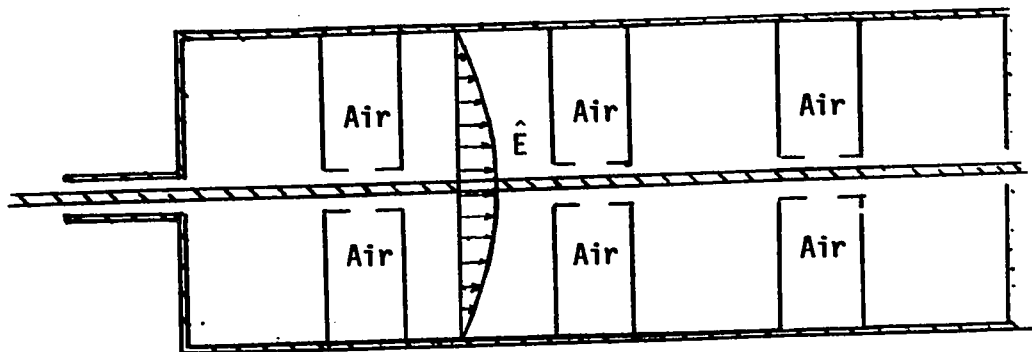


Figure 2.1.

Cross-section of TE_{10} Applicator

Usually such heating is used for moisture removal. Bulk heating of a dielectric delivers the latent heat of evaporation to the water without conventional heat transfer through an insulating surface layer. The air supply shown in the figures is used for moisture transport; it need not be heated if it is dry and moving rapidly. Furthermore, the walls are cold and will condense the water from overly moist air. Small turbulent jets impinge upon the web at right angles and large holes are provided for easy air escape. Any liquid on the walls must be blown out or fall out of the bottom exits. The guide must not drip, since this could cause arcs. Further detail is provided by Okress⁽⁵¹⁾.

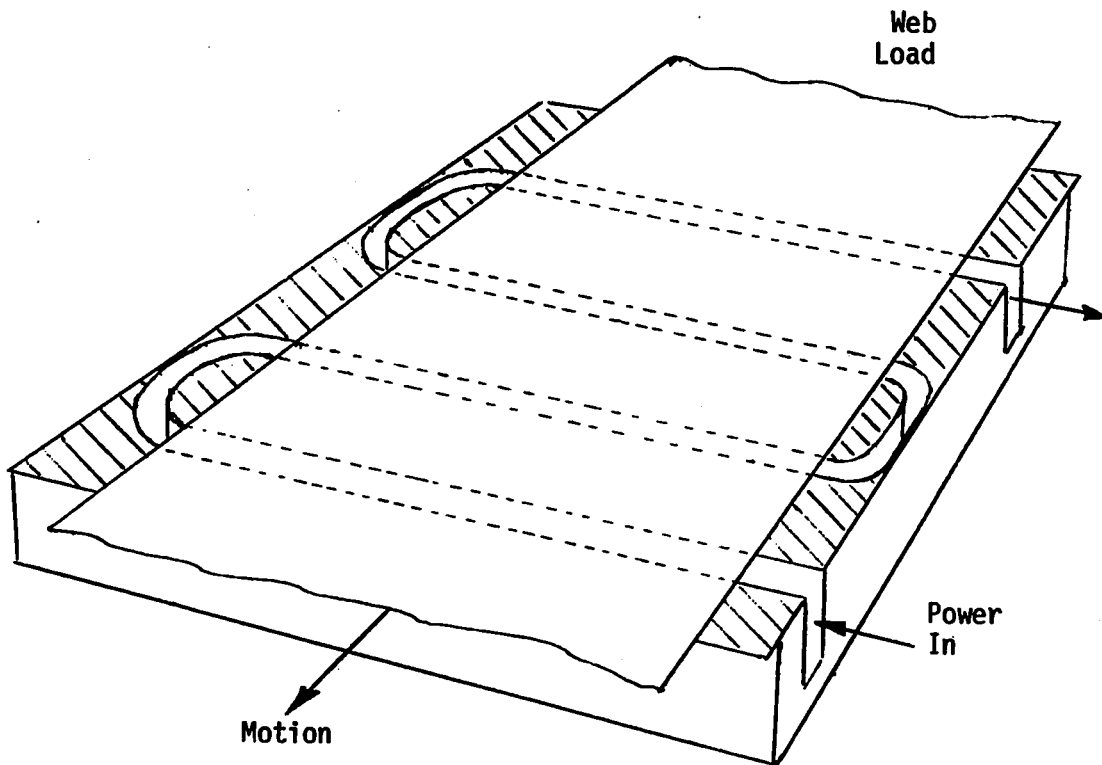


Figure 2.2

Bottom Half of TE₁₀ Applicator

As the wave crosses the web, it loses energy. Altman⁽²⁾ uses perturbation theory (See Appendix I) to obtain:

$$\alpha = \frac{\omega \epsilon_0 \epsilon_r'' \int_{\Delta S} (\hat{E}_0 \cdot \hat{E}) dS}{2 \int_S (\hat{E}_0^* \cdot \hat{H}) \cdot \hat{n} dS} \quad (2.1)$$

where α is the attenuation coefficient in nepers per meter, \hat{E}_0 is the unperturbed electric field vector, \hat{E} is the perturbed field, and \hat{n} is a unit vector perpendicular to the cross-section. If the web does not change the fields Eq. 2.1 gives the same expression as before, $\alpha = \left(\frac{1}{2}\right) \epsilon_0 \epsilon_r'' F \xi^2 \eta$. This is a general description; it shows that reducing either F or ξ^2 will improve uniformity at the expense of efficiency.

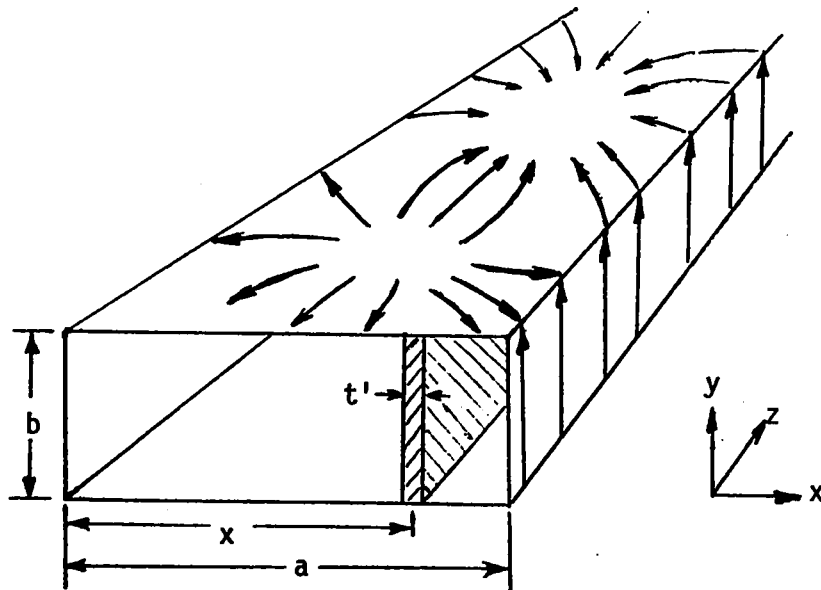


Figure 2.3 Currents and Dimensions for TE₁₀ Applicator

Applying Eq. 2.1 to the standard TE₁₀ applicator,

$$\alpha_g = \omega \epsilon_0 \epsilon_r'' F_{g n_0} \left(\frac{\lambda_g}{\lambda_0}\right) \sin^2 \left(\frac{\pi x}{a}\right) \quad (2.2)$$

where the subscript g refers to the waveguide and where the filling

factor F_g is given by t/a of Figure 2.3. The guide wavelength λ_g is greater than the free space wavelength λ_0 ; an effect which gives increased α_g near cutoff.

In a line along the centre of the broad wall of the guide the wall currents flow only in the \hat{z} direction. At other x locations in the broad wall they will cross the slot, producing displacement current, and from it, radiation or leakage. This fixes x/a to $1/2$ and ξ^2 to 2. There is no acceptable way of controlling ξ^2 unless other structures are introduced into the applicator to change the basic mode⁽⁴¹⁾.

The width a can be changed to control F but cutoff results if it is less than $\lambda_0/2$. It should not exceed $3\lambda_0/2$ because other modes can be generated in wide guides. Changing b deposits more power in less web, leaving α_g unchanged. Thus simple TE_{10} applicators do not permit good attenuation control⁽⁴⁰⁾.

Another type of applicator is the fringing field applicator, where a field component exterior to the structure intercepts the load^{(19), (42)}. Very little power is carried in such fields and they die away rapidly with distance from the applicator. By using multiple resonator sections, very high fringing field strengths may be obtained and since the bulk of the power is not applied to the load, the attenuation may be gradual. Fringing field applicators are distributed structures, so they will accept a wide variety of loading conditions with little reflected power.* When operated unloaded,

* This effect is discussed in greater detail in Chapter 5 where slow wave structures are adapted to cavity coupling. The structures used in that chapter are fringing field applicators applying power to an intermediate structure, a multimode resonant cavity. Phase control is also important to that problem, while it is nearly irrelevant here.

power is radiated away and the reflection coefficient can be controlled.

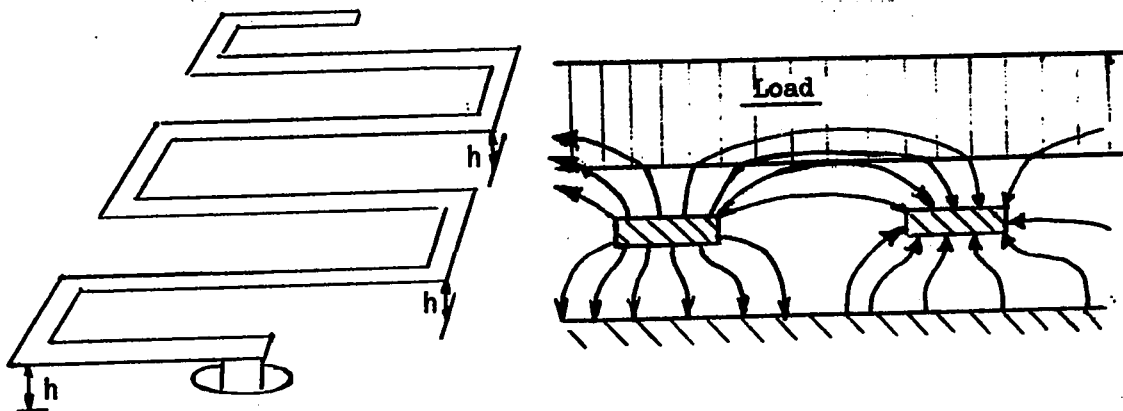


Figure 2.4 TEM Fringing-Field Applicator

Some sample structures are shown in Figures 2.4 and 2.5. In the first case, a stripline has been formed into meandering transmission line and the load above it absorbs power from the fields emanating from the top of the conductor. Before terminating on the ground plane, these flux lines are intercepted by the load, and the further the load is from the conductor, the fewer flux lines reach it. Most of the power is carried below the stripline. In the second example, one side has been removed from a meandering TE_{10} waveguide and the fields inside spill out. Air may be blown from below for flotation and moisture transport.

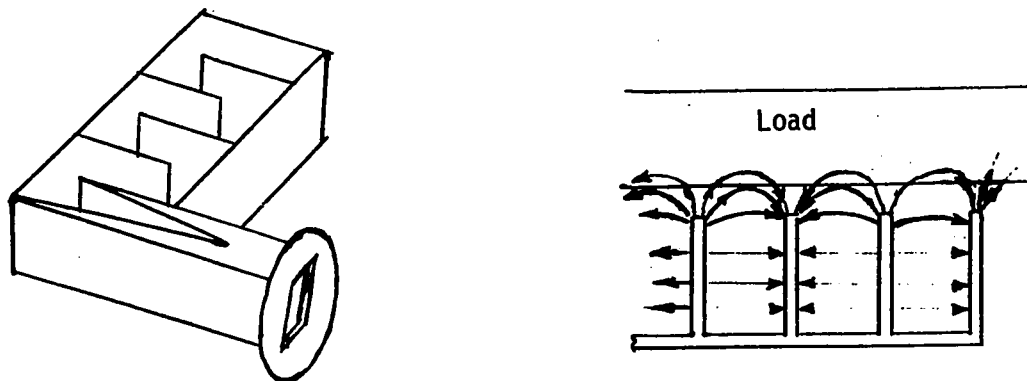


Figure 2.5 TE_{10} Fringing-Field Applicator

The fact that fringing fields die away rapidly implies that only the surface of a thick material will be heated. Therefore fringing field applicators have been considered for drying the paint strips on pavement⁽²⁴⁾, although this has not proved feasible. Radiation of unused power has the advantage that it can protect the magnetron from reflections, but the result can be accidents. There are also hot spots in almost all of the fringing field structures, but this problem may be overcome by adjusting the dimensions of the applicator*.

Because of their insensitivity to loading conditions these structures are replacing the TE_{10} applicator in practice. However, many of their advantages can be more safely attained in a closed applicator, as will be shown in the rest of the chapter.

2.2 Circular Coaxial Applicator

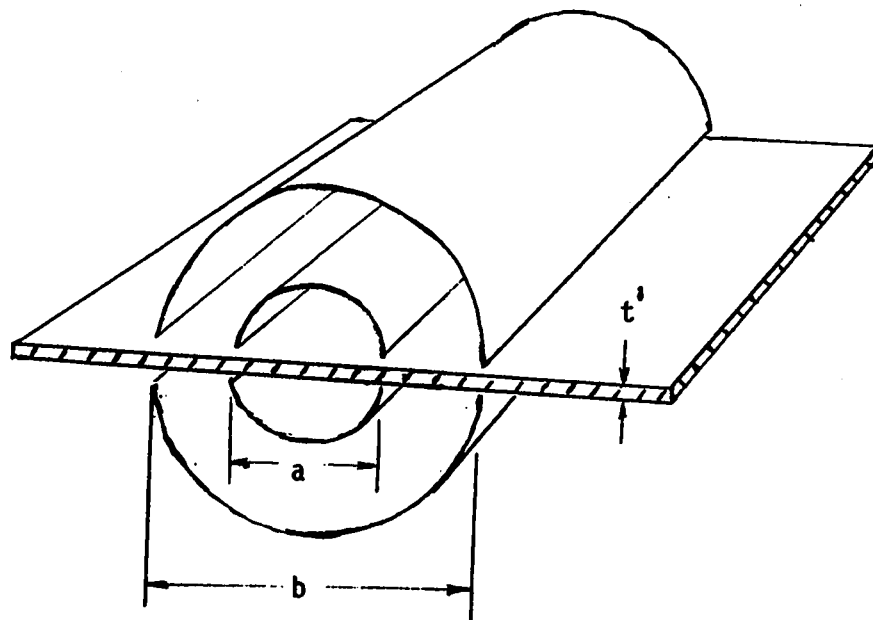


Figure 2.6 Circular Coaxial Applicator

* Pat. pending in 1971, Genesy's Systems.

A simple TEM alternative to TE_{10} waveguide is the circular coaxial structure of Figure 2.6*. Its electric fields obey the well known relationship:

$$\hat{E}_r = \frac{\phi}{r \log_e \left(\frac{a}{b}\right)} \hat{r} \quad (2.3)$$

where E_r is the radial electric field, a , b and t are as in Figure 2.6, \hat{r} is a radial unit vector and r is the distance from the centre⁽⁵⁶⁾. If t is small,

$$E_t \approx E_r \quad (2.4)$$

Substituting in 2.1, we obtain

$$\begin{aligned} \alpha &= \frac{\epsilon_0 \epsilon_r''}{4\pi} \frac{2\omega \int_a^b t' \left(\frac{\phi}{r \log_e (a/b)}\right)^2 dr}{2 \int_a^b \frac{1}{\eta_0} \left(\frac{\phi}{r \log_e (a/b)}\right) \cdot 2\pi r dr} \\ &= \frac{\epsilon_0 \epsilon_r'' \eta_0 t \omega}{3\pi} \frac{(1 + b^2/ab + a^2/ab)}{(a + b)} \end{aligned} \quad (2.5)$$

or

$$\alpha_c = \left(\frac{1}{6}\right) \epsilon_0 \epsilon_r'' \eta_0 \omega F_c (1 + b/a + a/b) \quad (2.6a)$$

where the subscript c refers to coaxial lines, and

$$F_c \approx \frac{2t'}{\pi(a + b)} \quad (2.6b)$$

The filling factor F_c is defined as in the previous chapter. If we separate out the field concentration factor, we obtain

$$\xi^2 = (1/3)(1 + b/a + a/b) \quad (2.7)$$

* Another alternative is the twinline, in Appendix II.

This becomes unity as the characteristic impedance becomes very small.

In all TEM structures the currents are parallel to the direction of propagation. Therefore, a longitudinal slot may be located anywhere with no problem of radiation from displacement current crossing it.

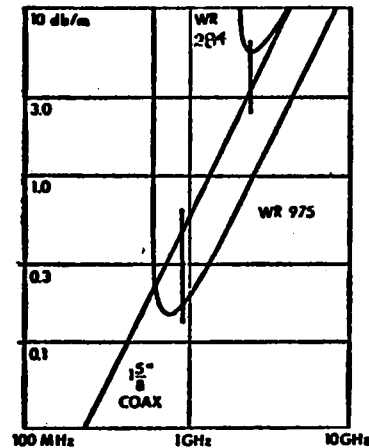


Figure 2.7 Attenuation of Simple Structures (From 40)

Comparing the TE_{10} rectangular waveguides to 50 ohm coaxial line, we obtain

$$\frac{\alpha_c}{\alpha_g} = 0.623 \left(\frac{F_c}{F_g}\right) \left(\frac{\lambda_0}{\lambda_g}\right) \quad (2.8)$$

In Figure 2.7, computed results for attenuation in a 0.24 kg/m^2 web at about 25% water content are shown. It has no cutoff frequency, so the TEM structure can give higher attenuation because F_c can be made large by making the structure small. Cutoff effects prevent this in the rectangular waveguide, since t and a determine F_g . Circular coaxial line provides some attenuation control, and the centre conductor forms an obvious air conduit. However, it is not simple to build. ϵ^2 is a constant if the characteristic impedance

is kept constant, and it is close to unity.

A section of 50 ohm, 1 5/8" circular coaxial line with a 1/8" slot was constructed. Its walls were 0.08" thick. Using strips of very wet paper, the attenuation factor in Figure 2.7 was confirmed. For comparison a TE_{10} WR284 waveguide section with the same wall thickness and slot width was prepared. This too gave the predicted attenuation.

If a wet web is used, energy propagates out of the applicator in a dielectric wave⁽⁶⁹⁾. To check the leakage of the two applicators, they were loaded very heavily with wet paper. A laboratory generator applied 100 mW of forward power to each applicator. With a Narda 8110 leakage detector it was found that leakage was proportional to the ratio of α_c and $\alpha_g^{(5)}$. This means that leakage depends on the electric field intensity in the web region, and not on the mode. When metal dipoles were used, which is an unusual practice, the coaxial line gave significantly more leakage, since the dipoles were capacitively coupled to the centre conductor. This effect was not observed for even the wettest paper. Thus for reflectionless dielectric loading, the escaping power is proportional to $(\epsilon^2 P_f)/S$ where P_f is the forward travelling power.

A TEM applicator has been found which does what a TE_{10} one will. It also permits control of F_c , but ϵ is nearly constant.

2.3 Variable Cross-Section TEM Applicators

In addition to control of F , by scaling the dimensions, we may control ϵ^2 by placing the web in a region where electric fields are reduced⁽⁴⁰⁾. To do this, non-circular cross-sections must be used. Because the currents are not transverse, virtually

any structure comprised of two or more insulated pieces of metal may be slotted longitudinally and used as an applicator, provided that it bears no higher order modes. Many possible systems provide the reduced ξ^2 , giving reduced attenuation, leakage, and even reflections, since low ξ implies that most of the energy does not impinge upon the edge of the web.

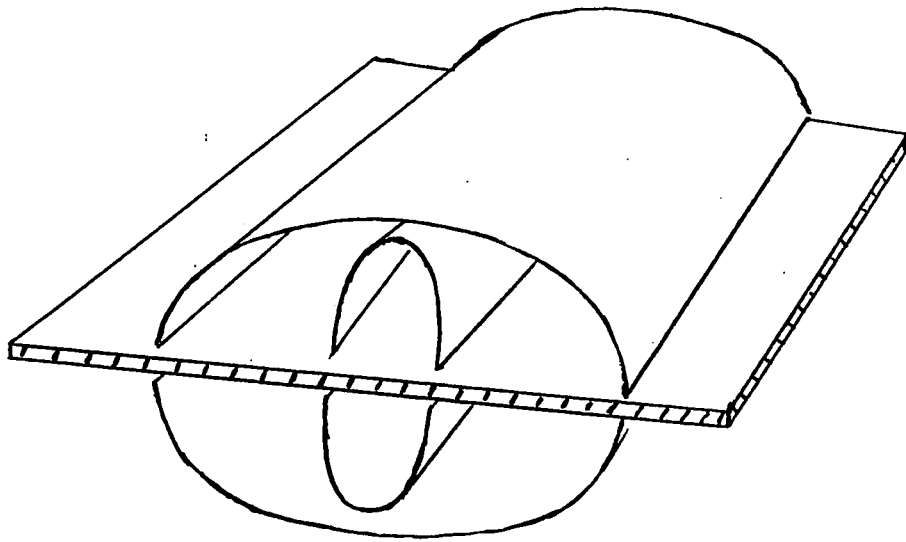


Figure 2.8 Elliptical TEM Applicator

The simple circular structure can be distorted and made elliptical as in Figure 2.8. The region of high power transport is the narrow gap between the major and minor axes of the inner and outer conductors respectively. The web passes through the low field region between the other axes of the conductors. However, F_c is increased in the process and α is not reduced as rapidly as ξ^2 .

A much easier structure to construct is shown in Figure 2.9. A rectangular centre conductor * is used with an elongated rectangular

* In the rest of this thesis it is assumed to be square, but if its shape is adjusted, added control of ξ^2 is possible.

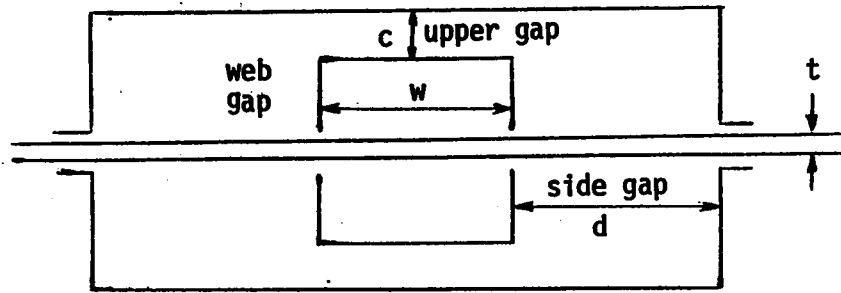


Figure 2.9 Rectangular TEM Applicator

outer conductor. The effect on ϵ^2 is the same as in the elliptical applicator. The corners must, of course, be rounded to prevent arcing.

A first order analysis may be made by treating the upper and side gaps as parallel plate capacitors and ignoring curvature of the fields. This is valid for any frequency, since there is no cutoff frequency and therefore no dispersion in TEM structures. If we assume that $w \gg c$, we can assume that the voltage gives the electric fields directly, or $\phi = (E_d)d = (E_c)c$. For small perturbations and square centre conductors, we may expand 2.1 as follows:

$$\alpha = \frac{\eta_0 \omega \epsilon_0 \epsilon_r'' \int_0^d \left(\frac{V}{d}\right)^2 t dy}{2 \int_0^c \left(\frac{V}{c}\right)^2 w dx + 2 \int_0^d \left(\frac{V}{d}\right)^2 w dy + \int \int_{\text{corners}} |E|^2 dS} \quad (2.9)$$

If $d \gg c$ the first of the lower three integrals dominates and the power is carried mainly above and below the centre conductor. The attenuation is then proportional to c/d .

This result is for the asymptotic case: low characteristic impedance and very small c/d . When the gaps c and d become large the electric field is no longer constant and the upper integral becomes

a constant because the fields diverge at the side of the centre conductor. It is expected that the resulting minimum α may be reduced by making the centre conductor higher than it is wide, or by making the face of the centre conductor concave.

The leakage of such a structure is dependent on ξ^2 while attenuation depends on both ξ^2 and F . Leakage is then proportional to $(c/d)^2$, and this applicator can give reduced leakage while providing the same attenuation as a given circular coaxial or rectangular TE_{10} applicator.

If the characteristic impedance of an applicator undergoes sharp changes, as when a heavy load passes through a high field region or ξ^2 is changed, these discontinuities will reflect power toward the magnetron. If there is an absorbing web between the reflection and the power source, the problem is reduced, but this cannot be guaranteed. The characteristic impedance change is proportional to ξ , so reduction of ξ also controls the problem of reflections from the web edges.

Similar results have been demonstrated in waveguides^{(8),(41)} by reducing the fields in the centre of the TE_{10} rectangular structure by providing two constricted regions on either side of centre. The power was conveyed in these regions, reducing ξ^2 by the same principle as in the TEM structures of Figure 2.8 and Figure 2.9. The biggest difficulty in either mode will be arcing, but with rectangular TEM structures arcing will be easier to control since wider regions are provided for power transport*.

* A simple TE_{10} waveguide can carry more power than either structure. See the example at the end of Chapter 3.

CHAPTER THREE

NUMERICAL ANALYSIS OF THE RECTANGULAR TEM APPLICATOR

In the previous chapter it was shown that control of the parameter ξ^2 is possible in TEM structures. Approximate behavior of attenuation for the rectangular version was derived from simplifying assumptions. In this chapter ξ^2 will be evaluated more accurately and the previous expression will be verified. The perturbation technique will be retained, allowing the fields to be calculated for the empty applicator. The loaded applicator is assumed to have the same fields, which is approximately true for the electric field if the web is thin and is parallel to the electric fields calculated for the empty applicator.

The assumption of parallel plate capacitor behavior will be replaced by the method of moments. In this method it is assumed that the charges existing on the conductors can be accurately represented by a screen of infinitely long line charges. When these charges are obtained, it will be possible to present the designer with charts, from which he can select rectangular TEM shapes to give desired ξ^2 , F and characteristic impedance Z_0 (47), (48).

3.1 Characteristics of the Rectangular Structure

ξ^2 can either be derived from the area integration in Chapter 1, or from a volume integration over some length of applicator. Let ΔS be the cross-sectional area of the empty structure which will later be occupied by the web. Expressed in terms of volumes, if the fields in ΔS are constant over the thickness of the web,

$$\xi^2 = \lim_{t \rightarrow 0} \frac{V}{\Delta V} \frac{\int_{\Delta V} \hat{E} \cdot \hat{E}^* dv}{\int_V \hat{E} \cdot \hat{E}^* dv} \quad (3.1)$$

where ΔV is the volume $z'\Delta S$. ΔS can only be changed in magnitude by changes in thickness t' . V is the volume $z'S$ and z' is the active length of applicator, measured along the propagation path of the wave. Similarly ξ^2 can be treated as a power transport parameter. The power carried in the total cross-section S at unity VSWR is given by

$$P_f = \int_S (\hat{E} \times \hat{H}) \cdot d\mathbf{S} = \left(\frac{1}{n}\right) \int_S (\hat{E} \cdot \hat{E}^*) dS \quad (3.2)$$

from Poynting's theorem. The power carried in the web region ΔS of the empty structure is given by

$$P_{fw} = \frac{1}{n} \int_{\Delta S} (\hat{E} \cdot \hat{E}^*) dS. \quad (3.3)$$

Then

$$\xi^2 = \lim_{t \rightarrow 0} (S/\Delta S) (P_{fw}/P_f) \quad (3.4)$$

For LSE modes, if the web is found to be a minor perturbation by a check such as that given in Appendix I and if the fields are nearly constant in its vicinity, the total mean-squared electric fields in it can be found by multiplying ξ^2 by $P_f F/n$. If ξ^2 is known, the heating rate and attenuation constant can be found from the power level and web properties.

The electric fields shown in Figure 3.1 may be calculated by the method of relaxation (18), (27), (47), (60) or the method of moments (33). It was decided to use an extension of Harrington's moment method for economy of computer time as well as for accuracy. The relaxation method is iterative, involving a very large number of

calculations. In addition, it results in a grid of voltages whose gradient must be evaluated and squared. Numerical differentiation can produce very large errors. The method of moments produces a set of charges, from which all the other parameters may be obtained directly.

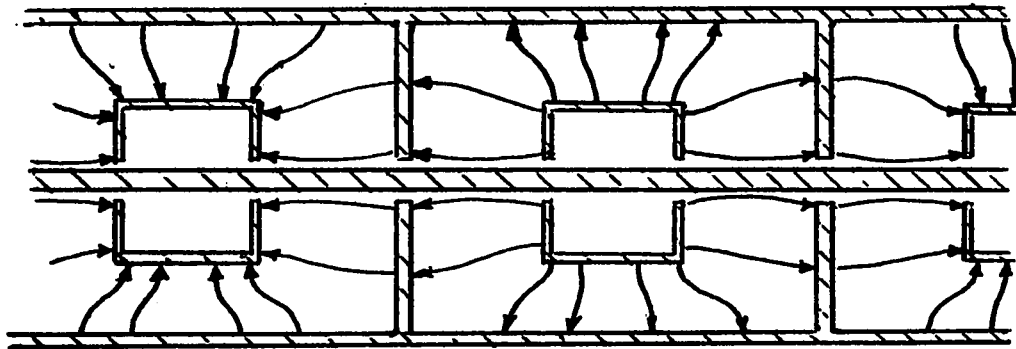


Figure 3.1 **Rectangular TEM Applicator**

For matching the applicator to the power source as well as for minimizing internal standing waves, the characteristic impedance must be known. This is given by $Z_0 = 1/c\underline{C}$ where c is the velocity of the wave which in empty TEM structures travels at the speed of light. \underline{C} is the capacitance per meter, given by

$$\underline{C} = (|q_a| + |q_b|) / 2 \phi, \quad (3.5)$$

q_a and q_b being the charge per meter on the inner and outer conductors respectively. ϕ is the voltage difference between conductors, and the average voltage of the system is set to give equal $|q_a|$ and $|q_b|$.

3.2 A Mathematical Technique for TEM Structures

(a) The Moment Method

The method of moments can be used for electrostatic systems. TEM applicators have the same electrical properties at any frequency

if they are reflectionless. Thus we can start from the fact that the voltages on the conductors are constant on the metal surfaces and find the zero frequency charge distribution which generates them.

To avoid solving integral equations, which involve an infinite number of charges, the moment method approximates the charge distribution by elementary charged areas. These elements have an assumed internal charge distribution or weighting function, which is fixed in form but multiplied by a scalar. The scalars have the dimensions of charge and convert the relationship into a matrix equation for which they form the vector of independent variables. In fact, though, it is the voltages which are known. This means that a matrix inversion is needed to change this simple relationship between charges and voltages into one in which voltage is the independent variable.

The method of moments is an approximation. It is based on the fact that the voltage at a distant location* is sensitive not to the arrangement of charge in an element, but to the magnitude. The approximation can be improved by increasing the number of elements, and by selecting the weighting function to better approximate the actual distribution or to produce errors which cancel.

Let a charge density σ Coulombs per square meter be distributed over the conductors of Figure 3.1. Assume that it generates a voltage $\phi_0 + 1$ volt on the inner conductor. These voltages, at any desired location, (x,y,z) can be obtained from σ

* Further from the nearest charge than the width of the elementary areas.

by electrostatics:

$$\phi(x,y) = \iiint \frac{\sigma(x',y',z')}{4\pi\epsilon r} dx dy dz \quad (3.6)$$

where $r = \sqrt{(x - x')^2 + (y - y')^2 + (z - z')^2}$ and the dummy coordinates (x', y', z') are the location of the infinitesimal charge element of the integration. However, the charge distribution σ must be found. To do this, we use line charge weighting functions (Dirac delta functions), $\delta(x - x')\delta(y - y')$. The charge sheets σ on the conductors are then approximated by a screen of line charges $q_j \delta(x - x')\delta(y - y')$, infinitely long in the z direction. Then in matrix tensor form, Equation 3.6 may be approximated by

$$\phi_i(x'_i, y'_i) = L_{ij} q_j(x'_j, y'_j) \quad (3.7a)$$

and in inverted form,

$$q_j(x'_j, y'_j) = L_{ij}^{-1} \phi_i(x'_i, y'_i) \quad (3.7b)$$

where primes indicate a charge location, and where repeated indices indicate summation. L_{ij} is given by $\partial\phi_i/\partial q_j$.

If $x'_j = x'_i$ and $y'_j = y'_i$, or in other words if we try to evaluate the self-potential of a line charge, a discontinuity results. To avoid this, a strip charge is assumed in evaluating L_{ij} . The weighting functions must be changed in this case, and we may use strips of width $\frac{1}{2} \sqrt{(x'_{j+1} - x'_{j-1})^2 + (y'_{j+1} - y'_{j-1})^2}$ centered at (x'_j, y'_j) .

It is now possible to evaluate the L_{ij} directly from electrostatic theory and invert the matrix by digital computer*.

* There are inversion routines in the IBM standard routines based on Gauss Jordan reduction. One of these was used. However, it has been shown (10) that the moment method can give rise to ill-conditioned matrices, for which inversion gives escalation of round-off errors. This will be discussed later.

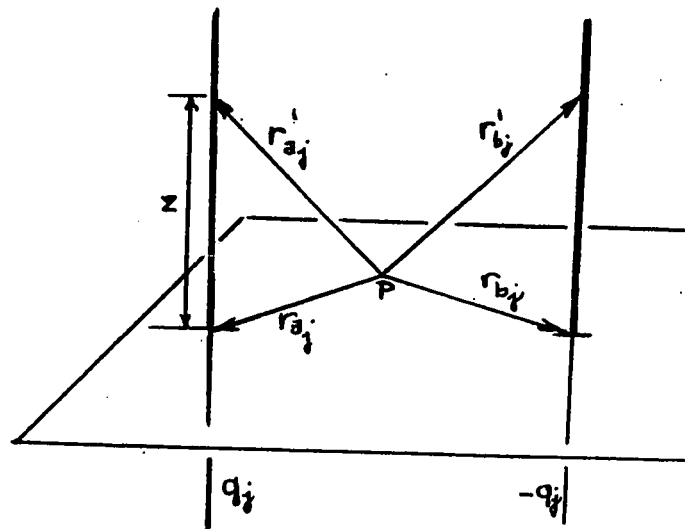


Figure 3.2 Line Charges

Let p be a measurement point, a distance r away from a line charge of q Coulombs per meter. Then the voltage at p is

$$\phi_p = \frac{1}{4\pi\epsilon} \int_{-\infty}^{\infty} \frac{qdz}{r'}$$

where $r' = \sqrt{r^2 + z^2}$. For a single charge the voltage is

$$\phi_p = \lim_{u \rightarrow \infty} \frac{q}{2\pi\epsilon} \left[\ln(z + \sqrt{z^2 + r^2}) \right]_0^u \quad (3.8)$$

The infinity may be removed by evaluating the potential for equal and opposite pairs as in Figure 3.2*. Then,

$$\begin{aligned} \phi_p &= \frac{q_j}{2\pi\epsilon} \left[\ln \frac{z + \sqrt{r_a^2 + z^2}}{z + \sqrt{r_b^2 + z^2}} \right]_0^\infty \\ &= -\frac{q_j}{2\pi\epsilon} \ln \left(\frac{r_a}{r_b} \right). \end{aligned} \quad (3.9)$$

In 3.7, if p represents the location of another charge, $L_{p,j}$ must be expressed in terms of charge j and its image charge, i.e.

*It may also be removed by using a reference point at a finite distance from the applicator.

$$L_{p, ab_j} = \left(\frac{-1}{2\pi\epsilon}\right) \ln \left(\frac{r_{a_j}}{r_{a_j}}\right). \quad (3.10)$$

The errors in using line charges are evaluated in Appendix III.

The electric field near a line charge is given by

$$\hat{E} = -\nabla\phi = \frac{q}{2\pi\epsilon r} \hat{r}. \quad (3.11)$$

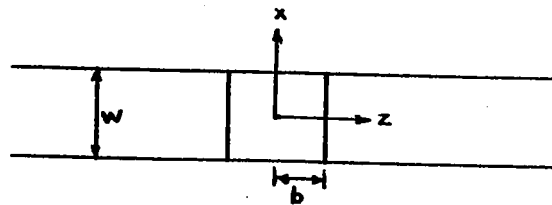


Figure 3.3 Strip Charge

To evaluate the voltage in the centre of a strip where $i = j$, we use the geometry of Figure 3.3. At the centre, Eq. 3.1 gives

$$\begin{aligned} \phi_{ii} &= \int_{-b}^b \int_{-a}^a \frac{\sigma dz dx}{4\pi\epsilon \sqrt{x^2 + z^2}} \\ &= \frac{\sigma}{4\pi\epsilon} \int_{-b}^b \ln \left(\frac{\sqrt{z^2 + a^2} + a}{\sqrt{z^2 + a^2} - a} \right) dz. \end{aligned} \quad (3.12)$$

Making appropriate substitutions and integrating by parts, we obtain

$$\phi_{ii}(w,b) = \frac{\sigma w}{2\pi\epsilon} \left[\text{Sinh}^{-1} \left(\frac{2b}{w} \right) + \left(\frac{2b}{w} \right) \text{Sinh}^{-1} \left(\frac{w}{2b} \right) \right] \quad (3.13)$$

where w is the width of the strip and b is its extent in the $\pm z$ direction. This gives the self-voltage of one of the strips in the applicator. Here too, the voltage increases without limit as b approaches infinity,* and, a strip of equal and opposite charge must

* When $2b = w$ we obtain Harrington's solution for a square area.

always be present on the other conductor.

We may approximate the image charge as we have done for the other cases where $i \neq j$. A line charge of magnitude $q = -\sigma w$ is assumed to be located at its centre. If the matching charge is located a distance r away, its voltage for a length $2b$ is, from 3.8,

$$\phi_{i,n+1-i} = \frac{-\sigma w}{2\pi\epsilon} \left[\ln(b + \sqrt{b^2 + r^2}) - \ln r \right]. \quad (3.14)$$

The self voltage of this system of charges is

$$\phi_{ii} = \frac{\sigma w}{2\pi\epsilon} F_1(r, w) \quad (3.15)$$

where

$$F_1(r, w) = \lim_{b \rightarrow \infty} \left\{ \text{Sinh}^{-1}\left(\frac{2b}{w}\right) + \left(\frac{2b}{w}\right) \text{Sinh}\left(\frac{w}{2b}\right) + \ln\left(\frac{r}{b + \sqrt{b^2 + r^2}}\right) \right\}. \quad (3.16)$$

Taking limits, $\lim_{b \rightarrow \infty} \ln\left(\frac{r}{b + \sqrt{b^2 + r^2}}\right) = \ln\left(\frac{r}{2b}\right)$; $\lim_{x \rightarrow \infty} x \text{Sinh}^{-1}\frac{1}{x} = 1$;

and $\lim_{x \rightarrow \infty} \text{Sinh}^{-1}(x) = \ln x + \ln 2$.

This gives

$$\begin{aligned} F_1(r, w) &= \lim_{b \rightarrow \infty} \left\{ \ln\left(\frac{2b}{w}\right) + \ln\left(\frac{r}{2b}\right) + 1 + \ln 2 \right\} \\ &= \ln\left(\frac{r}{w}\right) + 1 + \ln 2 \end{aligned} \quad (3.17)$$

and

$$\phi = \frac{\sigma w}{2\pi\epsilon} \left(\ln\frac{r}{w} + 1.693147 \right). \quad (3.18)$$

Eq. 3.18 gives the self voltage at the centre of a strip, and must of course be used again with a different w when obtaining the self voltage of the image charge.

(b) Use of Image Charges

For the rectangular TEM applicator, each charge occurs in the presence of an equal and opposite charge on the other conductor. In addition, three more identical charge pairs are located symmetrically as in Figure 3.4. Assume that $(\sigma_m w_m)_{00}$ is at (y_m, x_m) while $(\sigma_m w_m)_{01}$ is at $(y_m, -x_m)$, $(\sigma_m w_m)_{10}$ is at $(-y_m, x_m)$ and $(\sigma_m w_m)_{11}$ is at $(-y_m, -x_m)$. The matching charges are $(\sigma_{n+1-m})_{\ell, k}$ where n is the total number of charges, m is the index of the charge considered, and ℓ, k are 0 for the positive half plane and 1 for the negative half plane. $(\sigma_{n+1-m} w_{n+1-m}) = -\sigma_m w_m$ and is located at $(y_{n+1-m}(-1)^\ell, x_{n+1-m}(-1)^k)$, for a total of four images. Then if $i \neq j$ using Eq. 3.5, $a = m$, $b = n + 1 - m$ and

$$L_{ij} = \frac{1}{2\pi\epsilon} \sum_{k=0}^1 \sum_{p=0}^1 \left[-2n \frac{\sqrt{(y_i - (-1)^k y_j)^2 + (x_i - (-1)^p x_j)^2}}{\sqrt{(y_i - (-1)^k y_j)^2 + (x_i - (-1)^p x_{n+1-j})^2}} \right] \quad (3.19)$$

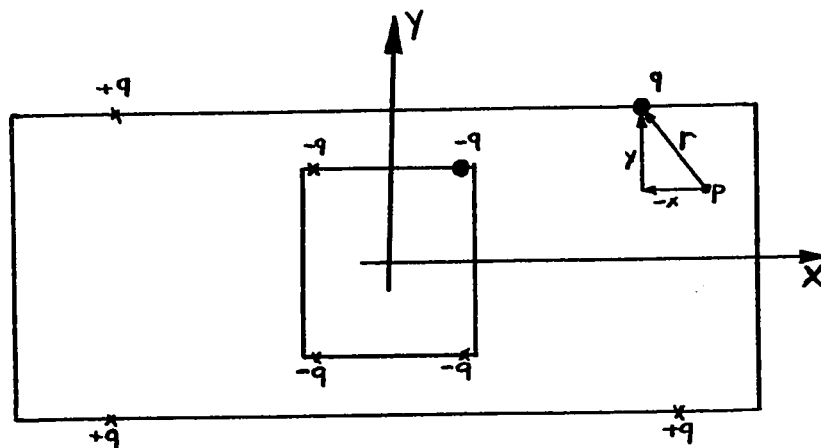


Figure 3.4

Image Charges

When $i = j$, the self voltage of this pair must be added to those of the image pairs. Using Equations 3.5 and 3.8

$$\begin{aligned}
 L_{ij} = \frac{1}{2\pi\epsilon} \{ & 1 + \ln 2 + \ln \left[\frac{\sqrt{(y_i - y_{n+1-i})^2 + (x_i - x_{n+1-i})^2}}{w_i} \right] \\
 & + \ln \left[\frac{2x_i}{\sqrt{(y_i - y_{n+1-i})^2 + (x_i + x_{n+1-i})^2}} \right] \\
 & + \ln \left[\frac{2y_i}{\sqrt{(y_i + y_{n+1-i})^2 + (x_i - x_{n+1-i})^2}} \right] \\
 & + \ln \left[\frac{2\sqrt{x_i^2 + y_i^2}}{\sqrt{(y_i + y_{n+1-i})^2 + (x_i + x_{n+1-i})^2}} \right] \} \quad (3.20)
 \end{aligned}$$

It is now possible to invert the matrix L_{ij} , providing that the proper distribution of the opposite images is known. This must be determined iteratively. As a first approximation, we can assign images in a location close to the correct one by simply distributing them equidistant from each other. For a magnitude of $\sigma_i w_i$ in 3.7a we may use that of either the charge i or its image $n+1-i$, whichever is closer. The accuracy of this is improved by the fact that the log function is quite insensitive to errors in faraway charges. We then let

$$L_{ij} = \frac{1}{2\pi\epsilon} \left\{ \ln \left(\frac{r_{i,n+1-j}}{r_{ij}} \right) + \dots \right\} \text{ if } r_{ij} \leq r_{i,n+1-j}, \quad L_{ij} = 0$$

if $r_{ij} > r_{i,n+1-j}$ or alternatively we may average the two charges,

letting $L_{ij} = \frac{1}{2} \left(\frac{1}{2\pi\epsilon} \right) \left\{ \ln \left(\frac{r_{i,n+1-j}}{r_{i,j}} \right) + \dots \right\}$ for each. Both methods give accurate capacitance results, but to reposition the charges later it is desirable simply to use the nearest charge.

(c) Calculation of the Average Voltage.

If the charges are not paired properly, the capacitance and electric fields will be slightly incorrect. This error will arise in practice because the average voltage is not usually zero when the charges are paired, but shielding results in some average voltage other than zero for the structure. An infinitesimal unbalance in these infinitely long charges is sufficient to give a finite average voltage to the structure, as is shown by Eq. 3.8. This possibility has been eliminated in the final expressions for L_{ij} , Eq. 3.19 and Eq. 3.20. Thus the error has no useful physical significance, since it results from violating the charge pairing assumption.

Let us assume a 1 volt potential difference between conductors and evaluate the resulting average voltage. To obtain the capacitance, let

$$q_i = L_{ij}^{-1} \phi_j. \quad (3.21)$$

Then $\phi_j = \phi_{ave} - \frac{1}{2}$ volt for the outer conductor and $\phi_j = \phi_{ave} + \frac{1}{2}$ volt for the inner conductor, where ϕ_{ave} is the average voltage to be calculated for the structure. Then

$$q_i = -q_{n+1-i}$$

and

$$C = \left| \sum_{i=1}^{n/2} q_i' \right|. \quad (3.22)$$

Since 3.21 is a system of linear equations,

$$q_i = L_{ij}^{-1} \phi_{0j} + \phi_{ave} L_{ij}^{-1} u_j \quad (3.23)$$

where ϕ_{0j} and u_j are vectors. $\phi_{0j} = \frac{1}{2}$ for $i > n/2$ and $\phi_{0j} = -\frac{1}{2}$ for $i \leq n/2$. $u_j = 1$ for all j . Let

$$q_{0i} = L_{ij}^{-1} \phi_{0j}. \quad (3.24)$$

Then

$$q_i = q_{0i} + \phi_{ave} L_{ij}^{-1} u_j \quad (3.25)$$

We know that $\sum_{i=1}^n q_i = 0$ from charge pairing. Then

$$0 = \sum_{i=1}^n q_{0i} + \phi_{ave} \sum_{i=1}^n L_{ij}^{-1} u_j$$

and we may solve for ϕ_{ave} :

$$\phi_{ave} = - \left(\sum_{i=1}^n q_{0i} \right) / \left(\sum_{i=1}^n L_{ij}^{-1} u_j \right). \quad (3.26)$$

The capacitance is then given directly by

$$\underline{C} = \sum_{i=1}^{n/2} (q_{0i} + \phi_{ave} L_{ij}^{-1} u_j) \quad (3.27)$$

from which Z_0 follows.

These facts can be shown to be reasonable by examining the individual elements and their interactions. As expected, it is also possible to show that the average voltage is proportional to the potential difference. If $q_i = -q_{n+1-i}$ the average voltage for

a matched pair, neglecting other charges in the vicinity, is

$$\phi_{ii_{ave}} = \frac{1}{2} \left(\frac{q_i}{2\pi\epsilon} \right) \left\{ \ln \left(\frac{r_{i,n+1-i}}{w_i} \right) - \ln \left(\frac{r_{n+1-i,i}}{w_{n+1-i}} \right) \right\}. \quad (3.28)$$

The potential difference is

$$\begin{aligned} \phi_{ii_{diff}} = \left(\frac{q_i}{2\pi\epsilon} \right) \left\{ \ln \left(\frac{r_{i,n+1-i}}{w_i} \right) + \ln \left(\frac{r_{n+1-i,i}}{w_{n+1-i}} \right) \right\} \\ + 2 + 2\ln 2 \}. \quad (3.29) \end{aligned}$$

Solving for $(q_i/2\pi\epsilon)$,

$$\phi_{ii_{ave}} = \left[\frac{\phi_{ii_{diff}}}{2} \right] \frac{\ln \left(\frac{w_{n+1-i}}{w_i} \right)}{\ln \left(\frac{r_{i,n+1-i}}{w_i} \right) + \ln \left(\frac{r_{n+1-i,i}}{w_{n+1-i}} \right) + 2 + 2\ln 2} \quad (3.30)$$

All quantities except ϕ_{ave} and ϕ_{diff} are fixed by the given geometry, and unless $w_{n+1-i} = \phi_{ave} \neq 0$. The voltages of this pair on elements j and $n+1-j$ in the vicinity are

$$\phi_{ji} = \frac{q_i}{2\pi\epsilon} \left\{ \ln \left(\frac{r_{j,i}}{r_{j,n+1-i}} \right) + \dots \right\} \quad (3.31)$$

and the average voltage on pair $j, n+1-j$ due to $i, n+1-i$ is

$$\phi_{ave_{ji}} = \frac{1}{2} \left(\frac{q_i}{2\pi\epsilon} \right) \left\{ \ln \left(\frac{r_{ji}}{r_{j,n+1-j}} \right) - \ln \left(\frac{r_{n+1-j,i}}{r_{n+1-j,n+1-j}} \right) \right\} \quad (3.32)$$

Again, if the pair of positive charges is spaced differently to the pair of negative charges, this contribution to the average voltage is not zero, and it is proportional to the potential difference $\phi_{ii_{diff}}$.

If the charge distribution were chosen correctly, the

resultant average voltages would all be the same*. For correctly spaced charges,

$$\phi_{i\text{ave}} = \sum_{j=1}^{n/2} \phi_{\text{ave}_{ij}} = \frac{1}{2} \sum_{j=1}^n \phi_{\text{ave}_{ij}}, \quad (3.33a)$$

and these averages would all be equal to that given by Eq. 3.26.

The average voltage in 3.26 for incorrectly placed charges is

$$\phi_{\text{ave}} = \frac{1}{2n} \sum_{i=1}^n \sum_{j=1}^n \phi_{\text{ave}_{ij}}. \quad (3.33b)$$

It was found when a computer program was developed both to locate and to solve for the charges, that the average voltage for a pair of parallel charge arrays was zero. This is predicted by Equations 3.28 to 3.32, since the spacing of the positive strips was the same as for the negative strips. When a closed coaxial system was used, the outer conductor shielded the inner one and the applicator had an average potential very nearly equal to half the potential difference.

(d) Correction of Charge Placement

If the charges are not correctly placed, some error remains in the values computed for C and ϕ . Experimental results showed the capacitance error to be about $1\frac{1}{2}\%$ for simple evenly spaced charge distributions on square 47 ohm coaxial line. However, after equalizing the magnitudes of the two charges on each pair (which makes the situation worse), errors in voltage of up to 20% remained. Since the electric field is the gradient of voltage

* For spacings chosen incorrectly, the potential difference is still the same for each pair, if the method of moments is used to obtain q_j as in Equations 3.21 to 3.26.

and since the potential difference between image charges is correct, its error is less. However, the percentage error in ξ^2 is double that in the fields themselves, and ξ^2 is also sensitive to local charge errors.

To remedy the error in charge placement, we must examine the physical meaning of the line charges. The L_{ij} matrix has been set up so that q_j is assumed to be paired by a charge $-q_j$ at location $n+1-j$. We then set $L_{i,n+1-j}=0$ if i and $n+1-j$ are on the same conductor. The line charges computed represent a strip with magnitude q_j equal to $\sigma_j w_j$. The location of the image charge is nearly, but not exactly, correct and the log dependence of the L_{ij} makes them insensitive to shifting of remote charges. Thus one may reduce the width of q_j to compensate for deviations in q_j from $\frac{1}{2}(q_j - q_{n+1-j})$. It has been found practical to leave the distribution on the centre conductor fixed, since the corners affect the field strengths strongly. One may then make double the indicated correction in widths of the strips on the outside conductor.

$$\begin{aligned} &\text{Letting } q_j' \text{ represent the average charge for the pair } q_j, \\ q_j' &= \frac{1}{2} (q_j - q_{n+1-j}). \end{aligned} \quad (3.34)$$

Then the new width w_j' is given by

$$w_j' = (1 + \beta(q_j - q_j')/q_j') w_j, \quad (3.35)$$

where β is a multiplication factor; which is different from 2 because ϕ_{ave} will change slightly. The pairing changes as w_j is adjusted and the total width must be equal to the distance around the outer boundary.

When each iteration, consisting of calculation of w_j followed by calculation of q_j' , has been performed, the matrix L_{ij} may be used with q_j' to give the voltages on the conductors. In other words,

$$\phi_{i_{ave}} = \frac{1}{2} (L_{ij}q_j' + L_{i,n+1-j}q_{n+1-j}') \quad (3.36)$$

The error $e_{\phi_i} = (\phi_{i_{ave}} - \phi_{ave})$ may be used to check for ill-conditioned matrices and/or inaccurate charge distribution. The voltage difference is always correct if the matrix is well-conditioned*, and this may be used to pin-point the source of the error. When the charges are used to calculate the fields, the tangential electric field will be zero. Since this implies that adjacent strips are at the same potential, the two facts are equivalent. If the charges are not equal and opposite, the product $q_j = \sigma_j w_j$ must be changed. This was the criterion used in the program, since ξ^2 is sensitive to local errors.

To use the program to calculate its own β , we first determine a charge error for each strip pair. Let the error be given by

$$e_i = (q_i - q_i')/q_i' \quad (3.37)$$

* See for example, McCalla, Introduction to Numerical Methods and Fortran Programming, J. Wiley 1967, p.176. Bostian's word of warning⁽¹⁰⁾ is even more valid for infinitely long line charges than for point charges. Serious errors arose from ill conditioned matrices using single precision arithmetic. However, the voltage difference check showed that typical accuracies of six figures could be obtained by using double precision arithmetic on the IBM 360/67 system during matrix inversion. Longer iterative procedures such as the Gauss Siedel method were not necessary.

where q_i is the charge calculated during an iteration, including the effect of the average voltage as in the previous section. q_i' is this charge averaged with its image charge. The optimum acceleration for an iteration occurs when

$$\bar{e} = \sum_{i=1}^{n/2} e_i \gamma_i = 0 \quad (3.38)$$

where $\gamma_i =$

$$\begin{aligned} & 1 \text{ if } e_i \text{ was previously positive} \\ & 0 \text{ if } e_i \text{ was previously negative} \end{aligned} \quad (3.39)$$

The β satisfying this criterion would give all $e_i = 0$ if the $\frac{\partial L_{ij}}{\partial w_i}$ were constant with respect to q_i and w_i . To correct β from β_1 to β_2 in two successive iterations, we use β_1 to correct q_{i_1} to q_{i_2} . Then we examine the magnitude of the correction. If we use β_1 we obtain an error e_{i_2} . Summing

$$\bar{e}_1 = \sum_{i=1}^{n/2} e_{i_1} \gamma_1 \quad (3.40)$$

and

$$\bar{e}_2 = \sum_{i=1}^{n/2} e_{i_2} \gamma_2$$

The actual correction for each strip is equal to $(e_1 \gamma_1 - e_2 \gamma_2)$ and if this is proportional to β_1 , we have that

$$(e_1 \gamma_1 - e_2 \gamma_2) / \beta_1 = \text{const.} \quad (3.41)$$

The desired correction gives no averaged error, or

$$(e_1 \gamma_1) / \beta_2 = \text{const.} \quad (3.42)$$

Then by summing over i and dividing Eq. 3.41 by Eq. 3.42,

$$\beta_2 = \beta_1 \frac{\sum_{i=1}^{n/2} |e_{i_1}|}{\sum_{i=1}^{n/2} |(e_{i_1} - e_{i_2})|} \quad (3.43)$$

Eq. 3.43 gives a new acceleration factor for the next iteration, or alternatively for correction of the previous adjustment of w_i . If the error \bar{e}_2 is less than \bar{e}_1 and β is nearly constant, convergence is most rapid when β_p is used in iteration $p+1$. As expected, β is about 2, typically 1.7. When there were large errors, the corrections were scaled down until the largest adjustment to a strip was about 66.7%.

Using the methods of this section, small errors converged rapidly, i.e. a voltage error of 6% converged to 0.3% in two iterations, starting with a β of 2 and recalculating it once. Simultaneously, charge errors of 32% converged to 1.8%. The method loses speed of convergence rapidly for errors over 50% and for applicator cross-sections where the width was very much greater than the height. In addition to limiting the corrections it was necessary to start from a nearly square structure and progressively make the structures wider. Increments of 20% were used, which was also a good interval for plotting the results, and each corrected distribution was used for the

initial strips on the outside conductor of the next cross-section.

Theoretically, Newton's method could be adapted in matrix form, using first derivatives of either ϕ_i or tangential electric field. When this was tried, it was found that very ill-conditioned derivative matrices resulted and the errors were drastic. The method based on adjusting total strip charge was much more successful.

(e) Calculation of Applicator Parameters

When the charges have been calculated and the error criterion met, we may calculate ξ^2 from Equations 3.1, 3.2, 3.3, and 3.11 by placing a grid of points in the interior. The total $|E|^2$ from all charge pairs is obtained for each point and multiplied by the cross-sectional area around the point, and a summation is used instead of the integrals in Equations 3.1 and 3.2. For a true TEM structure,

$$\hat{E}_i \cdot \hat{E}_i^* = \left(\frac{\sigma_i w_i}{2\pi\epsilon}\right)^2 \left\{ \frac{x^2}{r^4} + \frac{y^2}{r^4} \right\} \quad (\text{no summation}) \quad (3.44)$$

where $x = (x_p - x_\sigma)$, $y = (y_p - y_\sigma)$ and $r = \sqrt{x^2 + y^2}$ as shown in Figure 3.4. The total squared field at point p_j is then given by

$$(\hat{E} \cdot \hat{E}^*)_j = \left(\frac{1}{2\pi\epsilon}\right)^2 \left\{ \left(\sum_{i=1}^n q_i \left(\frac{x}{r^2}\right)_{ij} \right)^2 + \left(\sum_{i=1}^n q_i \left(\frac{y}{r^2}\right)_{ij} \right)^2 \right\}. \quad (3.45)$$

If k points are evenly spread over the main area S and ℓ points over the web area, ΔS and Δa_i is the area around point i ,

$$\xi^2 = \left(\frac{k}{\ell}\right) \left(\sum_{i=1}^{\ell} (\hat{E} \cdot \hat{E}^*)_i \Delta a_i \right) / \left(\sum_{j=1}^k (\hat{E} \cdot \hat{E}^*)_j \Delta a_j \right). \quad (3.46)$$

The power carried in the guide for a voltage difference ϕ_{diff} is then

$$P = \frac{1}{n_0} \left(\frac{1}{k}\right) \left\{ \sum_{j=1}^k (\hat{E} \cdot \hat{E}^*)_j \Delta a_j \right\} \quad (3.47)$$

Alternatively,

$$P = (\phi_{\text{diff}})^2 / Z_0 \quad (3.48)$$

which can be compared to the results of 3.47 to check the computer program. To check a particular design for breakdown problems, we may use the square root of Eq. 3.45, scaled to some forward power, i.e. 1.0 kW using Eq. 3.47. The maximum E in the interior will be somewhat less than that at the corners if they are not rounded. This means that the value given by a grid is an approximate value only, applying to rounding radii of the order of the grid and inter-charge spacing.

3.3 Results

Two computer programs were used to produce design maps for the rectangular TEM structure. The first was an implementation of the mathematics of the previous five sections. This main program accepted as input parameters the dimensions of the structure and several control commands, and was run for a wide variety of applicator cross-sections, producing a deck of output cards carrying Z_0 and ξ^2 data. A second program was written to interpolate linearly between the members of this set of cross-sections. This program was capable of rearranging the data for presentation on various sets of axes.

The main program also printed sheets of data, giving the applicator dimensions, Z_0 , the number of sampling points above and to the side of the centre conductor, the error in Poynting's vector (obtained by comparing Equations 3.47 and 3.48), the factor ξ^2 for a web above as well as to the side of the centre conductor, and the filling factor. This information could be used to calculate attenuation and to predict its accuracy. In addition, the maximum electric field was printed for a forward power of 1 kW. This was simply the largest field found on the grid of measurement points. It is about the same as for a structure in which the corners are rounded with a radius equal to the spacing of the charges on the centre conductor if the grid of measurement points has the same spacing. The spacing could be checked by referring to the printed output, and adjusted accordingly. To obtain better accuracy, the charges may be placed closer together on a quarter circle at the corners.

It is likely that the present method is accurate to about 50% when calculating breakdown power levels.

For the interpolation step, a matrix of applicator cross-sections was obtained by varying the upper and lower gaps by 20% steps. Including images, 80 charges were assumed per cross-section. The inner conductor was square and was assumed to be 1 meter on a side, but the dimensions may be taken to be any convenient units. The spacing is 1/20 of the inner conductor, so fringing fields to the side of it are fairly accurately determined. In the computer program, ϵ_0 was set to $1/2 \pi$. This means that the charges were not expressed in Coulombs but may be converted by dividing by 18×10^9 .

Figure 3.5 shows the charges distributed over one quadrant of a typical applicator and the voltages induced in the interior at the sampling points. Figure 3.6 shows the same applicator with the magnitudes of the electric fields that the main program calculated. The charges on the outer conductor have been iteratively relocated and the outer corners have very little charge. The corners of the inner conductor have about twice the charge density that the centres have. The measurement mesh chosen was too coarse to determine the maximum electric field, but the corner has a high gradient. Also apparent is the field concentration near the centre conductor, indicating that the faces of the conductors are not acting like a parallel plate capacitor, as they do for smaller gaps. If the applicator is scaled in size, ϵ^2 , Z_0 and the voltages are unchanged. The

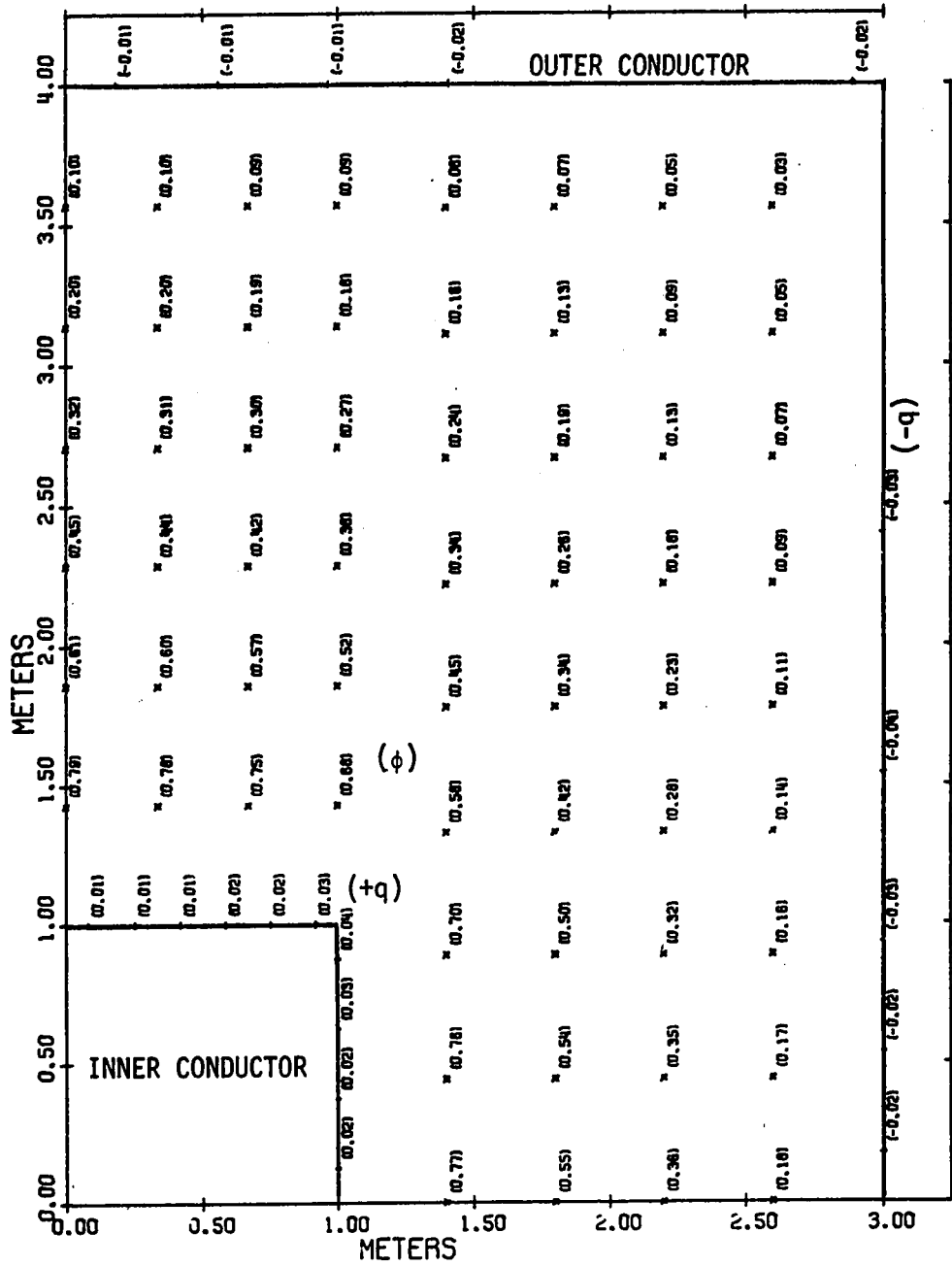


Figure 3.5 VOLTAGES IN TEM APPLICATOR

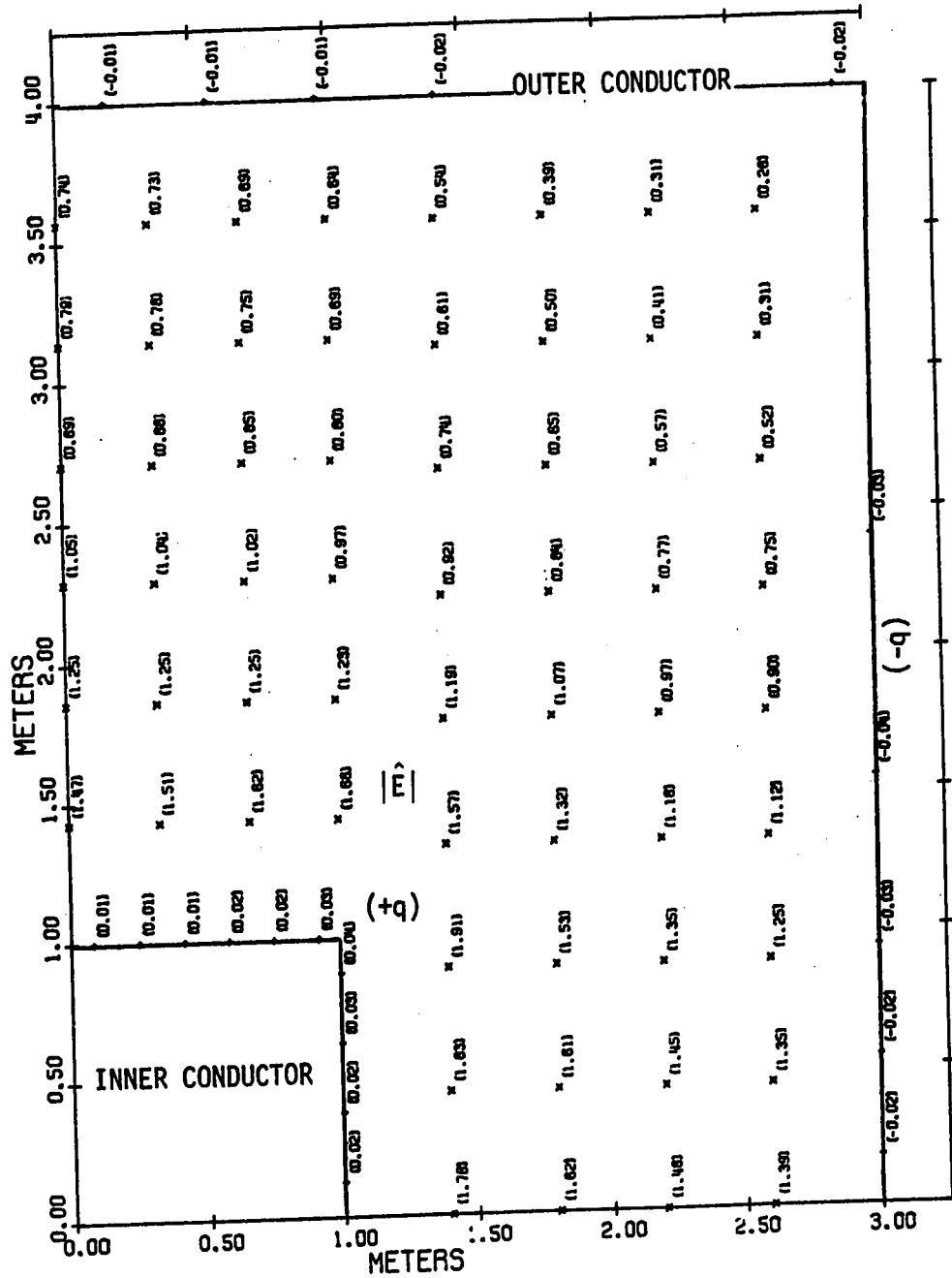


Figure 3.6 ELECTRIC FIELDS IN TEM APPLICATOR

electric fields are inversely proportional to the scaling factor and directly proportional to the applied voltage. For convenience in computation, the dimensions shown are doubled, while the fields are calculated for a normal-sized structure, including all four quadrants.

Figures 3.7 to 3.12 are maps produced by the interpolation program. The first four charts are contours of various parameters plotted against the dimensions of the structure. With the exception of Figure 3.10 for Z_0 , these maps are not in a convenient form for design but they show how the various parameters change as the designer changes the vertical and horizontal gaps, corresponding to c , and d respectively of Figure 2.9. The third gap, through which the web passes, is assumed to be very small.

A deck of 136 input cards was converted to a set of 6 matrices of size 16 by 16 whose elements were input or calculated data from the main program. The interpolation program searched for contours between these points. Each input card was accompanied by a card bearing the error calculated in the main program which was used to correct ξ . Since most of the power is carried in the narrow gap, it was assumed that the same percentage error occurs in ξ^2 as in Poynting's vector. For almost all the cross-sections the uncorrected error was less than 10% and only for very small gaps, or Z_0 of about 12 ohms, was the error even visible on the graphs.

Figure 3.7 shows the filling factor. All the other parameters have been normalized to the dimensions of the centre conductor, so for F , the web is assumed to be as thick as the centre conductor

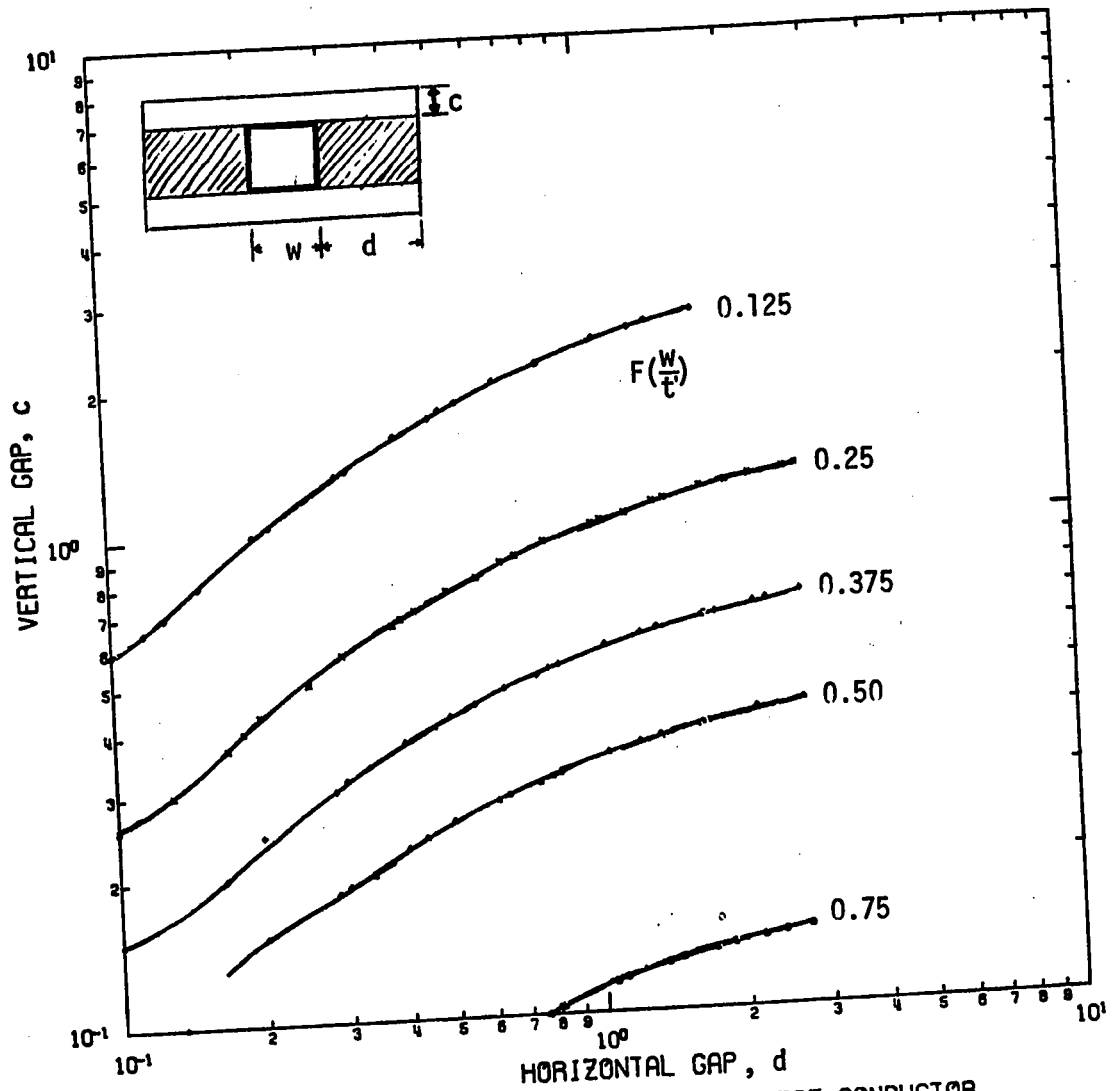


Figure 3.7 FILLING FACTOR NORMALIZED TO CENTRE CONDUCTOR

- The normalized filling factor $F(\frac{w}{c})$ is used. ΔS is the cross-hatched area to the side.
- w taken to be 1 unit, c and d follow.

is high. This does not imply that a large gap occurs in the centre conductor, but that the computed values of F and $F\xi^2$ must be multiplied by t/w where t is the web thickness and w is the centre conductor height. Thus the plots show the variable $F(\frac{w}{t})$. These contours tend to become constant for very wide webs. The scatter is due to the interpolation program.

In Figure 3.8 the quantity ξ^2 is plotted. For very narrow applicators the web is in the high field region. The interior area can be very large if the vertical gap c is large. Thus ξ^2 can increase without limit. The contours tend to go upward at 45° except for very large horizontal gaps, where the concentration of fields at the side of the centre conductor causes them to level out. Some scatter is visible on the $\xi^2 = 0.125$ contour.

The attenuation is proportional to the product of ξ^2 and $F(\frac{w}{t})$ so this is plotted in Figure 3.9. There are some dramatic changes in direction of these contours, and the product is less than unity. (If $F(\frac{w}{t})\xi^2$ were unity, it would imply that all the power is carried beside the centre conductor.) This plot, while it tells the designer how to make an applicator with a desired loss, does not indicate how to choose among the infinite number of possible combinations on one of the contours.

In Figure 3.10 the contours of constant characteristic impedance (Z_0) are mapped. Along one of these contours are various applicators which can be cascaded without reflections. These contours cut at a large angle across the contours of Figure 3.9, and thus permit a more intelligent choice of gap widths. In the

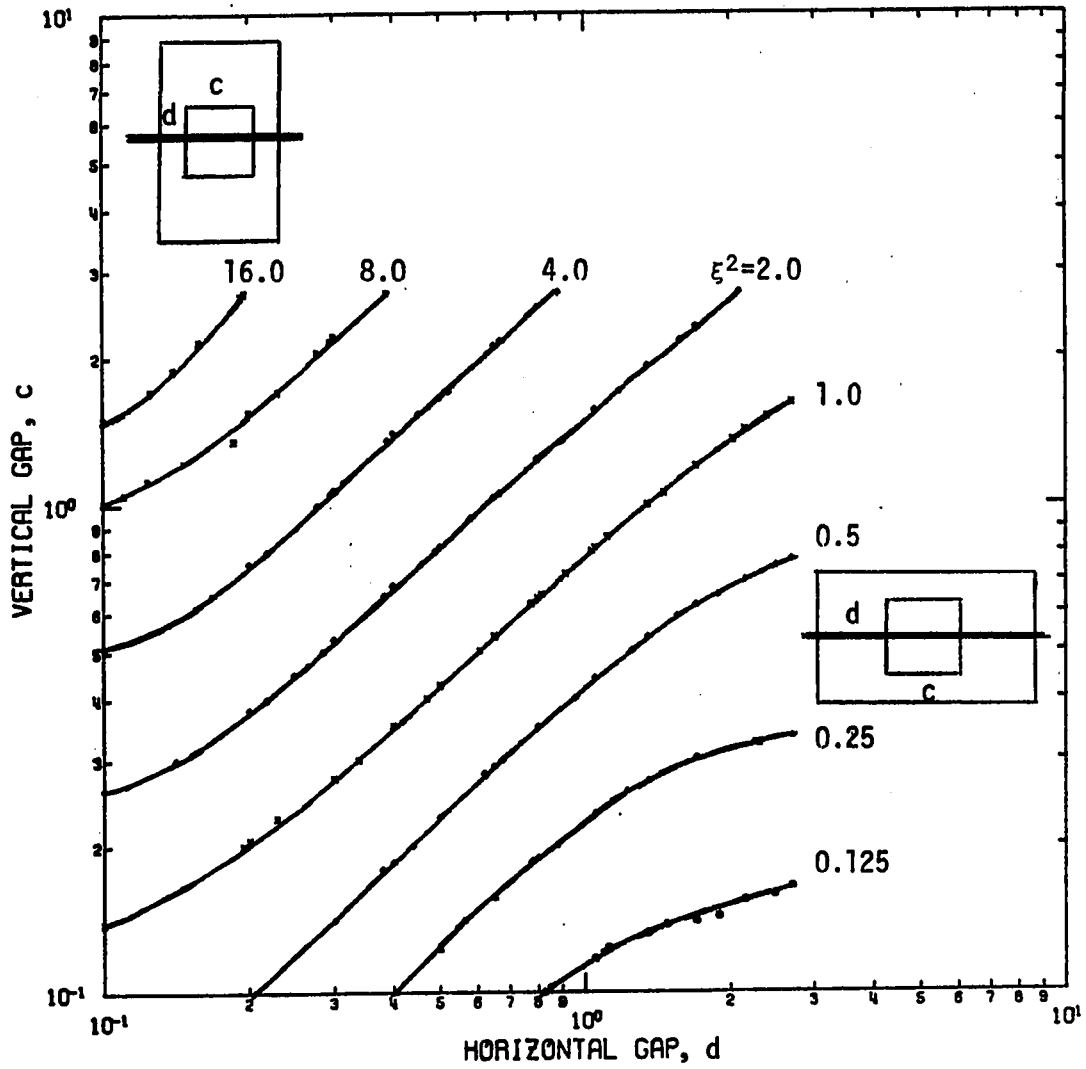


Figure 3.8 POWER CONCENTRATION IN WEB REGION

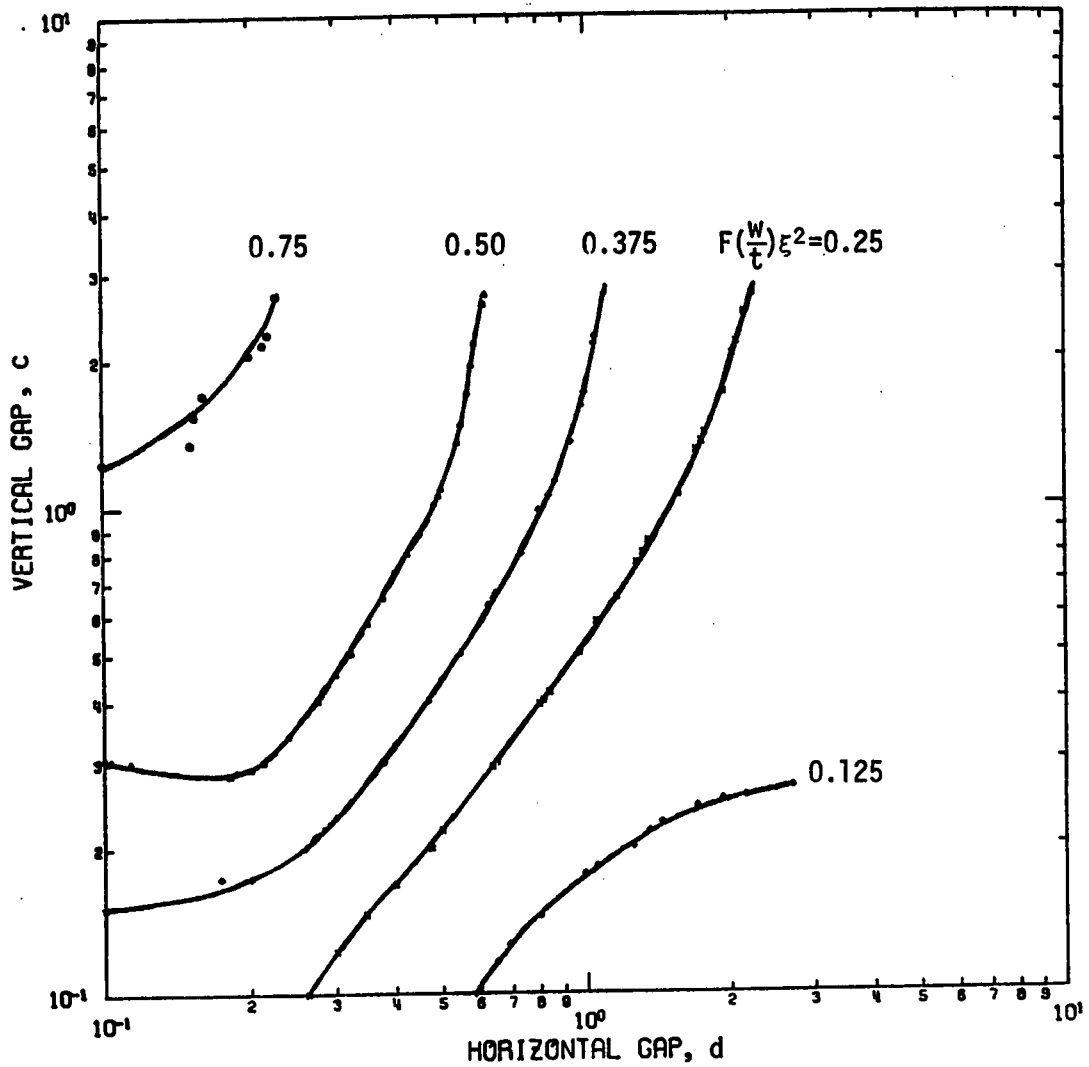


Figure 3.9 POWER CONCENTRATION FILLING FACTOR PRODUCT

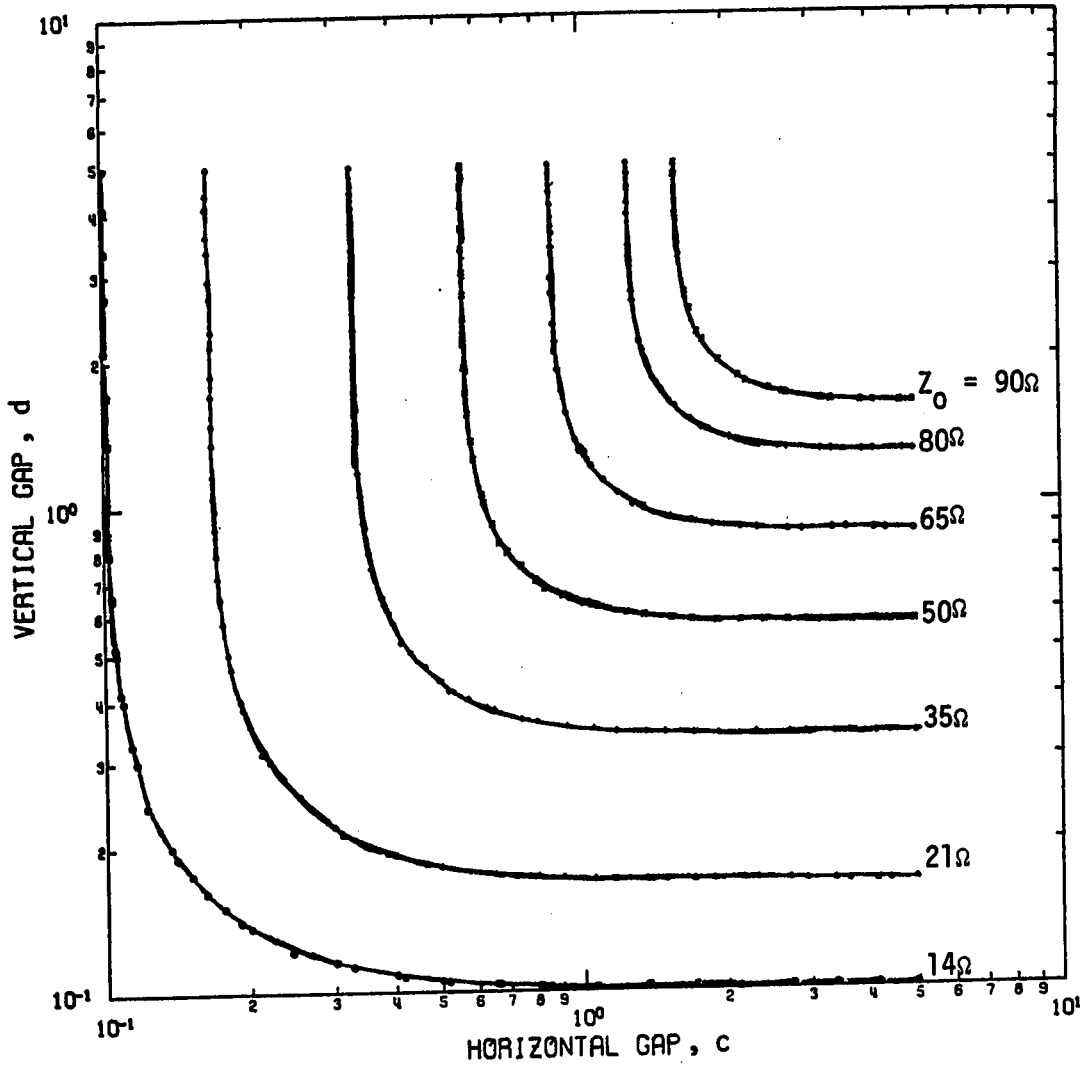


Figure 3.10

SPACING FOR CONSTANT IMPEDANCE

- Using this map, the reflection coefficient may be calculated.

region to the right of the diagonal through the plot, the upper gap dominates the characteristic impedance and the designer can choose the horizontal gap for attenuation without affecting the characteristic impedance significantly.

Since the applicator should be reflectionless, the interpolating program also prepared data for ξ^2 and the $F(\frac{W}{T})\xi^2$ product along the Z_0 contours. In the next two figures, it is plotted. The independent variable is taken to be the horizontal gap and the vertical gap may be determined from Figure 3.10. In Figure 3.11 the ordinate is ξ^2 and in Figure 3.12 it is the $F(\frac{W}{T})\xi^2$ product.

Again, ξ^2 can increase without limit while the $F\xi^2$ contours are limited to unity. In their middle regions the ξ^2 curves behave as $1/d^2$ while the $F\xi^2$ curves behave as $1/d$. For small d the departure of the $F\xi^2$ curves from $1/d$ behavior is due to the departure of the Z_0 contours from constant upper gap c . For large d , the fringing fields near the side of the centre conductor carry more power than the rest of the web region and the side wall of the outer conductor does not appreciably affect these fields. Thus there is a minimum attenuation which decreases as the upper gap is decreased, giving reduced Z_0 . In Chapter 2, it was shown that the rectangular hyperbola region gives this applicator its advantage. These graphs show that the low impedance contours give the designer the widest range of attenuation control.

To use Figure 3.12 with constant upper gap c , a dotted line has been drawn across the chart showing the limit of the low reflection region. This line corresponds to the diagonal in

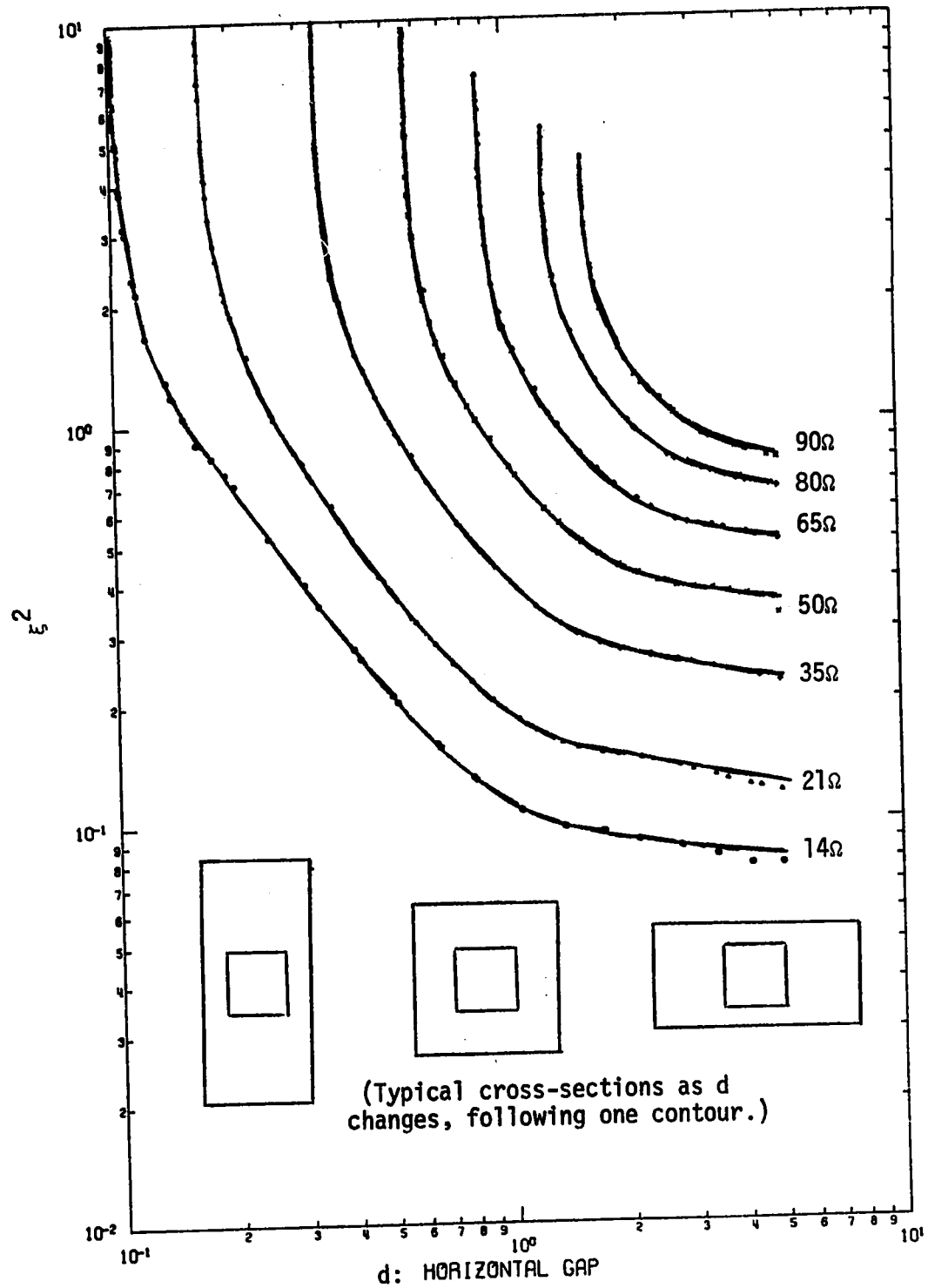


Figure 3.11 POWER CONCENTRATION AT CONSTANT IMPEDANCE

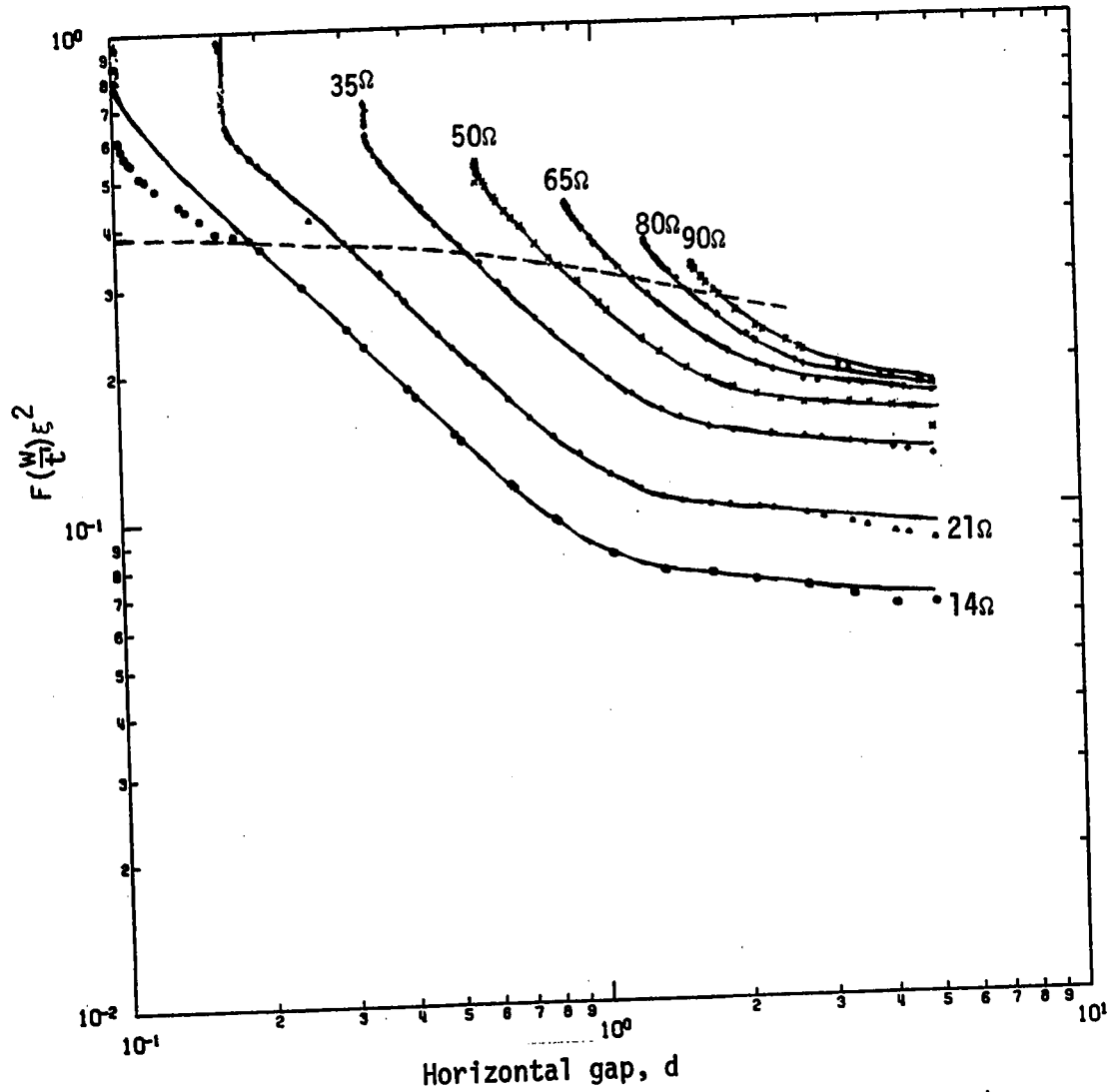


Figure 3.12 Chart for Web Power Absorption Factor - no web gap

- The dotted line is the boundary below which the upper gap may be made relatively constant.

Figure 3.10 and along it the characteristic impedance will be 48% too low, giving -9 db reflected power. The chart errors are minimal except in extremely wide applicators, where the matrices were ill-conditioned. This error is visible along the 14 ohm contour. At the departures from hyperbolic behavior at low attenuation the errors are very small and the useable ranges are accurately given.

To test the accuracy of the main program, a short section of rectangular coaxial line was constructed. Using an L-C meter and a time domain reflectometer, its characteristic impedance was found to be 46.6 ohms \pm 0.5%, when the side and upper gaps were equal. The main program predicted 46.5 ohms, which agrees with Metcalf⁽⁴⁸⁾. As the side gap was adjusted from 1 to 4 times the upper gap, 2 to 1 attenuation control was observed, which agrees very closely with Figure 3.12.

The upper and lower gaps are normally used to control the structure, but if the web gap is large, the electric fields to the side are reduced. To check for this, the upper gap was fixed while a variety of web gaps were used in the main program. This results in applicators which do not follow a Z_0 contour over the entire adjustment range, but do so if this range is kept below the limit shown in Figure 3.12. In Figure 3.13 the upper gap was set to 0.2 of the centre conductor and the web gap was 0, 1/10, 1/4, 1/3, and 9/10 of the centre conductor. The ordinate is the $F(\frac{W}{C})\epsilon^2$ product. Five to one attenuation control can be attained with very small web gaps but the presence of even moderately wide web gaps seriously degrades this control. The

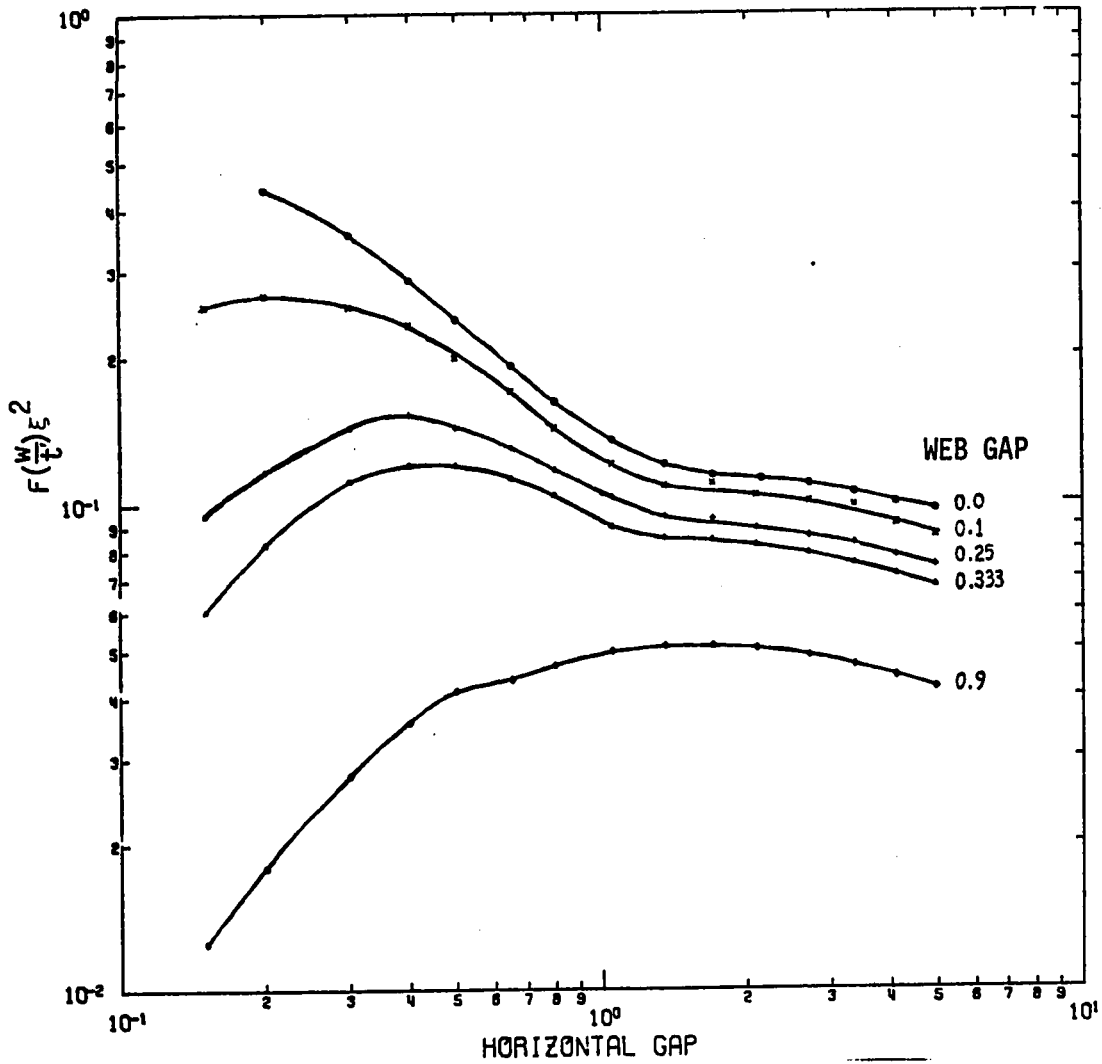


Figure 3.13 **Effect of Web Gap on Power Absorption**

-Upper Gap = 0.2m, about 25 ohms. Web gap = 0, 1/10, 1/4, 1/3, 0.9m, centre conductor assumed equal to 1m.

lower attenuation limit is also reduced by very wide gaps, a fact that can be used to further reduce the attenuation.

3.4 Design Example

To construct a simple applicator which will accept a wide variety of loads, several passes should be made over the web at increasing attenuation. This will permit uniform heating at first, with gradual increase of attenuation when the energy is partly absorbed. The efficiency will be kept high by the increased attenuation.

If a $3/16$ " gap is used for web transport, Figure 3.13 shows that the centre conductor should be at least 2" wide. From Figure 3.10, the 20 ohm structure has a normalized gap of about 0.17 above a unit centre conductor, or 0.33" spacing to the upper ground plane. Checking Figure 3.12, little is gained from side spacings greater than 2 units or 4". By staying below the dashed line in this figure, we may avoid varying the upper spacing, which would otherwise be needed to maintain a constant Z_0 . However, we lose a factor of 2 in attenuation control, and a pass will be included with a smaller side gap than the vertical gap. To gain a further factor of 2 in the first pass, we may add one section with a very large gap for the web. This also reduces the leakage.

The resulting applicator is shown in Figure 3.14. The centre conductor is 2" square and, except for the last pass of the coaxial line, the upper gap is $1/3$ ". On the first pass, the side gaps are 4" and the web gap is $1\ 1/2$ ". On the second pass the web gap is reduced to $3/16$ ", doubling the attenuation. On the third

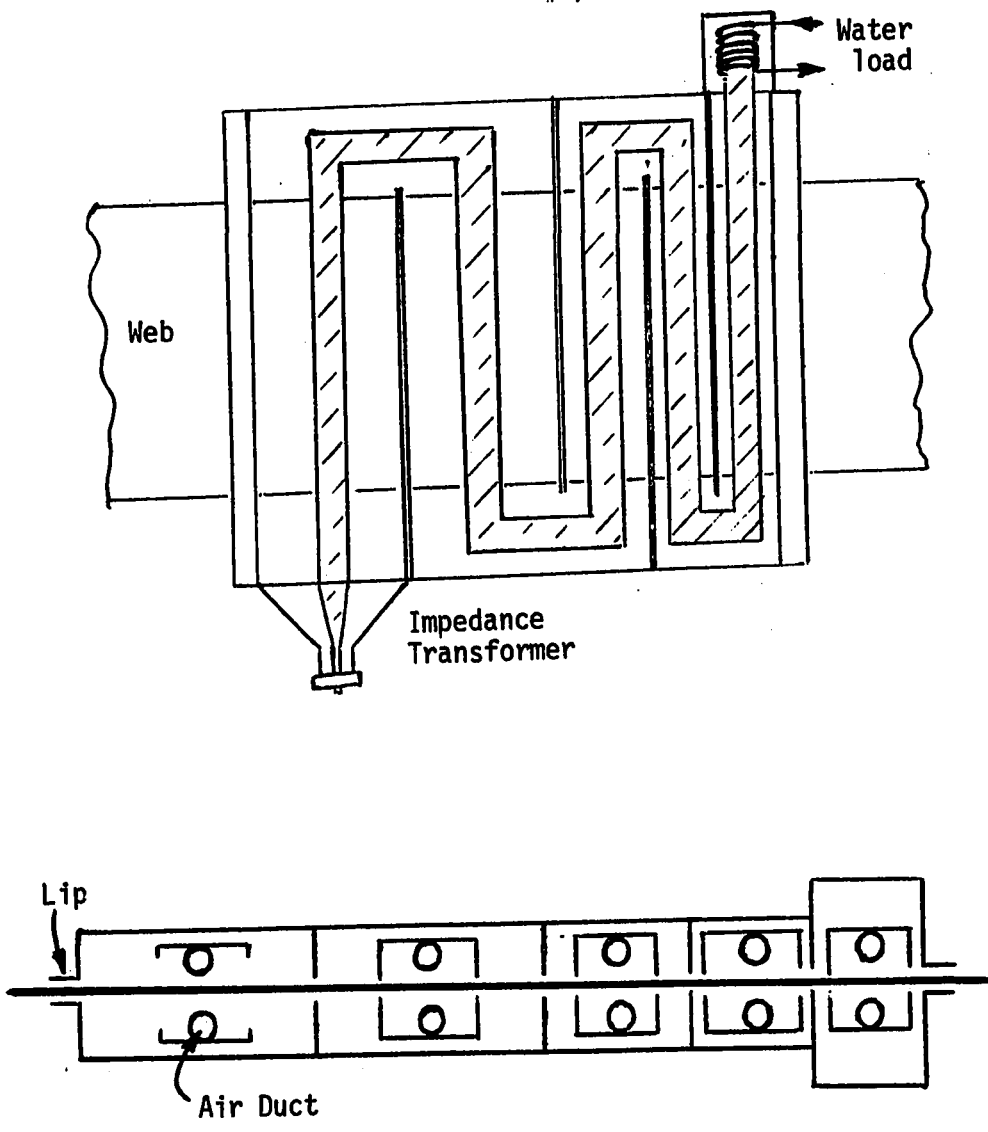


Fig 3.14 Rectangular TEM Applicator Design

pass the side gap is reduced to 1" and on the fourth and fifth pass to 1/3". On the fifth pass the upper gap is increased to 1"*. The applicator designed here is only 26" long and 4" high. Its width need only be about 4" wider than the web to be dried.

The rest of the design consists of choosing the water load, matching transformer and the lips to prevent leakage. Air must be provided and it is probably advisable to run 1/2" polyethylene tubing inside the centre conductor rather than simply blowing in air. This tubing has the advantage of supplying air more evenly along the length of the web, and holes in the tubing will provide jets which impinge vertically on the web rather than flowing over it in a laminar pattern. This could also provide for air suspension of the web.

In the low attenuation passes of this design, the main program predicts 2000 volts RMS per cm at 10kW. Since the mesh used was as coarse as that shown in Figures 3.5 and 3.6, this figure is optimistic, and applies to a radius of curvature of about 1/4" on the corners. Allowing for double the predicted field, i.e. 1/8" radius of curvature, the structure could probably carry 2 1/2kW with 2000 V/cm RMS field strength. Circular 50 ohm 1 5/8" coaxial line can also carry 2 1/2kW at 2000 V/cm RMS field strength. S-band waveguide can carry over 100 kW of power at the same RMS field strength and L-band waveguide can carry over 1 MW.

* There are two reflections at the ends of the square pass which will cause up to -6 db of reflected power, depending on frequency. This has been tolerated to simplify the design. Also; in the next chapter it will be shown that using two passes at each attenuation sharply reduces inhomogeneity of heating, and more than one mode can exist at 2450 MHz.

CHAPTER FOURINHOMOGENEITIES AND ATTENUATION IN TRAVELLING WAVE APPLICATORS

In Chapter 2 it was shown that attenuation could be controlled in TEM structures and in Chapter 3 detailed design data were produced for this purpose. In this chapter information will be given to select the optimum attenuation.

An electromagnetic field can give uniform heating of homogeneous webs if there is no reflected wave to cause interference patterns and if the energy in the incident wave does not become absorbed too near the edge of the web. In addition, if a web has wet spots they absorb more power than the rest of the web. This fact permits levelling of the moisture content of sheets such as paper⁽⁷³⁾. Again the field must be kept uniform. When large reflection coefficients occur in a travelling wave applicator, or when the web attenuates the wave too rapidly, the result will be poor product quality and possibly fires. A more accurate technique is needed to predict inhomogeneous heating in wet webs.

Heenan⁽³⁵⁾ treated the situation where the evaporating web moves in the same direction (concurrent) or in the opposite direction (countercurrent) that the microwave power travels. He did not go into detail about temperature, vapor pressure and air flow; or about reflections. To include the latter causes of inhomogeneities, it will be desirable that the web be stationary. This is batch heating, which is not used in practice, but which gives a worst-case inhomogeneity prediction since the motion of the web will even out the heating. If the predicted inhomogeneity is low, Heenan's theory can be adapted to crosscurrent motion by considering slow waves.

4.1 Drying of Wet Webs

In conventional hot air drying there are two stages of moisture removal, called constant rate drying and falling rate drying. The moisture is removed first from the surface of the web, and capillary action keeps the surface supplied with moisture even though the density of the web is falling. During this constant rate phase, heat is supplied directly to the wet surface and it is usually carried by the same air which carries away the water vapor. Later, the evaporation is carried out inside the material and heat is supplied more slowly to the water. This is because the heat must penetrate a dry thermally insulating layer. This is called the falling rate stage.

Because energy is absorbed from the electromagnetic fields, mainly by the water itself, migration of the water in the material has little effect on the power absorbed. If the power is travelling forward only in a travelling wave dryer, the evaporation rate begins falling as soon as drying begins*. However, the rate of diffusion of water vapor inside the web will limit the transport of vapor, resulting in a higher temperature. Thus a wet surface is advantageous, but not as much so as in hot air drying.

The moisture content above which free liquid water is mobile in a web is called the fibre saturation point[§]. Above this point ϵ_r'' of the water component of a web is approximately the same as for free water, while below it the large percentage of bound water causes increased ϵ_r'' (ϵ_w'')^{(45), (62)}. For wet webs, high temperatures reduce

*After transient conditions disappear: see later.

§For Douglas fir, below about 50% dry weight or 0.2 gm water per ml.

ϵ''_W while for drier webs high temperatures can increase it⁽⁶¹⁾. This means that there is the danger of thermal runaway and fires if dry spots develop, and the applicator should be designed to prevent inhomogeneities.

While the constant rate drying stage is not present in travelling wave microwave driers, the same range of moisture content permits the use of two simplifying assumptions; namely that the required vapor pressure (and therefore temperature) is determined by surface conditions and that the lossiness of the web is determined by free water^{*}. Below fibre saturation these assumptions break down, and the required vapor pressure rises significantly at about the same time as ϵ''_W does. The analysis of this chapter will predict inhomogeneities in this range, thus determining whether there are spots which have dangerously low moisture content while other parts of the web need additional drying.

Another analysis of inhomogeneity[§] assumes that the web is uniform, that there are no changes in temperature, that no reflections occur and particularly that no evaporation takes place. This analysis will be derived in Section 4.3 by using simplifications of the more complete treatment.

*If a multimode cavity is used, the electric field can be increased sufficiently to give constant rate drying⁽³¹⁾. This occurs automatically, even below the fibre saturation point, if the efficiency is kept high and the magnetron power output is constant.

[§]Williams and Warner's second figure⁽⁷³⁾.

It would be possible to relate vapor pressure⁽¹⁾, power absorption per unit length, dielectric properties of water^{(26),(57)},⁽⁶⁸⁾, and other parameters of a specific system to predict its complete behavior while heating a wet, moving web. However, in the following section it is assumed that the web is batch heated, and to further reduce the complexity, the remaining variables can be normalized to give only two independent variables; the initial equilibrium temperature and a product of filling factor, moisture content and field concentration factors. The result is a moisture contour which is initially level, becomes uneven as the edge of the web nearest to the magnetron is dried, and is eventually levelled out when the energy passes further over dried parts of the web.

4.2 Energy Deposition and Drying for Very Wet Webs

(a) Power Applied

The power dissipated in the web per unit length is

$$P_{\text{web}} = \epsilon_0 \rho \epsilon_W'' \omega \int_{\Delta S} (\hat{E} \cdot \hat{E}^*) dS \quad (4.1)$$

$$= \epsilon_0 \rho \epsilon_W'' \omega \xi^2 \psi^2 \eta P_f F \quad (4.2)$$

where P_f is the forward power at the position z ,

$$P_f = \int_S (\hat{E}_f^* \times \hat{H}_f) \cdot \hat{n} dS \quad (4.3)$$

and

$$\psi = \left| \frac{(E_f + E_r)}{E_f} \right| \quad (4.4)$$

which gives the field concentration due to reflections. ξ^2 is related to fields and power as in Chapter 3. The wave impedance is

$$\eta = E_f/H_f = \frac{\mu_0/\epsilon_0}{\sqrt{1 - (\omega_c/\omega)^2}} \text{ or } \mu_0/\epsilon_0 \sqrt{1 - (\omega_c/\omega)^2} \quad (4.5)$$

for TE and TM modes respectively, assuming that very little power is carried in the web. The complex dielectric constant of the water in the web is

$$\epsilon = \epsilon_0 (\epsilon'_W - j\omega\epsilon''_W)$$

and ρ is the volume fraction of the web which is filled with water.

The ϵ''_r of the web as a whole is $\rho\epsilon''_W$. * ω_c is the radian cutoff frequency and ω is that of the power source.

(b) Drying Rate

When the web surface is kept soaked by capillary action the mass lost through drying is given by the empirical relation

$$\frac{\partial m}{\partial t} = -K_G(R)^U(S)^V (P_a/p_{fm}) P_W B \quad (4.6)$$

*In this analysis it is assumed that the power absorption is caused only by free water in the web. Thus $F\rho$ is the cross-sectional area occupied by water with dielectric constant $\epsilon_0\epsilon'_W - j\epsilon_0\epsilon''_W$. Alternatively F is the filling factor of the web and its dielectric constant is $\epsilon_0(\epsilon'_r - j\epsilon''_r)$. The latter interpretation may permit easier understanding of the problem at low moisture content, where ϵ''_r is higher than predicted by this model, since ϵ''_W is not constant (62).

where m is the mass of water per unit length, K_G is the mass transfer coefficient, R is the modified Reynolds number, S is the Schmitt number, B is the boundary exposed to air, u and v are experimentally determined constants, p_a is the total pressure of air in the (dry) air stream, p_w is the partial pressure of water at the web boundary and p_{fm} is the logarithmic mean partial pressure of dry air in the boundary layer⁽¹⁾. The variable p_{fm} is given by

$$p_{fm} = \frac{(p_{fs} - p_{ft})}{\ln (p_{fs}/p_{ft})} \quad (4.7)$$

where p_{fs} is the partial pressure of dry air at the surface. p_{ft} is the partial pressure of dry air at the upper edge of the boundary layer.⁽¹⁾ Simplifying and combining drying parameters,

$$\frac{\partial \rho}{\partial t} = \frac{-k_{dry} B}{\Delta S g_w} \frac{p_a}{p_{fm}} p_w \quad (4.8)$$

where $k_{dry} = K_G (R)^u (S)^v$, which varies with air duct design and flow rate, g_w is the density of water (kg/m^3), ΔS is the cross-sectional area and $B/\Delta S$ is the surface to volume ratio of the web.

(c) Temperature Changes

The rate of temperature rise is given by

$$\frac{\partial \theta}{\partial t} = \frac{1}{\rho \Delta S g_w c_w} \frac{\partial Q}{\partial t} = \frac{1}{\rho \Delta S g_w c_w} (P_{web} + \lambda_w g_w \Delta S \frac{\partial \rho}{\partial t}) \quad (4.9)$$

where θ is the average temperature ($^{\circ}\text{C}$), c_w is the specific heat of water (Joules/ $^{\circ}\text{C}$ kg), Q is the heat in the web (Joules/m), λ_w is the latent heat of evaporation (Joules/kg), where MKS units have been

used for consistency with the electromagnetic units. It is assumed that no heat is lost to radiation and that none is supplied by the air stream. k_{dry} is nearly independent of temperature⁽¹⁾.

Let the equilibrium temperature be θ_e . If θ is below θ_e , $\partial\rho/\partial t$ is low and ρ changes slowly while θ rises. If P_{web} is constant and $\Delta\theta = (\theta - \theta_e) \ll \theta_e$, a change in $\partial\rho/\partial t$ will occur, i.e.,

$$\rho\Delta\theta c_w = \lambda \int_0^\infty \left\{ \left\{ \frac{\partial\rho}{\partial t} \right\} - \left\{ \frac{\partial\rho}{\partial t} \right\}_e \right\} dt. \quad (4.10)$$

Differentiating with respect to time,

$$\frac{\partial\theta}{\partial t} = \frac{\lambda_w}{c_w} \frac{1}{\rho} \left(\frac{\partial\rho}{\partial t} - \left(\frac{\partial\rho}{\partial t} \right)_e \right) \quad (4.11)$$

Thus the time constant of temperature equilibration is 539.5 times less than that of drying of the web. It can therefore be assumed that the web is very close to thermal equilibrium while it dries.

The vapor pressure of water and ϵ_w'' are known functions of temperature^{(26),(57),(68),(71)}. Since the surface is assumed to be wet, p_w is the vapor pressure, and from a curve fitting program,

$$p_w \doteq 2.0805 \times 10^{-8} \theta^5 + 2.097 \times 10^{-6} \theta^4 + 1.942 \times 10^{-4} \theta^3 + 0.011084 \theta^2 + 0.32593 \theta + 4.6249. \quad (4.12)$$

For the dielectric losses, at the 2450 MHz ISM frequency,

$$\epsilon_w'' \doteq 3.6949 \times 10^{-7} \theta^4 + 0.0001084 \theta^3 + 0.01222 \theta^2 - 0.70285 \theta + 21.331. \quad (4.13)$$

The dimensions are, of course kept correct by the numerical constants.

(d) Normalized Drying Rate

Substituting $\partial\theta/\partial t \approx 0$ and using Equations 4.2, 4.8 and 4.9,

$$\epsilon_0 \rho \epsilon_w'' \omega \psi^2 \xi^2 \ln P_f F = \lambda_w k_{dry} B (P_a/p_{fm}) p_w \quad (4.14)$$

If the web has a thickness t' and two sides are exposed to air,

$$B/\Delta S = 2/t' \quad (4.15)$$

and we may define

$$x_e = (u_p \epsilon_w''(\theta_e)) / \left(\frac{p_a}{p_{fm}(\theta_e)} \right) p_w(\theta_e) \quad (4.16)$$

where

$$u_p = 1 \text{ Torr} \quad (4.17)$$

which keeps the dimensions correct. Then solving Equation 4.14,

$$x_e = \frac{2 u_p k_{dry} \Delta S \lambda_w}{t' \epsilon_0 \eta \omega P_f \psi^2 \rho \xi^2} \quad (4.18)$$

The variable x_e is dimensionless and depends only on θ_e . Solving for x_e at $p_{fs} = (760 - p_w)$ and $p_{fa} = 760$ Torr, and changing dependent to independent variable with the curve fitting computer program,

$$\theta_e = -0.01800261 x^4 - 0.08522502 x^3 + 4.938560 x^2 - 10.37308 x + 15.19636 \quad (4.19)$$

where

$$x = \ln(x_0 / \rho \xi^2 \psi^2 (P_f/P_0)) \quad (4.20)$$

and where

$$x_0 = x_e(\theta_0). \quad (4.21)$$

This gives two new variables, P_0 , a reference power, and θ_0 , the reference equilibrium temperature at this power for $\rho = \psi^2 = 1$.

The other independent variable is k_{dry} , which can be adjusted by changing the air flow. While it does not appear in the following analysis, it will be assumed that the air flow gives an equilibrium temperature θ_0 at the forward power P_0 . From Eq. 4.14, at equilibrium,

$$\frac{\partial \rho}{\partial t} = \frac{-\epsilon_0 \rho \epsilon_W'' \omega \psi^2 \xi^2 \eta P_f F}{\lambda_W g_W \Delta S} \quad (4.22)$$

Let

$$\tau = \frac{t}{T_0} \quad (4.23)$$

where

$$T_0 = \lambda_W g_W \Delta S / \epsilon_0 \eta P_0 \omega \epsilon_W''(\theta_0) \xi^2 F \quad (4.24)$$

Then

$$\left(\frac{1}{\rho}\right) \left(\frac{\partial \rho}{\partial \tau}\right) = -\psi^2 \frac{P_f}{P_0} \frac{\epsilon_W''(\theta_e)}{\epsilon_W''(\theta_0)} \quad (4.25)$$

T_0 represents the boil-dry time constant at $\left(\frac{\theta_e}{\theta_0}\right) = \psi^2 = \frac{P_f}{P_0} = 1$.*

Returning to the temperature rise equation, 4.9, we can normalize it also:

$$\frac{\partial \theta}{\partial \tau} = \tau_\theta \left[\frac{P_f}{P_0} + \frac{\epsilon_W''(\theta_0)}{\psi^2 \epsilon_W'' \rho} \frac{\partial \rho}{\partial \tau} \right] \quad (4.26)$$

where

$$\tau_\theta = \left(\frac{\lambda_W}{C_W}\right) \psi^2 \frac{\epsilon_W''}{\epsilon_W''(\theta_0)} \quad (4.27)$$

This can be used for the transient problem, if needed, and again shows that change in θ is much more rapid than change in ρ .

* The substrate is assumed to be lossless.

(e) Propagation Constant

Altman⁽²⁾ gives a perturbation solution for the propagation constant. Assume that all the web in a cross-section is at the same temperature and moisture content (batch processing). Then for a single forward or reverse component E_r or E_f , the components of the propagation constant are

$$\beta - \beta_0 = \frac{\epsilon_0 (\epsilon'_W - 1) \omega \rho \iint_{\Delta S} (\hat{E}_0^* \cdot \hat{E}) dS}{2 \iint_S (\hat{E}_0^* \times \hat{H}) \cdot \hat{n} dS} \quad (4.28)$$

and

$$\alpha = \frac{\epsilon_0 \epsilon''_W \omega \rho \iint_{\Delta S} (\hat{E}_0^* \cdot \hat{E}) dS}{2 \iint_S (\hat{E}_0^* \times \hat{H}) \cdot \hat{n} dS} \quad (4.29)$$

where \hat{n} is a unit normal vector. \hat{E}_0 is the unperturbed electric field while \hat{E} is the perturbed field. For lightly loaded LSE modes \hat{E}_0 is approximately equal to \hat{E} . Also, $\hat{E} = \eta \hat{H} \times \hat{n}$ and $\beta_0 = \omega / v_p = \sqrt{\epsilon_0 \mu_0} / \sqrt{1 - (\omega_c / \omega)^2}$. The propagation constant is then

$$\gamma = \alpha + j\beta = \epsilon_0 \epsilon''_W \eta \omega \frac{F}{2} \epsilon^2 \rho \psi^2 + j \left(\frac{\omega}{v_p} + \epsilon_0 (\epsilon'_W - 1) \eta \omega \frac{F}{2} \epsilon^2 \rho \psi^2 \right) \quad (4.30)$$

where v_p is the phase velocity in the waveguide.

(f) Capacitance and Characteristic Impedance

The capacitance of a transmission line can be evaluated by using energy storage, or⁽³⁰⁾

$$\frac{2C}{v} = \frac{N_e}{v^2} = \frac{\epsilon}{v^2} \iint_S (\nabla \phi \cdot \nabla \phi) dS \quad (4.31)$$

where v is the total voltage between conductors, N_e is the stored

electric energy per unit length and \underline{C} is the capacitance per unit length. For a perturbed TEM line

$$\begin{aligned} \frac{\Delta \underline{C}}{\underline{C}_0} &= \frac{\underline{C} - \underline{C}_0}{\underline{C}_0} = (\epsilon'_W - 1) \rho \frac{\iint_{\Delta S} (\hat{E}^* \cdot \hat{E}) dS}{\iint_S (\hat{E}_0^* \cdot \hat{E}_0) dS} \\ &= (\epsilon'_W - 1) \xi^2 F_\rho \end{aligned} \quad (4.32)$$

This can be used to calculate the characteristic impedance change,

$$\underline{Z}_0 = \sqrt{\underline{L}_0 / \underline{C}_0} \quad \text{and} \quad \underline{Z}'_0 = \sqrt{\underline{L}_0 / (\underline{C}_0 + \Delta \underline{C})} \quad (4.33)$$

In complex form the normalized characteristic impedance is

$$\underline{Z} = \frac{\underline{Z}'}{\underline{Z}_0} = \sqrt{1 / 1 + F \xi^2 \rho \{ \epsilon'_W - 1 - j \epsilon''_W \}} \quad (4.34)$$

(g) Distributed Reflections

It can be shown⁽¹⁴⁾ that a TEM line or waveguide with a characteristic impedance discontinuity and a load mismatch (Fig. 4.1) gives a voltage reflection coefficient

$$\Gamma = \frac{\Gamma_1 + \Gamma_3 \exp(-2\gamma \ell)}{\Gamma_1 \Gamma_3 \exp(-2\gamma \ell)} \approx \Gamma_1 + \Gamma_3 \exp(-2\gamma \ell) \quad (4.35)$$

For a transmission line with gradually changing \underline{Z}_0 , we may assume step increments at the ends of infinitesimal lengths dz , or

$$d\Gamma = \frac{1}{2} d \ln \underline{Z}_0 \quad (4.36)$$

or at the input of the line or waveguide,

$$\Gamma_i = \frac{1}{2} \int_0^L \exp(-2\gamma z) \left(\frac{\partial}{\partial z} \ln Z_0 \right) dz \quad (4.37)$$

Using Z , Eq. 4.37 may be approximated by two finite difference equations in E_r and E_f .

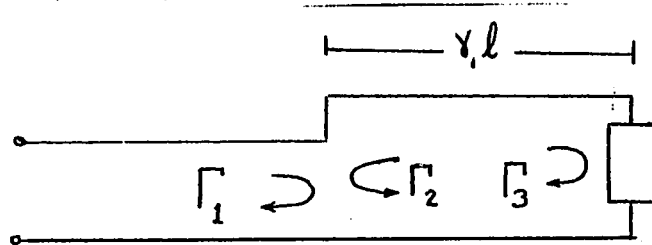


Figure 4.1 Double Discontinuity

(h) Finite Difference Equations for Reflections

Assume that the applicator is matched except for the effect of the web, ie once the power passes the load it is absorbed. The web may be divided into N segments, h units in length, in the propagation direction, and numbering will begin at the end opposite to the power source.

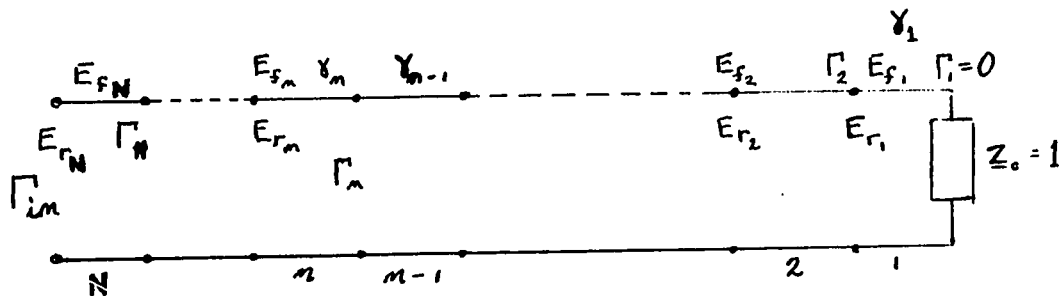


Figure 4.2 Distributed Reflections

At each segment, assume the reflection to occur at the load end and measure E_f and E_r at the beginning. Using Eq. 4.34,

$$\Gamma_i = (\underline{Z}_{i-1} - \underline{Z}_i) / (\underline{Z}_{i-1} + \underline{Z}_i) \quad (4.38)$$

Starting at $n = 1$ we assign E_{f_1} some value temporarily and calculate all the E_{f_n} and E_{r_n} by recursion. (Finally, all values can be reset to correspond to the actual input power.) Then

$$E_{r_1} = E_{f_1} \Gamma_1 \exp(-2\gamma_1 h) \quad (4.39)$$

For any element n , from $n = 1$ to $n = N-2$.

$$E_{f_{n+1}} = \frac{E_{f_n} \exp(\gamma_n h)}{(1 + \Gamma_n)} - E_{r_n} \Gamma_{n+2} \quad (4.40)$$

and

$$E_{r_{n+1}} = E_{f_{n+1}} \Gamma_{n+1} \exp(-2\gamma_n h) + E_{r_n} (1 - \Gamma_{n+2}) \exp(-\gamma_n h) \quad (4.41)$$

For the last element, Equations 4.40 and 4.41 give the correct results if $n+1 = N$ and $\Gamma_{n+2} = 0$. N , of course gives the web width, z_m , i.e. $N = z_m/h$, to the nearest integer. Then

$$\psi_n^2 = \left(\frac{E_{f_{n+1}} + E_{r_{n+1}}}{E_{f_n}} \right)^* \cdot \left(\frac{E_{f_{n+1}} + E_{r_{n+1}}}{E_{f_n}} \right) \quad (4.42)$$

(i) Finite Difference Time Response of the System

Eq. 4.25 can now be converted to a finite difference equation by setting $E_{f_N}^* \cdot E_{f_N} = 1$ for normalization of power. A small interval of normalized time τ can be chosen. Then

$$\frac{(\rho_{k+1} - \rho_k)_n}{\Delta\tau} = -\rho_{k,n} \frac{\epsilon_w''}{\epsilon_w''(\theta_0)} \psi^2_{k,n} \quad (4.43)$$

where the subscript k refers to the time index and n refers to the z index.

At $k = 0$, θ_0 , and some desired ρ_0 are assigned as initial conditions. The web-applicator-magnetron system design is described by the constants ϵ_n^2 , F , ρ_0 , z_m , ω_c , ω , P_0 and the air flow. The web reaches an initial equilibrium temperature of θ_0 at $n = N$, or where the power is first incident. The air flow and P_0 are assumed to be correctly related to give θ_0 . Then the edge nearest to the magnetron will dry at a rate such that $(\rho_{0N} + (\frac{\partial \rho}{\partial \tau})_{0N} T_0) = 0$ where the subscripts 0 and N indicate initial conditions at the edge.

The air flow is assumed to be uniform and initially dry, the web to be thin enough that it is at nearly the same temperature throughout, which gives the vapor pressure of the surface water, and k_{dry} is assumed to be nearly constant. Only the range above fibre saturation is treated and diffusion of liquid water from location to location is ignored. Perturbation analysis of waveguide behavior has been used with LSE modes.

4.3 Exponential Heating Model and Meanderline Applicators

There are important cases where evaporation is minimal or irrelevant. Then Eq. 4.9 reduces to

$$\frac{\partial \theta}{\partial t} = \frac{1}{\Delta S g_d c_d} P_{web} \quad (4.44)$$

where g_d and c_d are the mass density and specific heat of the web.

Expanding P_{web} ,

$$\frac{\partial \theta}{\partial t} = \frac{\epsilon_0 \epsilon_r''(\theta)}{\Delta S g_d c_d} \omega \xi^2 F \psi^2 P_f \quad (4.45)$$

In this section $\epsilon_0 \epsilon_r''(\theta)$ is that of the web as a whole, and must be obtained from sources such as Tinga⁽⁶¹⁾. Integrating Eq. 4.45,

$$\theta(t) = \frac{\epsilon_0 \omega \xi^2 F \psi^2}{\Delta S g_d c_d} \int_{t_0}^t P_f \epsilon_r''(\theta(t)) dt \quad (4.46)$$

Should ϵ_r'' be nearly constant,

$$\theta(t) = \frac{\epsilon_0 \epsilon_r'' \omega (\xi^2 \psi^2 F)}{m_d c_d} P_f (t - t_0) \quad (4.47)$$

where m_d is the mass in the applicator per meter.

The wave is attenuated in propagating along the applicator according to Eq. 4.32. Assume $\psi^2 = 1$; i.e. there are no reflections. Then, as in Chapter 1,

$$\begin{aligned} P_f &= P_0 \exp(-2\alpha z) \\ &= P_0 \exp(-\epsilon_0 \epsilon_r'' \eta \omega (F \xi^2 \psi^2)) z \end{aligned} \quad (4.48)$$

where P_0 is the power produced by the magnetron. The temperature profile as a function of time and distance is

$$\theta(t, z) = \frac{P_0 G(t)}{m_d c_d} \{t - t_0\} \exp\{G(t) \eta z\} \quad (4.49)$$

where $G(t) = \epsilon_0 \epsilon_r''(t) \omega F \xi^2$. (4.50)

The variable G is the conductance per unit length and is the conductance of the web multiplied by $F \xi^2$. $G \eta$ is the ratio between power absorbed per unit length and the transmitted power for the system under consideration.

When many passes are made, for a web z_m meters wide and for a residence time t , at location z on pass k ,

$$\theta(t,z) = \frac{P_0 G_k (t-t_0)}{m_d c_d} \{ \exp[-G_1 \eta z] + \exp[-(2z_m - z)G_2 \eta] \\ + \exp[-(2z_m + z)G_3 \eta] + \exp[-(4z_m - z)G_4 \eta] + \dots \} \quad (4.51)$$

The temperature inhomogeneity is less than that caused by a single pass, which is also true for moisture content inhomogeneities. If the series G_k (G_1, G_2 etc.) is gradually increasing, the range of loads which may be heated uniformly is increased.

In a Taylor series expansion for θ the first order term may be cancelled. When all the G 's are equal this can be accomplished by using an even number of passes⁽⁷³⁾, and the decrease in inhomogeneity is dramatic if the total inhomogeneity per pass is small. For instance, 20% inhomogeneity can be reduced to 5%, 30% to 10%, and 40% to 26%. For such an applicator, the designer should check for excessive reflection by using Eq. 4.34, check for excessive inhomogeneity by using Eq. 4.49 or the drying profile of Section 4.2, and if these do not exceed about 30%, add a final pass whose attenuation is sufficient to cancel the linear term of a Taylor expansion of Eq. 4.51. Alternatively he may use an even number of passes at each attenuation rate. If the inhomogeneity is excessive for any pass, it may be reduced by reducing the product of F and ξ^2 for the particular applicator chosen.

Figure 4.3 shows the percentage temperature inhomogeneity (lower three curves) and the percentage efficiency (upper three curves) for three applicators. The inhomogeneity is given by

$$I_{\alpha} = 100 (\theta_{\max} - \theta_{\min}) / \theta_{\max} \quad (4.52)$$

and is plotted on a log scale. The abscissa is $G_n z$, also on a log scale. Numbering from the top, curve number 3 gives both efficiency and inhomogeneity for applicator A_1 , a single pass of waveguide, TEM or any other mode. The user is given the choice of bad inhomogeneity or bad efficiency which is not surprising. Curve 1 is the efficiency and curve 4 the inhomogeneity for applicator A_2 consisting of five passes of the same waveguide as in curve 3. This applicator gives improved uniformity since it returns the wave to the far side of the web, and improved efficiency due to the increased number of passes over the web. Curve 2 gives the efficiency and curve 5 the inhomogeneity for the graded attenuation applicator, A_3 , designed in Chapter 3. The abscissa is $G_5 n z$, where G_1, G_2, G_3, G_4 , and G_5 are increasing in the order of $1/16, 1/8, 1/4, 1/2$, and 1 . There is some loss in efficiency because of the low attenuation on some passes, but there is a more than proportional improvement in homogeneity. The final pass to cancel the first-order Taylor series term has been omitted. It would produce better cancellation in the graded applicator A_3 than in the constant attenuation applicator A_2 .

4.4. Experimental Results

A length of WR284 waveguide (1.34" by 2.84" inside dimensions) was constructed with $\frac{1}{8}$ " wide slots in the broad walls and tapering at

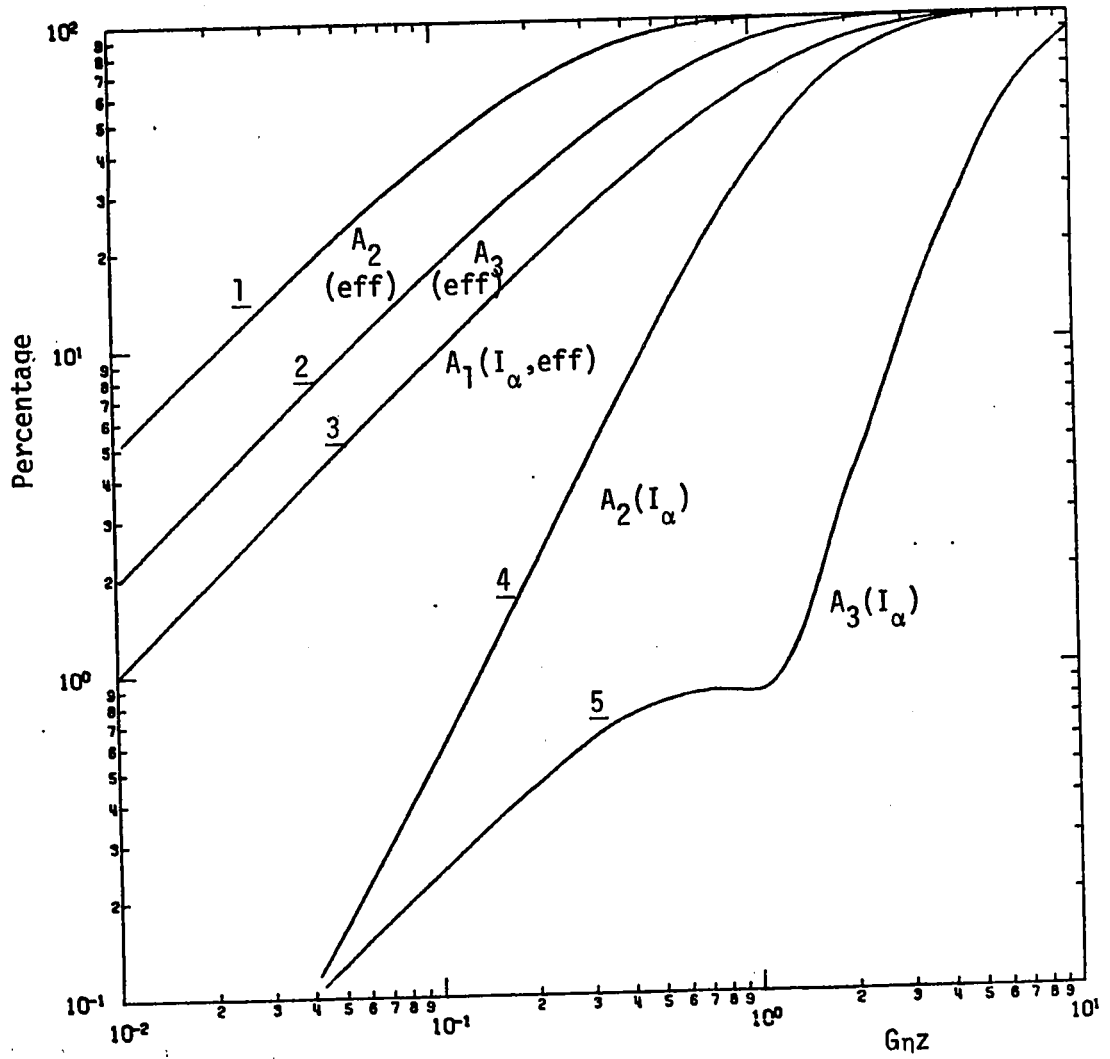


Fig. 4.3 INHOMOGENEITY AND EFFICIENCY VS WEB LOADING

the ends, with a useable length of 45 cm. A water load, matched to provide less than -20dB return loss, and a Philips DX260 1 kW 2450 MHz magnetron were connected to either end of this TE_{10} applicator. An air duct was provided with an opening into one slot $\frac{1}{8}$ " high by 18" long. Five vanes were mounted internally to redirect an air stream incident on the $1\frac{1}{2}$ " by $1\frac{1}{2}$ " end evenly over the web. This was checked with a simple flowmeter. The web was placed on a 0.01" mylar strip to expose only one side to the air stream. A Fortran IV program* was used to predict the attenuation and temperature profiles given the initial temperature, which was measured after 5 seconds ($\tau=0.2$).

Three strips of blotting paper were soaked to 185% water content (dry basis) and placed on the mylar strip. One kW of power was applied giving an initial temperature of 45°C where the power was first incident on the load. The experimental reflection coefficient, measured at low power, was 3.2 ± 0.2 dB, or 45% reflected power. The program predicted 5 dB, or 32%. This is probably due to higher order modes being generated in the vicinity of the interface, since the load was a large perturbation. The predicted T_0 was 17.8 sec at 1 kW and the observed value was between $18\frac{1}{2}$ to $21\frac{1}{2}$ seconds. In Table 4.1 the weights of samples from the partially dry web are compared to the theoretical values. These results check very well. Due to the drying rate and the available balance used, the webs were heavy and measurement times in the vicinity of $\tau = 0.75$ were used. The moisture content is expressed as the percentage of the moisture content measured in an identically prepared control sample. This is of the same form as the output of the program, which assumed that the web started at $\rho = 100\%$.

* See the following section.

Table 4.1 Experimental Check on Attenuation Inhomogeneity

Time	Temperature*	Location	Moisture Content		τ	
			Experimental	Theoretical		
15 sec	35.0 ⁰	2 cm	42±5%	39.3%	0.8	
		9 cm	86%	91.9%		
		18 cm	97%	100%		
15 sec	35.6 ⁰	7 cm	45%	44.8%	0.7	
		25 ⁰	5 cm	73%		76.1%
		9.9 ⁰	9 cm	84%		93.2%
		5 ⁰	14 cm	97%		99.9%
		5 ⁰	30 cm	94%		100%
		5 ⁰	39 cm	104%		100%

* Measured temperature was 35⁰ at $\tau = 0$.

4.5 Computer Results for Very Wet Webs

Fortran IV programs were written to solve the system of difference equations, developed in Section 4.2, for TEM and WR284 applicators. The input variables were $\epsilon_w''(\theta_0)$, x_0 , F , the number of wavelengths of web, the time and distance intervals, and printing instructions. The output for each time interval was maximum reflection coefficient and, at several locations, the temperature, water remaining, and deviation from an exponential which was fitted to the curve of moisture content.

Figure 4.4 shows the moisture content curves for one wavelength of wet web at several instants in normalized time. $F\xi^2$ was 0.03416, giving $F\xi^2\epsilon_w'' = 0.1$ at 80⁰C. τ , starting at the top, is 0.25, 0.5, 0.75, 1, 1.25, 1.5, 1.75 and 2.0 for the solid curves representing 80⁰C. The x's are for $\tau = 1.0$ at 35⁰C. The frequency was 2450 MHz and the applicator was a TEM structure. Waveguides give more attenuation in the TE modes.

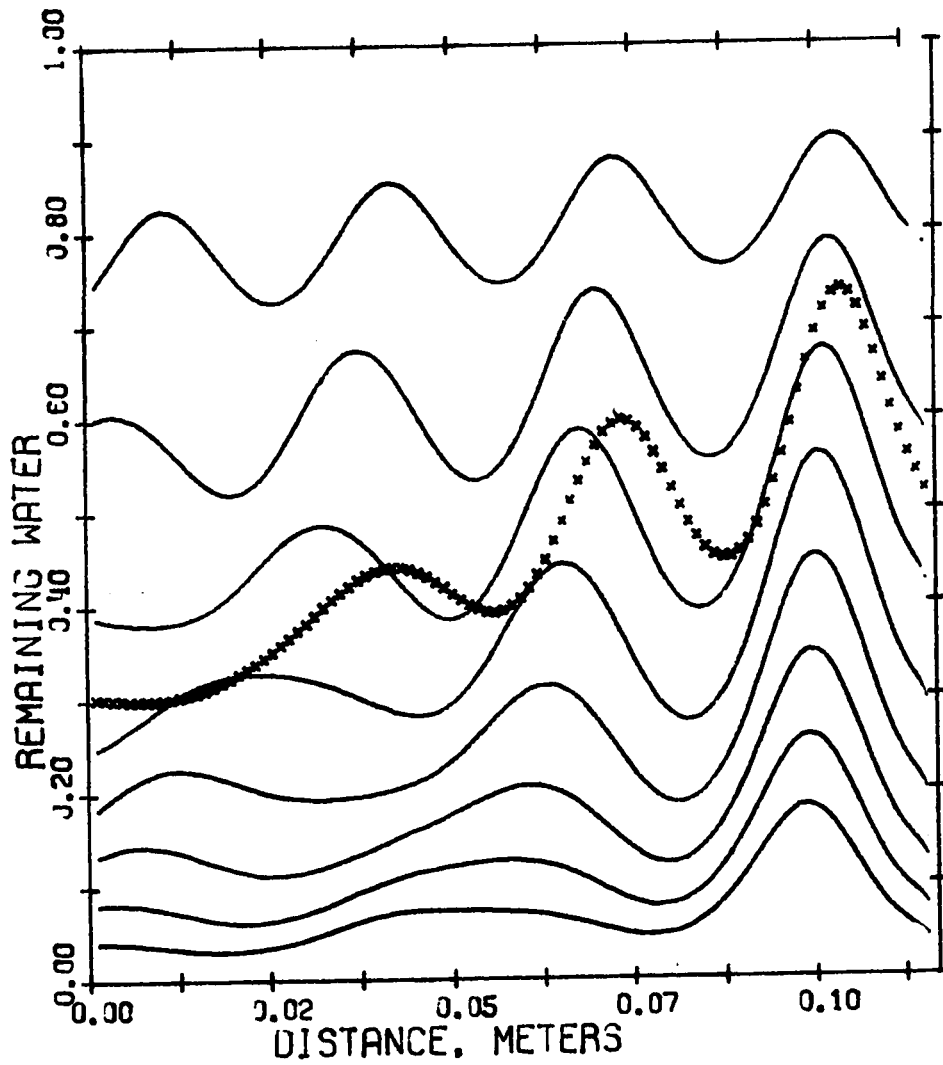


Fig 4.4 Moisture Content at Time 0.25, 0.5, 0.75, 1.0, etc.

The moisture content starts at 1.00 throughout the web and evaporates. Plots are shown at the instants indicated, and the hot spots are lower in moisture content. The wet spot at 1 meter has been shielded by reflections and appears in all plots.

One rather bad wet spot remains at the far edge. Since a wet spot is a region of low electric field, it is shielded by reflections. The fact that the guide wavelength increases as the water evaporates prevents standing waves from increasing the shielding effect as evaporation progresses. The maxima move, drying the wet spots previously left by minima. This effect would not be present in moving webs.

Other results for webs wider than 1 wavelength show that at 2450 MHz, inhomogeneity is introduced mainly by attenuation. This shows that at least in the 2450 MHz ISM (Industrial, Scientific and Medical) band, problems with standing waves are likely to originate in the design of the unloaded applicator, not in the reflections from web discontinuities, as had been suspected. The reflection for the edge of the web in Figure 4.4 is only -11.6 dB, which is not difficult to create by designing a bend in a waveguide. -11.6 dB is not a severe reflection, but its effect is quite substantial due to the fact that the VSWR is twice the magnitude of the reflected electric field and the power absorbed is proportional to the square of the sum of the reflected and incident fields⁽⁷³⁾. The upper gap controls the characteristic impedance in the TEM applicator, which should help reduce reflections.

The least-squares fit of an exponential through the moisture content curve of the web showed that the heating can deviate markedly from an exponential due to high temperature depression of ϵ_w'' . As a result, the drying is more uniform than the heating predicted (Section 4.3). If the air flow is increased to keep θ_0 low, levelling is improved, but an uneven electric field will then create more inhomogeneity.

In Figure 4.5 some results are shown for inhomogeneity vs. normalized time. The curves are: curve 1, $F_{\xi^2 \epsilon_w''}(\theta) = 0.03416$ or $F_{\xi^2 \epsilon_w''}(\theta_0) = 0.1$; curve 4, with x 's $F_{\xi^2} = 0.01113$ or $F_{\xi^2 \epsilon_w''}(\theta_0) = 0.03333$, where the waveguide version of the program was used; curve 2, also $F_{\xi^2} = 0.01113$ etc. but for TEM waveguide; curve 3, $F_{\xi^2} = 0.003416$ or $F_{\xi^2 \epsilon_w''}(\theta_0) = 0.01$. In curves 1, 3 and 4 a TEM version of the program was used and in curve 2, the waveguide version for WR284 guide at 2450 MHz was used. The initial temperature was 80°C , and 3.33 free-space wavelengths of web were assumed. The ordinate is the difference between the wettest and driest spot in the web, referred to the original moisture content, or

$$I = \left(\frac{\rho_{\max} - \rho_{\min}}{1.0} \right) \times 100\% \quad (4.53)$$

where ρ was initially 1.0.

To use this chart for conditions not exactly as programmed, we note that in all but very short webs it was found that the slow-wave effect smoothed out the wet spots. When wider webs, in this case 10 free space wavelengths, were assumed the inhomogeneity was proportional to the web width. When different temperatures were assumed, the inhomogeneity was proportional to $\epsilon_w''(\theta_0)$. Due to the higher n of the TE_{10} waveguide, attenuation is approximately doubled for this particular guide at this frequency. Inhomogeneity is proportional to n/n_0 . Then for curves 1, 2 and 3, the factor $F_{\xi^2 \epsilon_w'' z_m}$ is 0.333, 0.1, and 0.0333 respectively. The wet spot is not the same magnitude because the reflection coefficient is lower for wider lighter webs and some deviation will occur from scaling to narrow webs. We may even change the frequency, remembering that reflections may be

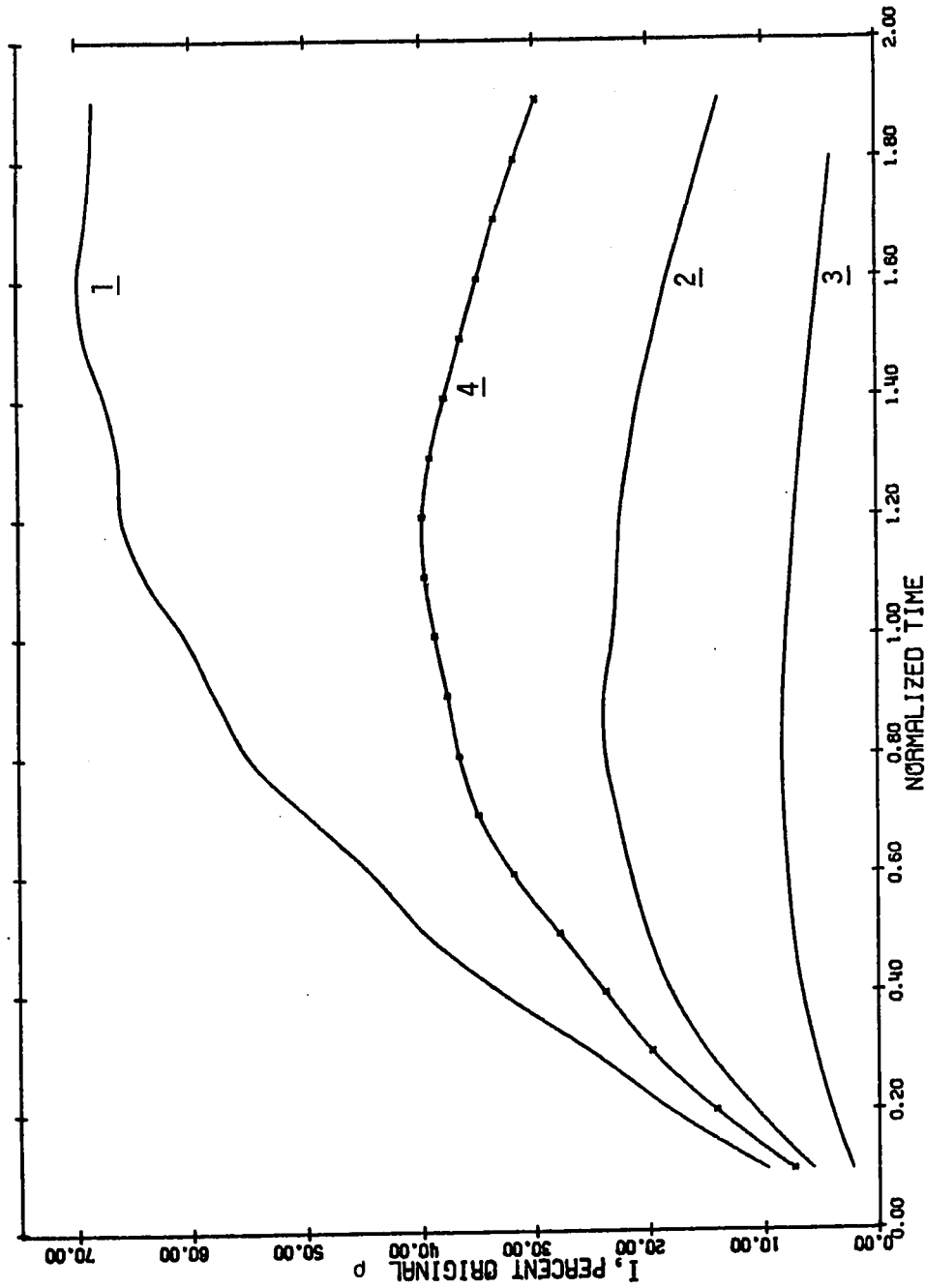


Fig. 4.5 DIFFERENCE BETWEEN MIN AND MAX MOISTURE CONTENT

much worse in the 915 MHz ISM band, where ϵ_w'' is lower. The TEM plots represent $G = 2.1, 0.70,$ and 0.21 respectively. For curve 3 of Figure 4.3 the respective temperature inhomogeneities for the other model would be 85%, 40% and 17%. Thus there is considerable gain in homogeneity from evaporation and the depression of ϵ_w'' at high temperature. However, the latter effect tends to work against levelling of moisture.

Figure 4.5 differs from Figure 4.3 in that the web will eventually dry and the power is assumed to go to the water load when it does. The unused power goes on to dry the remaining wet areas in this batch processing scheme. Batch processing is not often used in practice, but this assumption gives a conservative design plot. The average inhomogeneity in one pass will be slightly better for a moving web, since it will be partly wet and partly dried, i.e. different parts of the web represent different instants in normalized time. Therefore a bound for I in a moving web may be obtained by finding the appropriate curve in Figure 5.4 and adding a term I_T . The latter term is needed because in moving webs the standing wave nulls remain stationary after equilibrium is established. The extra term is given by

$$I_T = 4|\Gamma| \quad (4.54)$$

where Γ is calculated from $\rho = 1$ and $\rho = 0$ in Eq. 4.38.

If the air flow is increased, the initial equilibrium temperature is reduced. This means that the effect of high temperature depression of ϵ_w'' is less, and I is increased. The effect of mass transfer still exists, though, and a graph such as Figure 4.5

for the new temperature would be needed. An even more conservative bound could be obtained by using the I_α in Figure 4.3, which does not allow for evaporation.

In moving web systems one cannot always rely on eventual drying of heavy webs. Should the material be susceptible to thermal runaway, it is very undesirable that one part of the web be much drier than the rest. If the graduated multiple pass applicator is used, the web is forced to accept power by the very high ξ^2 in the last pass. If the power is too high and the material is susceptible to thermal runaway, fires may result. The web must not stop and it may be desirable to use limited attenuation. Increasing the air flow rate gives lower temperatures and may keep the web in a range where there is no danger of thermal runaway. This does not effect the drying time, except for an increase ϵ_w'' for the free water in the web. It is desirable that ξ^2 be kept low, however, so that these effects do not occur.

It is now possible to relate the evaporation analysis to Heenan's treatment⁽³⁵⁾. Several passes of waveguide form a slow wave structure. Let the distance measured along the wave path be z and that along the slow wave path be z' . The slow wave travels at a velocity which is reduced by z'_p/z_p , where z'_p and z_p are the periods of the path of the fast and slow wave respectively, in other words the total length of the waveguide per pass and the spacing between passes. The wave travels in the $+z$ and $+z'$ directions. These coordinates are at right angles to each other. Heenan refers to any web motion which is perpendicular to z as crosscurrent flow.

For the slow wave, the material and energy flows are concurrent if the web material moves in the $+z'$ direction and they are countercurrent if the web moves in the $-z'$ direction.

Assume that the predicted inhomogeneity for batch heating is less than 30% (or some other accuracy criterion). Then an even number of identical passes will give a uniform evaporation profile in z . If the web is moving this profile will vary across the waveguide in the z' direction. Heenan's treatments of concurrent and countercurrent flow are then approximately valid if z' is substituted for his z and all the attenuation factors are multiplied by z_p/z'_p . The applied power is a step function in z' and the moisture content is constant between passes and decreases across the waveguide portions of z' . The equations would predict an approximation to this profile, a continuous function equivalent to distributing the power uniformly over the entire web.

In summary, the evaporation analysis has resulted in inhomogeneity plots which differ by about a factor of 2 from the simple exponential. The observed hot spot formation at 2450 MHz has been traced to the applicator design, not loading, but at 915 MHz ϵ_r'' is significantly lower, and web reflections may be a much greater problem. The analysis can show whether this is so for any loading condition. It is not a complete description of drying below the fibre saturation point, where ϵ_w'' of water is not constant and the surface is not kept wet. It was shown that Figure 4.3 is a worst-case plot except in the range where $\partial \epsilon_r'' / \partial \theta$ is positive, and that the inhomogeneity of drying can be conservatively predicted by calculating that in the initial heating profile.

CHAPTER FIVE

CONTROL OF REFLECTIONS FROM RESONANT APPLICATORS

The problems associated with resonant applicators will be considered in this and the next chapter. In travelling wave applicators, the techniques which were used for reducing heating nonuniformity reduced reflections as well. In resonant applicators, however, the energy is reflected many times inside the cavity until it is dissipated. Conventional coupling techniques often permit some of the internally reflected waves to be coupled back out of the applicator. The resulting high VSWR shortens the life of the magnetron and is the most troublesome aspect of resonant applicator design. A coupling technique to reduce this difficulty will be treated, both theoretically and experimentally, in this chapter.

5.1 Microwave Heating in Resonant Cavities

When a load is relatively predictable, specialized applicators may be designed for it. However, experience has shown that for loads of various sizes and shapes multimode cavities often give the most satisfactory performance⁽⁷⁴⁾. In a well designed multimode cavity many resonant frequencies are available in the operating ISM band⁽³⁸⁾. The electric field nulls of these modes do not in general coincide, and heating will occur at almost any location if all the modes can be excited. Further, if a dielectric is placed in such a cavity, alternative modes are pulled downward into the frequency band of the magnetron, and the VSWR is better than for a single mode structure, which would simply be detuned.

The most common use of multimode cavities is in microwave ovens. Since these appliances are used by the general public, the system must be insensitive to moderate abuse⁽¹⁵⁾. Figure 5.1 shows a typical loop coupled microwave oven cavity, and alternate coupling structures are shown in Figure 5.2. The filling factor is usually less than 10%.

The loops and probes are usually less than $\lambda/2$ in size and do not extend over more than one field maximum. Therefore they are termed small element couplers here. The long strap coupler acts as a stripline transmission line with distributed electric and magnetic coupling. Because of its size it couples strongly to more modes than the small element couplers⁽⁷⁵⁾ and gives reduced VSWR. However, experiments show that the reflections are not reduced as much as might be expected and that stub matching in the transmission line is not uniformly effective over the entire band. For all the couplers shown reactive components of the input impedance vary widely with frequency; each change in load or operating frequency necessitates a change in the stub. This type of behavior can be traced to the fact that the cavity fields change sign nearly in synchronism with the reflections travelling in the coupler. Energy coupled from the cavity thus tends to add to the reflected wave rather than cancel it.

To avoid the synchronism between cavity and coupler waves, slow wave structures have been tested as coupling elements. The simplest slow wave structure, shown in Figure 5.3, is derived from the long strap coupler by zig-zagging it. If this structure is coupled

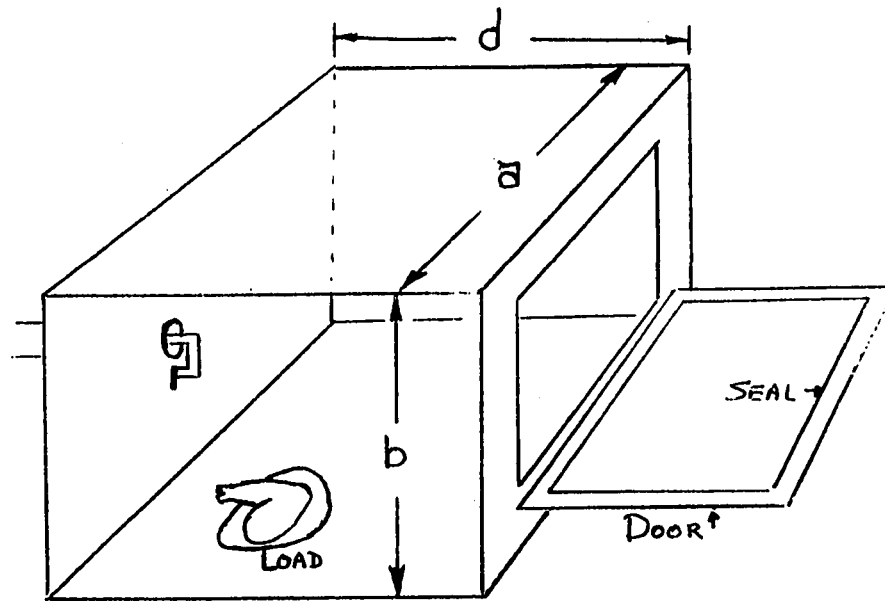


Figure 5.1 Microwave Oven Cavity

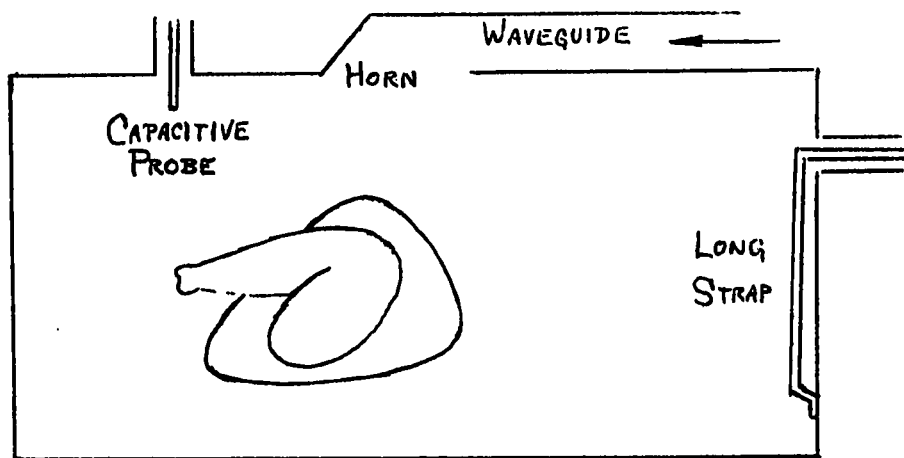


Figure 5.2 Various Coupling Elements

at the end, its characteristic impedance should be equal to that of the input transmission line, while if it is coupled at the centre, the characteristic impedance may be doubled. Experiments show that the slow wave structure gives improved VSWR, heating uniformity and matching between modes. The single stub tuner also provides an optimum match over the whole ISM band at one particular setting. This indicates that with this structure the residual reflections consist of the power that is not coupled into the cavity and is reflected from the ends of the coupling structure.

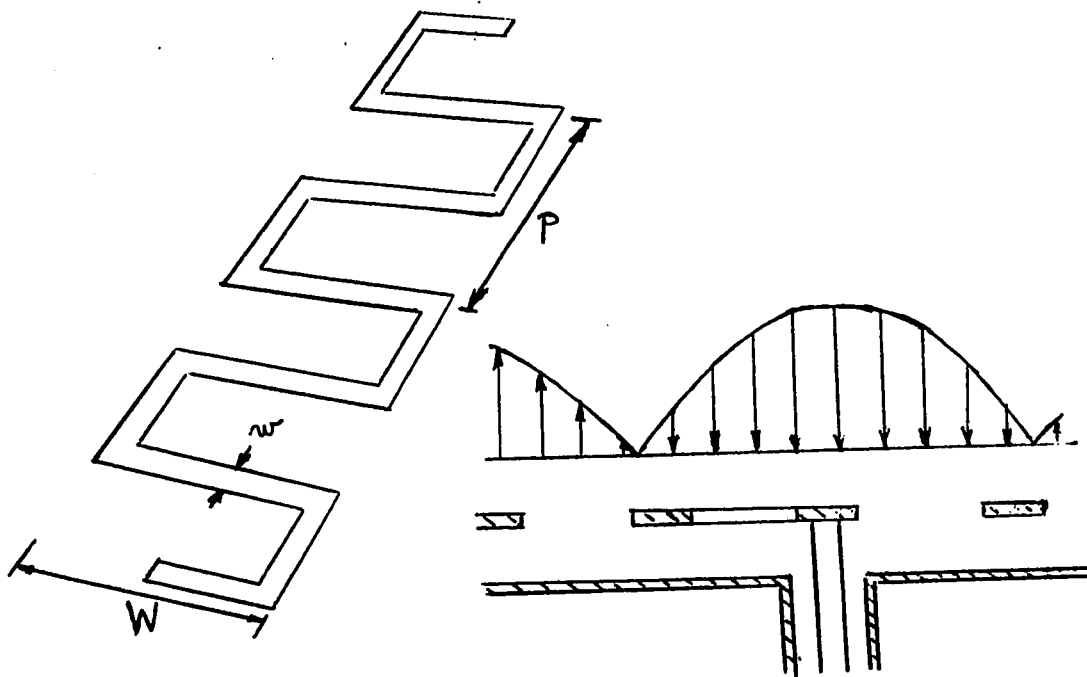


Figure 5.3

Stripline Slow-Wave Coupler

5.2 Reactance Coupling Theory

(a) Coupling Capacitance Model

The standard method for modelling and analyzing cavities employs a resonant circuit for each mode of the cavity⁽¹⁴⁾. A capacitor and inductor represent stored electric and magnetic energy respectively, while the losses in the walls and dielectric may be represented by a resistor in series with the capacitor. With a loop as the coupling element, mutual inductance for each mode may be calculated between the loop and the inductor of the model. For a coupling element which is small compared to a wavelength and couples with the electric fields in the cavity, we may use the capacitive coupling model of Figure 5.4. D is the capacitance between the cavity and the coupling element.

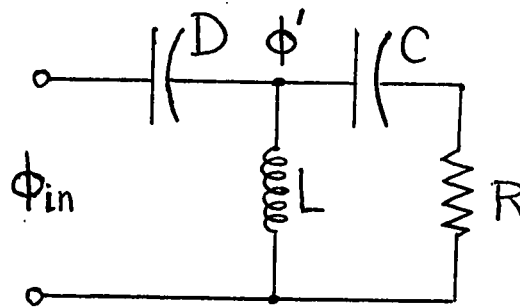


Figure 5.4 Lumped Circuit Model for a Single Mode

The resonant radian frequency of the mode n is given by

$$\omega_n = \sqrt{1/L_n(C_n + D_n)} \quad (5.1)$$

The energy stored in electric fields is given by:

$$N_e = \frac{\epsilon_0}{2} \int_V \epsilon_r' \hat{E} \cdot \hat{E}^* dV \quad (5.2)$$

Analogously, let the voltage on C be $\phi = \langle E \rangle / d$ where d is the distance between the wall with the coupling element and the opposite wall, as shown in Figure 5.1. $\langle E \rangle$ is a spatially averaged RMS electric field;

$$\langle E \rangle = \sqrt{\left(\frac{1}{abd}\right) \int_V (\hat{E} \cdot \hat{E}^*) dV} \quad (5.3)$$

where a , b , and d are shown in Figure 5.2. D is given by

$$D = \left(\frac{\langle E \rangle d}{\phi_c} - 1\right) / j\omega Z \quad (5.4)$$

Where Z is the impedance between the coupling element and ground, and ϕ_c is given by

$$\phi_c = \frac{\langle E \rangle d}{(1 + j\omega Z D)} \quad (5.5)$$

and represents the voltage induced in the coupling element by a standing field corresponding to ϕ' on C. Then $C + D$ is given by solving

$$N_e = \frac{1}{2}(C+D)\phi'^2 \quad (5.6)$$

The value of L may be determined from the resonant frequency and the value of C ; the latter calculated from the geometry of the cavity. Ignoring cavity losses other than dielectric heating the Q of the cavity in a particular mode is given by

$$Q_r = \frac{\int_V \epsilon_r' \hat{E} \cdot \hat{E}^* dV}{\int_{\Delta V} \epsilon_r'' \hat{E} \cdot \hat{E}^* dV} \quad (5.7)$$

where V is the cavity volume abd and ΔV is the volume of the load. P , the absorbed power is given by

$$P = \omega_n \epsilon_r'' \int_{\Delta V} \hat{E} \cdot \hat{E}^* dV \quad (5.8)$$

R may be obtained from the energy definition of Q:

$$Q_r = 2\omega_n N_e / P = 1/\omega_n (C+D)R \quad (5.9)$$

Losses other than the load are present, for example, the metal walls have a finite conductivity and may be deliberately coated with a lossy enamel for a base load. The wall losses should be represented by a resistor in series with L and the enamel load by a resistor in series with R and C. The Q of the model is given by

$$Q = \frac{1}{\frac{1}{Q_r} + \frac{1}{Q_e} + \frac{1}{Q_w}} \quad (5.10)$$

where Q_r , Q_e and Q_w are $\frac{2\omega_n N_e}{P}$ for the load, enamel (or other protective load) and the wall losses respectively. For high Q and $D \ll C$, the dielectric losses may also be represented by a resistance R_p in parallel with C given by,

$$R_p = \langle E \rangle^2 / d^2 P = Q\omega_n L \quad (5.11)$$

The results of the analysis for capacitive coupling are very similar to Collin's results⁽¹⁴⁾ for mutual inductance. Most applicators have both capacitive and mutual inductance coupling.

For multimode applicators, each mode should be represented by similar L,C,R equivalent circuits; the required number of these being equal to the number of significant modes.

(b) Results of Model

Solving for the input admittance of the model,

$$Y_{in} = \frac{sD(1+sRC+s^2LC)}{(1+sRC+s^2LC'+s^3LCDR)} \quad (5.12)$$

where $C' = C+D$. Rationalizing, the conductance is

$$G_{in} = \frac{-(\alpha^2\beta^2p^6)/Q^2R}{(1+p^2)^2-(p/Q)^2(1-p^4\beta^2\alpha^2)} \quad (5.13)$$

and the susceptance is

$$B_{in} = \frac{sD\{1+p^2(1+\beta-1/Q^2)+p^4(\beta-\alpha/Q^2)\}}{(1+p^2)^2-(p/Q)^2(1-p^4\beta^2\alpha^2)} \quad (5.14)$$

where $\omega_n^2 = 1/LC'$, $Q = 1/(\omega_n RC')$, $p = s/\omega_n$, $\alpha = D/(C+D)$ and $\beta = 1-\alpha$

s is the laplace transform variable and for steady state is equal to $j\omega$, which means that at resonance $p = j$. If $p = j$, $Q \gg 1$ and $\alpha \ll 1$; and letting $u_n = \omega/\omega_n$, we obtain

$$G_{in}(ju) = \frac{\alpha^2}{\{(1-u_n^2)^2+u_n^2/Q^2\} Q^2R} \quad (5.15)$$

and,

$$B_{in}(ju) = j\omega D + jG_{in}Q(u_n^2-1) \quad (5.16)$$

At resonance, these reduce to

$$Y_{in_n} = \frac{\alpha}{R} + j\omega D \quad (5.17)$$

Eq. 5.15 shows that if the voltage were kept constant (which is not the case for probes on transmission lines) the power absorbed is reduced by 3 dB at frequencies where $(u^2-1)Q=1$. At the same frequencies the input susceptance is equal to the conductance if D is small. On the slope of the function, the power absorbed decreases

twice as fast as the admittance.

The reflection coefficient has a wider bandwidth* than the input admittance due to the fact that both the incident voltage and the reflected voltage are applied to the load. Solving for the reflection coefficient,

$$\begin{aligned} \Gamma &= \frac{G_{in} + jB_{in} - G_0}{G_{in} + jB_{in} + G_0} \\ &= \frac{1 + jQ(u^2 - 1) - (1 + Q^2(u^2 - 1)^2)R/\alpha^2 Z_0}{1 + jQ(u^2 - 1) + (1 + Q^2(u^2 - 1)^2)R/\alpha^2 Z_0} \end{aligned} \quad (5.18)$$

where $j\omega D$ is assumed to be negligible and $Z_0 = 1/G_0$ is the characteristic impedance of the inlet transmission line. The behavior of the reflection coefficient for loop coupling is very similar.

The voltage transfer function will be used in section 5.2c. The tank voltage generated by the input voltage is

$$\begin{aligned} \phi' / \phi_{in} &= \frac{Z_{\text{tank}}}{1 + Z_{\text{tank}}} \\ &= \frac{sD(sL + s^2 LC'R)}{sD(sL + s^2 LC'R) + 1 + sRC + s^2 LC} \end{aligned} \quad (5.19)$$

Reducing this to the normalized quantities, and assuming $\alpha \ll 1 \ll Q$,

$$\frac{\phi'}{\phi_{in}} \approx \frac{\alpha p^2}{1 + p/Q + p^2} \quad (5.20)$$

At resonance this gives

$$\frac{\phi'}{\phi_{in}} \approx j\alpha Q \quad (5.21)$$

* Spacing between -3dB points and frequencies where $G = B$ respectively.

When the other modes are included we may consider all the resulting circuits to be in parallel. The total input admittance is given by

$$Y_{in} = \sum_{n=1}^{\infty} \left\{ sD_n + \frac{\alpha_n^2 u_n^6 (1 + jQ_n (u_n^2 - 1)/u^3)}{(u_n^2 + Q_n^2 (1 - u_n^2)^2) R_n} \right\} \quad (5.22)$$

Collin⁽¹⁴⁾ uses the same model to analyze the case where a loop terminates the transmission line. The result is

$$Z_{in} = j\omega L_0 + \sum_{n=1}^{\infty} \frac{\omega^3 \alpha_{\ell_n}^2 L_n / \omega_n^2}{1 - (\frac{\omega}{\omega_n})^2 + j\omega / \omega_n Q_n} \quad (5.23)$$

where α_{ℓ_n} is M/L , and M is the magnetic flux of the n 'th mode which threads the loop at unit current from the transmission line. This expression may be rationalized to give a reflection coefficient similar to that obtained for the capacitively coupled cavity. L_0 is the self inductance of the coupling loop and, if it is small, a single mode at its resonant frequency gives a resistance of

$$Z_{in_n} = \alpha_{\ell_n}^2 R. \quad (5.24)$$

(c) Distributed Coupling

The model of Figure 5.4 can be extended to deal with long strap couplers and slow wave structures. The coupling capacitance and mutual inductance become distributed as shown in Figure 5.5 and the coupling structure is equivalent to an infinite number of such sections of infinitesimal length. Let z be the distance from the inlet port of the transmission line measured along the path taken by a wave in the coupling structure. Let the coupling

capacitance per unit length be given by $D k_c(z)$ and the mutual inductance by $M k_\ell(z)$. D and M are the averaged magnitudes over the coupling structure such that $k_\ell(z)$ and $k_c(z)$ average to zero and bear the z dependence of the coupling. L, C' and R are defined in Section 5.2. \underline{C} and \underline{L} are, respectively, the self-capacitance and self-inductance per unit length of the coupling element. The coupling element itself is assumed to be reflectionless except at its ends.

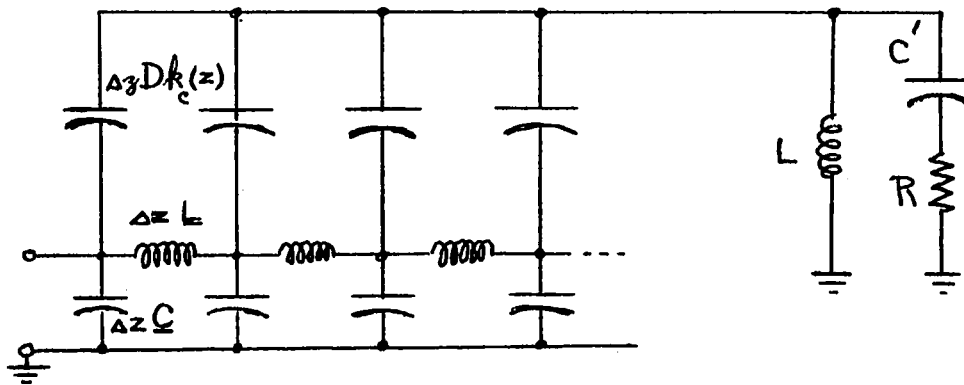


Figure 5.5 Distributed Coupling

The current $i\Delta z$ through the distributed coupling capacitance gives rise to two equal voltage waves travelling in the $\pm z$ directions and with magnitudes given by $\phi_f = \phi_r = i\Delta z Z_0/2$ where Z_0 is the characteristic impedance of the coupler. Mutual inductance generates equal but opposite voltage waves in the coupler having a magnitude $|\omega I_L \Delta z \frac{M}{2} k_\ell(z)|$. The stored magnetic energy in the cavity is almost equal to the stored electric energy and is given by $\frac{1}{2} I_L^2 L$, which defines I_L . Excitation of the cavity is modelled by current flow through $Dk_c(z)$ and voltage induced in L by the coupler current and $Mk_\ell(z)$. The phase reference for the

resonant circuit is the phase between its voltage and that at the input port of the coupling structure. If the Q of the cavity is high, the fields collapse almost simultaneously throughout the volume of the cavity.

Capacitive and inductive coupling generates a voltage in the equivalent tank circuit given by

$$\frac{\partial \phi'}{\partial z} = K_1 k_c(z)(\phi(z) - \phi') + K_2 k_\ell(z) i(z) Z_0 \quad (5.25)$$

where $\phi(z) = \phi_f(z) + \phi_r(z)$ and $i(z) = (\phi_f(z) - \phi_r(z))/Z_0$

The constants K_1 and K_2 are given by

$$K_1 = \frac{D}{C} \left(\frac{p^2}{1+p/Q+p^2} \right) \quad (5.26a)$$

and

$$K_2 = \frac{sM}{Z_0} \left(\frac{1+p/Q}{1+p/Q+p^2} \right) \quad (5.26b)$$

The coupling also induces waves in the coupling structure given by

$$\frac{\partial \phi_f}{\partial z} = K_3 k_c(z)(\phi' - \phi(z)) + K_4 k_\ell(z) \phi'; \quad (5.27)$$

$$\frac{\partial \phi_r}{\partial z} = K_3 k_c(z)(\phi' - \phi(z)) - K_4 k_\ell(z) \phi' \quad (5.28)$$

The constants K_3 and K_4 are given by

$$K_3 = sDZ_0/2 ; \quad (5.29a)$$

$$K_4 = \frac{M}{2L} . \quad (5.29b)$$

Equations 5.25, 5.27 and 5.28 form a set of three equations in three unknowns which define the voltages resulting from a specific excitation of the coupling structure. Integrating this set over z and including the excitation and a reflection Γ_t of ± 1 at the end, z_t , we obtain:

$$\phi' = \int_0^z \frac{\partial \phi}{\partial z} dz = \int_0^{z_t} (K_1 k_c + K_2 k_\ell) \phi_f dz + \int_0^{z_t} (K_1 k_c - K_2 k_\ell) \phi_r dz - \int_0^{z_t} K_1 k_c \phi' dz \quad (5.30)$$

$$\phi_f(z') = \phi_f(0) \exp(\gamma(z'-z)) + \int_0^{z'} \frac{\partial \phi_f}{\partial z} \exp(\gamma(z-z')) dz \quad (5.31)$$

$$\phi_r(z') = \Gamma_t \phi_f(z_t) \exp(\gamma(z'-z_t)) + \int_{z_t}^{z'} \frac{\partial \phi_r}{\partial z} \exp(\gamma(z-z')) dz \quad (5.32)$$

where z indicates a generation location, z' a measurement location and γ is the propagation constant of the coupling element. Obviously, these equations are coupled and cannot be easily solved except by difference equation methods. The values of D , M , k_c and k_ℓ must be obtained either from a boundary value solution of the geometry chosen, or experimentally.

In Eq. 5.32, the phase angle of all terms changes rapidly with z . The integral is much smaller than that of the absolute value of the integrand, unless the k 's change sign nearly in synchronism with the real part of $\exp(\gamma(z'-z))$. In other words, phase differences of backward travelling waves in the coupler cause cancellation of reflected power unless some of the waves in the cavity are nearly synchronized with those in the coupler.

For a lossless cavity ($R=0$), ϕ' increases until the unattenuated forward wave is reflected back toward the coupler. If $R \neq 0$, ϕ' is lower and the forward wave is attenuated with distance. This may be verified by examining the effect of ϕ_f in Equations 5.30 and 5.31. Its phase is synchronous with $\exp(\gamma(z - z'))$. $\frac{\partial \phi'}{\partial z}$ will be reduced if ϕ' is large and $\frac{\partial \phi'}{\partial z}$ is increased by ϕ_f and ϕ_r .

Alternatively we may examine the energy transfer. If the k 's are slowly changing, voltages of nearly equal magnitude and phase are induced in a long (but not necessarily straight) section of the coupling structure. Because of distributed arrival times at the inlet port, the reflected waves cancel and energy does not readily escape from the cavity once it has been distributed inside the high Q structure. However, there is a gradient in the forward wave propagating in the coupling structure and energy can be coupled into the fields unless ϕ' is large. The energy is randomized and cannot be recovered unless the integral of Eq. 5.32 is made non-zero.

The alternative to slow wave coupling is fast wave coupling, where the phase velocity is made very high. This means that the k 's change sign much more rapidly than $\cos(\gamma(z-z'))$ and the reflected power integral is small. It is thus possible to use a long straight section of waveguide very near cutoff as a coupling structure. It would be simply an extension of the transmission structure and would have an array of slots to couple power into the cavity. This would demand precision construction, but would require fewer parts and would take less room than a waveguide slow wave coupling structure.

5.3 Results of Slow Wave Coupling

The basic TEM slow wave coupling structure of Figure 5.3 has been built and tested. Preliminary measurements of Z_0 of a straight strap shows that a 50 ohm characteristic impedance would give little coupling. Several 100 ohm structures tested gave much more (but not excessive) coupling in most cavities. The presence of capacitance between sections of the structure permitted increased spacing to the ground plane at 100 ohms but resulted in pass band behavior. In the pass bands, the structure matched well to a cavity and to free space; and over half of the 1 to 4 GHz range there was less than -6 dB reflected power in free space operation. The centre frequencies of the pass bands occur at roughly even intervals and are listed in Table 5.1 for several experimental structures. The symbols are defined in Figure 5.3.

Table 5.1 Optimum Coupling Frequencies

<u>W</u>	<u>w</u>	<u>p</u>	<u>f_{optimum}</u>
10.5 cm	1.23 cm	5.1 cm	2.7 GHz, etc.
8.7 cm	1.23 cm	6.4 cm	2.0 GHz, 3.0 GHz, etc.
13.2 cm	1.00 cm	4.0 cm	0.92 GHz, 2.5 GHz, etc.
12.6 cm	1.23 cm	6.7 cm	2.45 GHz, etc.

$h = 1 \frac{1}{2}$ cm, thickness = 0.2 cm

Figure 5.6 shows a prototype 80 litre cavity which was used for thawing deep frozen, fluorocarbon-DMSO perfused canine kidneys⁽⁵⁵⁾. The organ was held in teflon and immersed in 1 litre of FC47 fluoro-carbon, and placed on a 1" thick nylon turntable. The walls were covered with perforated iron sheeting, which increased the losses in

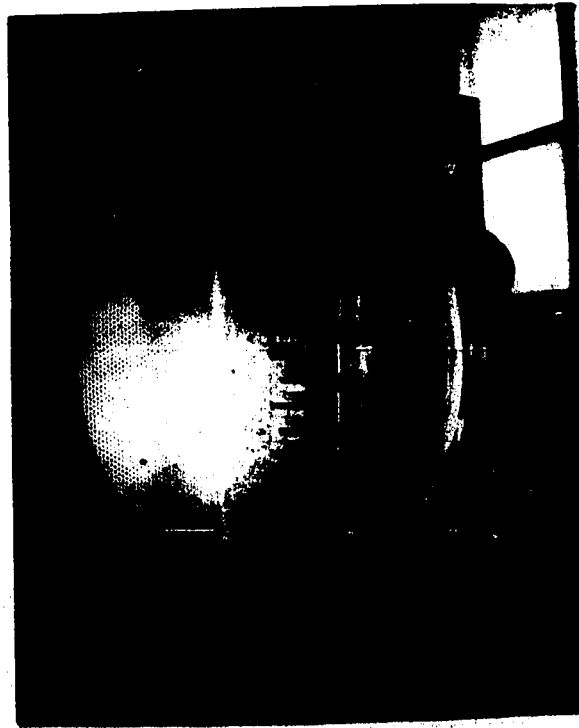


Figure 5.6 Experimental Cavity for Thawing Live Organs



Figure 5.7 Reflections from Experimental Cavity

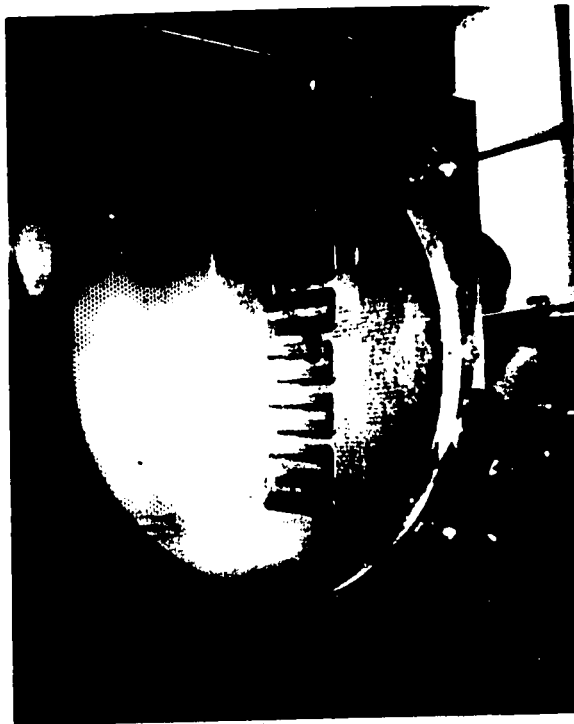


Figure 5.6 Experimental Cavity for Thawing Live Organs



Figure 5.7 Reflections from Experimental Cavity

the metal and in combination with the nylon gave a limited Q_0 . This base loading guaranteed good VSWR and limited the maximum field concentration in the cavity.

When the small element and long strap coupling structures were used, the reflections from the cavity were unacceptably high. With the last slow wave coupling structure of Table 5.1, the maximum reflection was reduced from -1dB to -6dB and typical reflections were about -10dB. The efficiency of heating was about 55% for a 500 ml water load while for 3 litres of water it was over 85%. The system was made useable by the new matching technique; organ heating rates of from 2° C to 4°C/sec were achieved in the ranges -79°C to +30°C and +4°C to +30°C⁽⁵⁵⁾. Uniformity of heating was also improved, partly by simultaneously rotating and oscillating the nylon disc⁽⁴⁴⁾.

In Figure 5.7, the reflection coefficient of this cavity is shown for a multiplicity of loading conditions as the turntable rotates. This and the next two photos were obtained by a frequency domain reflectometer and the vertical axis is reflected power, in dB. Zero dB means that the energy is totally reflected, and a 0dB trace was included by removing the cavity completely from the instrument. The -10dB line 2 major divisions lower, for example, represents 10% reflected power. Similarly, -3dB is 50%, -6dB is 75% and -20dB is 1% reflected power. The lower a trace is on the photographs, the better the cavity is matched. The horizontal axis is the frequency, and Figure 5.7 displays the 2.05 to 3.05 GHz band.

A shield was placed over the coupler in the cavity shown in

an attempt to obtain improved matching by reducing the rate of coupling to the cavity. As stated, the horizontal and vertical scales are 100 MHz and 5 dB per division respectively. The single line indicates 0dB, with a marker at 2450 MHz. The shield covered 40% of the area of the coupling structure and increased the maximum reflected power in the 2450 \pm 50 MHz ISM band from -6dB to -4dB. This is roughly proportional to the area covered. The load was only 200 ml and larger loads gave a better match. The bandwidth has been narrowed by the single stub tuner but it is still very wide compared to the useable bandwidth given by small element couplers. The failure of the shield to improve the match indicates that the cavity is not too heavily coupled, and that the reflections seen are from the ends of the coupling structure.

In Figure 5.8 the slow wave technique and a capacitive probe are compared in a 1100 litre empty aluminum cavity. The first structure of Table 1 has been used, so the frequency chosen was 2.6 GHz \pm 50 MHz. The vertical scale is still 5 dB/division, while the horizontal scale is now 10 MHz/division. The capacitive probe produced the bottom trace and the slow wave structure the upper trace. The 0 dB lines follow the graticule lines with a levelling error of about \pm 1 dB. This is a difficult cavity to couple to because of its very high Q (and therefore high ϕ' according to the theory), but there are bands where the slow wave structure couples quite well.

In Figure 5.9 the frequency has been dropped to 1.8 GHz where a long strap radiator was optimized. The slow wave structure was not quite optimum, but it coupled well. The scale factors are

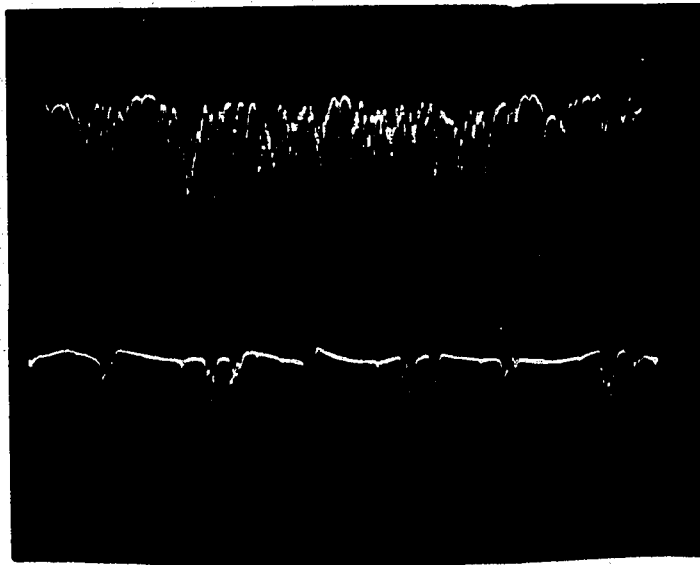


Figure 5.8 Reflections from Slow Wave Coupler and Capacitive Probe

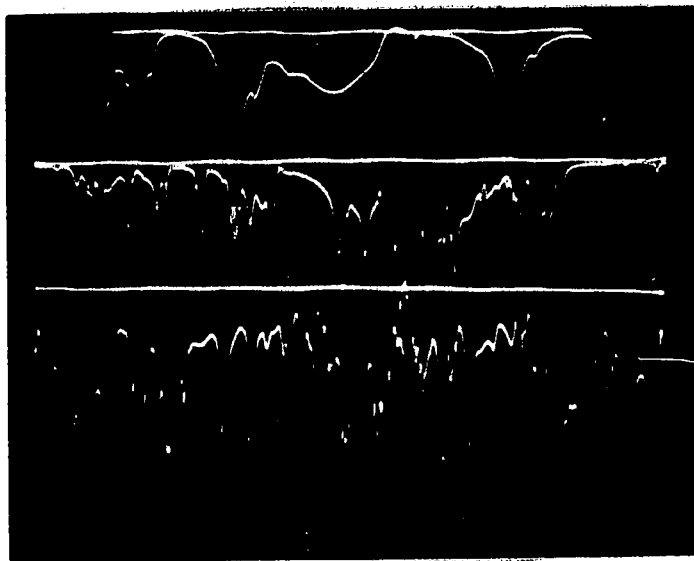


Figure 5.9 Reflections; Probe, Strap and Slow Wave Coupler

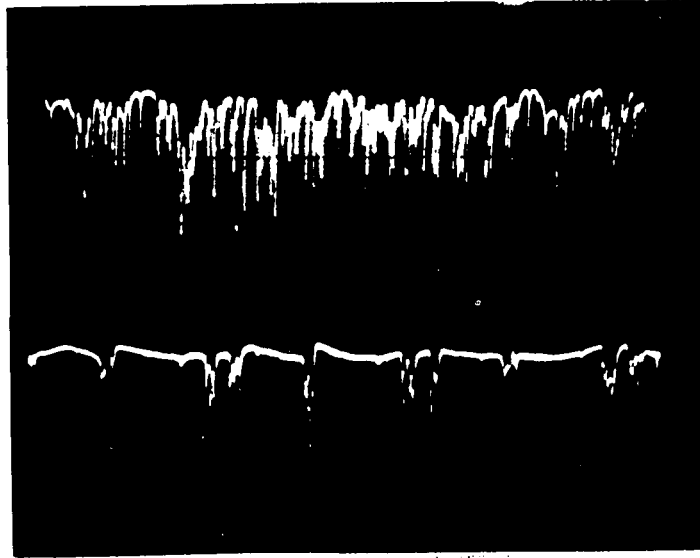


Figure 5.8 Reflections from Slow Wave Coupler and Capacitive Probe

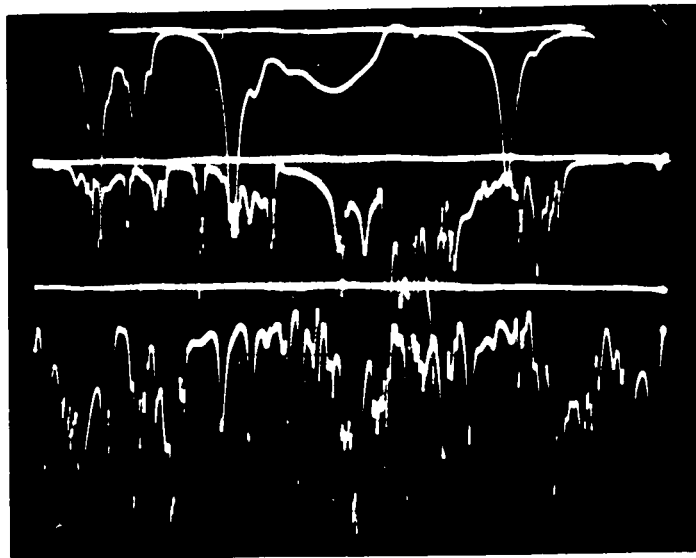


Figure 5.9 Reflections; Probe, Strap and Slow Wave Coupler

the same. From top to bottom are the reflection coefficients of the capacitive probe, long strap and slow wave structure respectively, in the same large cavity with a 1 litre water load. The improvement from the top to bottom trace is typical of the behavior of these three structures.

In this too-large cavity the slow wave structure was able to match 11 litres of water to the magnetron with about -10 dB average reflected power. The previous cavity was superior at the operating frequency and had sufficient base load to match well when used with the slow wave coupling structure to heat any load. A well designed cavity and the new coupler give a good system; if either is poor, the reflections are more severe.

Striplines are smaller than waveguides, which is physically convenient. However, this means that waveguides can have a much higher power handling capacity. Several waveguide slow wave structures meet the theoretical requirements derived in Section 5.3. A WR284 slow wave structure was constructed as shown in Figure 5.10, with lengths $l_1 = 10 \frac{1}{2}$ cm, $l_2 = 3 \frac{1}{2}$ cm and the slots gradually increasing to 0.6 cm in $2 \frac{1}{2}$ periods. The free space reflected power was less than -20 db of the incident power at 2450MHz. When tested in the large 1100 litre cubic cavity it gave good matching similar to the stripline structure, although the guide wavelength was almost double the free space wavelength. The path l_1 was large compared to a wavelength.

It was noted that if the reactance coupling could be suppressed, far field effects would give constant radiation resistance. With cavities of the size normally found in

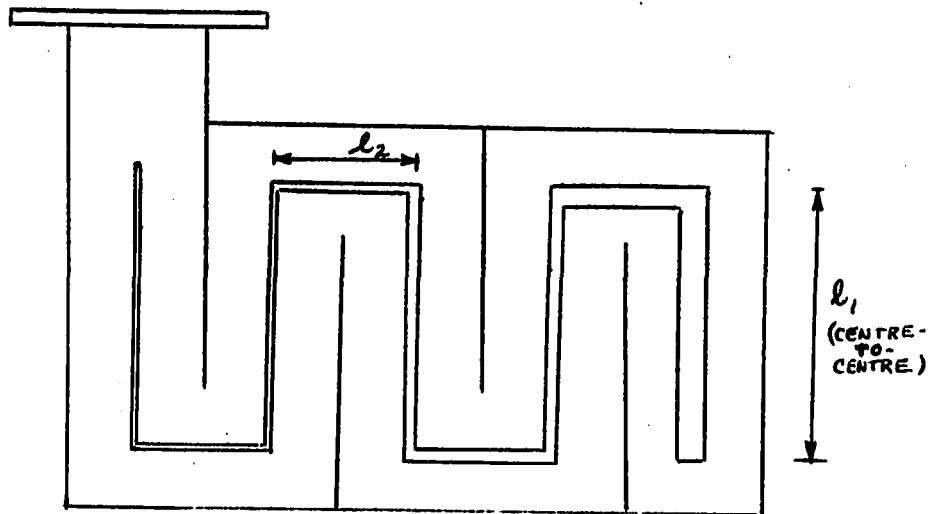


Figure 5.10 Waveguide Slow Wave Coupler; TE₁₀

microwave systems, experiments with small elements always revealed the mutual reactance (near field) behavior predicted in Section 5.2. It is possible to obtain good VSWR and heating uniformity in lossy enclosures by using standard high gain antennas, but the unused power is not returned to the load, and efficiency is usually poor. Other special antennas are used for concentrated heating^{(54),(72)} and are not treated here.

When the slow wave structure was used to excite a single mode in small cavities, it was possible to obtain a good match over a wide range of loading conditions. The problem of frequency pulling by the load is still present, however, and the cavity should either be tuned or be designed for multimode operation. This will be treated in the next chapter.

5.4 Conclusions and Practical Design Considerations

The simple small element gives a surprisingly tolerant match, and may be used in many situations where the load is quite predictable. For example, from Eq. 5.18, a loading range of from 0.333 to 3 times the optimum R gives a maximum of -6 dB reflected power. The 3 dB points for a matched load are about 2.4 times as far apart as f_n/Q . However, k_c (or k_λ) varies and the match is very dependent on locations of both coupler and load. This is overcome by the long strap coupler, giving more useable modes and an even wider range of acceptable load variations. The slow wave couplers have been shown here to suppress the remaining problems of strong reflection for some modes and random matching by the stub tuner.

The slow wave structures used are still rather large, approximately a full wavelength in width. The optimization of these structures has only been carried as far as selecting geometries that give pass bands at the desired frequencies. It is likely that structures of other dimensions would give further improvement in a cavity, although the best match was obtained at the frequency corresponding to the optimum free space radiation. To check for this, a difference equation computer program for Equations 5.30, to 5.32 could be developed. The coupling could be increased, since the shielding test indicated that reflections were increased somewhat by reducing the effective area of the coupler. However, in very high Q cavities, it may be an advantage to shield the coupling structure to spread the gradient of the incident wave

in the coupling structure over its length. It may be possible to parallel more than two sections of coupling structure to obtain increased coupling.

There are no resonances near some frequencies, and coupling is poor with any structure. Energy is then reflected from the end of the coupling element. It may be that the magnetron locks to these frequencies, as indicated by Huang⁽³⁶⁾. As he shows, it is desirable that the frequency parameter of the load locus of the magnetron Rieke diagram increase while the operating frequency of the magnetron decreases. This decreases the frequency drift of the magnetron-cavity system as detuning occurs. Similarly, by choosing the correct line length from the magnetron to the end of the coupling element, the end reflections may be placed in a stable operating region on the Rieke diagram, or possibly placed so that the magnetron does not operate at this frequency.

From energy considerations, ϕ' in a completely lossless cavity will rise until total reflection occurs. In low loss structures, there is some power absorption, but not enough to protect all magnetrons. Then it is necessary to use a permanent minimum load. This base load broadens the modes and also reduces the reflected power at the centre frequencies. The efficiency of the cavity is given by $Q_0/(Q_0+Q_r)$ where $Q_0 = \frac{Q_e + Q_w}{Q_e Q_w}$ and is due to the various base loads. The use of the slow wave structure permits higher unloaded Q and can thus improve efficiency while permitting a system which can be operated unloaded. It should be noted that as the Q is raised and coupling improved the fields in the interior

are increased and there will be more leakage of energy from the cavity unless the door seal is well designed⁽⁴⁶⁾.

A further improvement in heating efficiency has been obtained by several workers^{(32),(43)} by placing the load at the focus of an elliptical structure. An alternative is the apex of a pyramid. In this type of cavity, ξ^2 increases as the focus region is approached. The same effect will be obtained in the next chapter by adjusting F.

CHAPTER SIX

A SMALL MULTIMODE CAVITY FOR RODLIKE LOADS

In this chapter it is shown that vanes inserted into a small rectangular cavity make multimode operation possible. Tests on a preliminary design are given and again the slow wave coupler is shown to reduce the effect of load variations.

6.1 Microwave Heating of Rodlike Loads

Many presently used microwave threadline driers use a single resonant mode which is tuned to the operating frequency of the magnetron. This has the advantage that the applicator is small, resulting in high efficiency and a wider bandwidth. However, the load pulls the resonant frequency downward, and this problem is aggravated by small size. A typical cavity is shown in Figure 6.1⁽³⁶⁾. In this mode the electric field is parallel to the surface of the load and the standard small element coupler is shown. The cavity may be tuned by adjusting its volume or shape. In this type of system low loss, physically small filaments can be heated, provided that the loading does not vary.

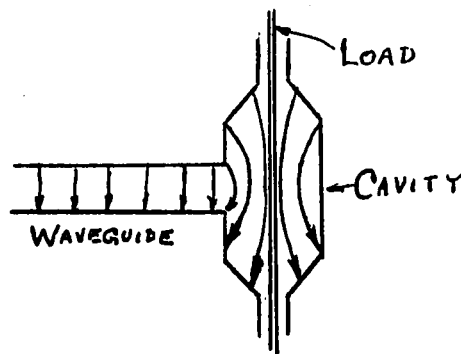


Figure 6.1

TM₀₁₀ Threadline Applicator

A load may be considered heavy if it results in a loaded Q considerably less than half of the unloaded Q , Q_0 . Altman⁽²⁾ gives a perturbation analysis for Q and detuning of loaded cavities, including cases where the load may not be parallel to the electric vectors. The effect of a load on losses is given by

$$\frac{1}{Q} - \frac{1}{Q_0} = \frac{\epsilon_r'' \epsilon_0 \int_V \hat{E}_0^* \cdot \hat{E} dV}{\frac{1}{2} \int_V (\epsilon_0 \hat{E}_0^* \cdot \hat{E} + \mu_0 \hat{H}_0^* \cdot \hat{H})} \quad (6.1)$$

The subscript 0 is used for unperturbed variables while the perturbed variables are unsubscripted. The denominator is equal to the stored energy if the perturbation is small. If the load is parallel to the electric field vectors,

$$\frac{1}{Q} - \frac{1}{Q_0} = \frac{1}{\epsilon_r'' F \xi^2} \quad (6.2)$$

The efficiency of heating is given approximately by $Q(1/Q - 1/Q_0)$. If the volume is decreased, the stored energy decreases and the wall losses decrease also, but more slowly. Therefore the efficiency increases even though Q_0 is reduced.

This analysis also gives the detuning of the resonant frequency ω_n due to a perturbation:

$$\frac{\omega_n - \omega_{n_0}}{\omega_n} = - \frac{\int_{\Delta V} [(\epsilon - \epsilon_0) \hat{E}_0^* \cdot \hat{E} + (\mu - \mu_0) \hat{H}_0^* \cdot \hat{H}] dV}{\int_V (\epsilon_0 \hat{E}_0^* \cdot \hat{E} + \mu_0 \hat{H}_0^* \cdot \hat{H}) dV} \quad (6.3)$$

If ϵ_r' is greater than one, as in ordinary dielectrics, the cavity resonates at a reduced frequency; while for plasmas, where the dielectric constant is less than that of free space, the resonant frequency is raised. A small metal object stores little energy at high frequencies (equivalent to $\mu \rightarrow 0$ and $\epsilon_r' \rightarrow \infty$ ⁽²⁾), and it may be shown that a metal perturbation at one of the walls results in an increase of resonant frequency if it is located in a region of predominantly magnetic energy and a decrease in frequency for electric energy. This is the standard method of tuning a cavity to compensate for detuning due to the load. The denominator in Eq. 6.3 decreases with the cavity volume and detuning becomes more severe if the filling factor is increased by using a smaller cavity.

Huang⁽³⁶⁾ showed that a magnetron can be made to pull into the operating range of a cavity under favorable conditions. As the anode voltage of a magnetron fluctuates due to the power supply ripple its resonant frequency changes, often by more than the bandwidth of the cavity. If the locus of the load reflection coefficient and the magnetron operating point change in opposite directions on the Rieke diagram as frequency changes, the system becomes more stable. A circulator was used to protect the power source, and a reflecting iris and phase shifter to rotate the locus of the load. Such a system is expensive, but it may be needed to heat a thin, low loss threadline effectively.

There are several other techniques in use for rodlike loads where $\epsilon_r'' \Delta V$ is large. A travelling wave applicator can be made by generating an electric field component parallel to the

axis of a waveguide and passing the filament or rod through it axially^{(65),(17)}. This avoids tuning problems but can lower efficiency. Double ridged waveguides can be used where the load is heavy enough so that the electric field need not be kept parallel to the load^{(8),(41)}. Elliptical cavities have been designed to control ξ^2 ^{(32),(43)}. Microwave ovens have been used for tests but Bhartia et al have correctly noted that these cavities are not designed to operate with rodlike loads because of their size⁽⁷⁾. They selected a single high order mode and tuned the cavity to compensate for loading. Using an alternate technique given below, multimode operation in a small volume is achieved and a high filling factor can be maintained with reduced detuning.

Plasmas usually are rodlike and are heated in a great variety of applicators, as evidenced by a large collection of microwave plasma references which was published in the Journal of Microwave Power⁽³⁹⁾. Examples are the coaxial cavity of Fehsenfeld and Broida⁽²⁰⁾ and the TE_{10n} cavity shown in Figure 6.2, or the same structure without an iris⁽⁵⁰⁾. At present microwave plasmas are mainly a research tool, although ozone manufacture has long been carried out in other types of plasmas. With small element coupling, the difference in Q of cavities before and after ignition of the plasma is so great that the magnetron must be protected by a device such as a circulator. The applicator of this chapter or a slow wave structure⁽⁹⁾ can be used to overcome this problem.

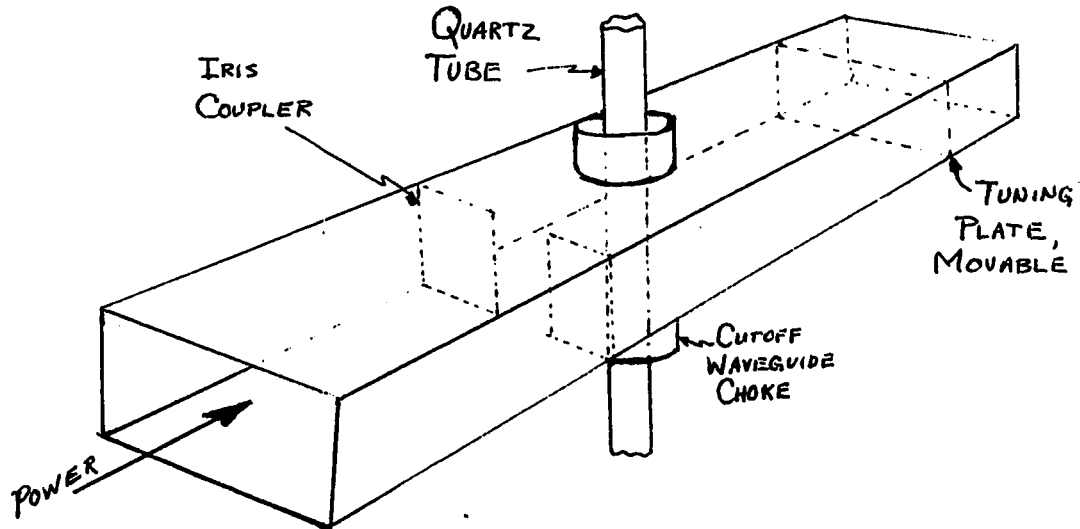


Figure 6.2 TE₁₀₃ Plasma Cavity

6.2 Metal Plates in a Rectangular Cavity

The modes of a rectangular cavity can be made spatially degenerate but only two of the three orientations of a mode usually give good coupling between the electric field and a rodlike load. Of these modes the TE_{m0n} modes are particularly promising because their electric vectors are always perpendicular to one pair of walls and their resonant frequencies are completely independent of the distance between these walls. In addition, if several of these structures (or for that matter any set of resonant structures) are coupled together the composite structure exhibits new resonant frequencies. Thus plates may be introduced into a rectangular cavity perpendicular to the electric vectors of the desired pattern, resulting in a multimode structure. A loop-coupled small multi-

mode cavity based on this principle is shown in Figure 6.3 and its input impedance versus frequency characteristic is sketched in Figure 6.4.

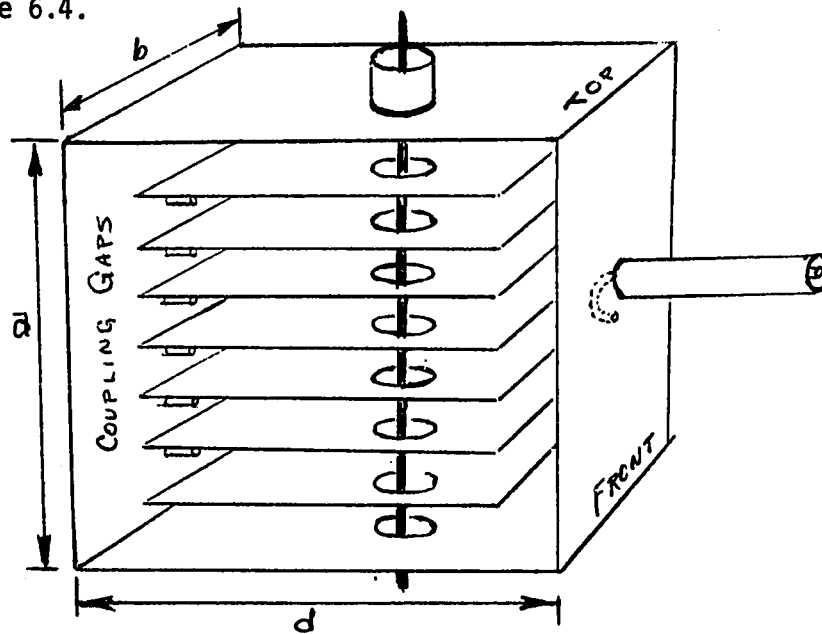


Figure 6.3 Vaned Multimode Test Cavity

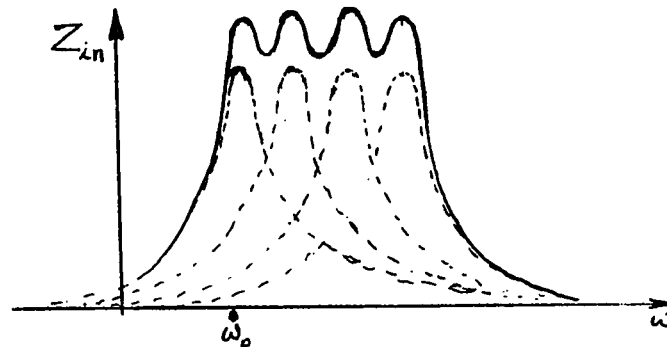


Figure 6.4 Coupling-induced Multimode Behavior

In the TE_{m0n} mode the elementary cavities formed by the plates carry a TE_{m0} waveguide mode which is reflected between end walls of the cavity⁽⁵⁶⁾. Resonance occurs at the frequency where these walls are $n/2$ guide wavelengths apart. In Figure 6.5 three such cavities are shown coupled at the ends and the centres. There

are two ways in which adjacent cavities can interact, resulting from combinations of spatial orientation (or phase) of the same mode in the two structures.

If the modes are in phase, as in cavities 1 and 2, the presence of vanes does not materially change the field pattern. If the orientations are opposed spatially, as in cavities 2 and 3, the fields diffract through the coupling holes and cancel each other. End coupling shortens the energy path length resulting in an increased resonant frequency. In Figure 6.5 there are three resonant frequencies corresponding to 0, 1 or 2 phase inversions. Since there are two ways to produce a single phase inversion, this mode is doubly degenerate, and could give two modes with stagger-tuned cavities.

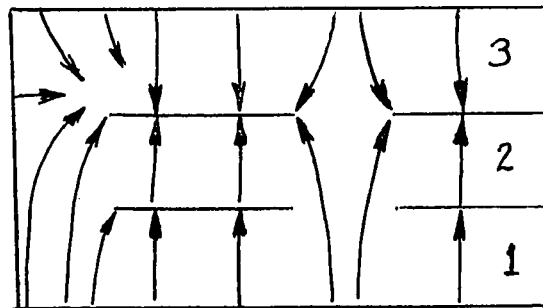


Figure 6.5 Coupled TE₁₀₁ Cavities

A rat-race resonator is shown in Figure 6.6. In this structure the reflection coefficient for a wave travelling around the ends is nearly zero. Resonance occurs when the phase of the fields in the cavity is constant. This need not require electric field nulls at the ends, and the wave can simply propagate around the loop;

hence the name. The opposed orientation in the two cavities which are coupled at both ends is a rat-race mode with possible strong reflections at the ends of the path. Many rat-race modes are permitted in the cavity of Figure 6.3, and resonant frequencies lower than the basic TE_{m0n} resonance occur, provided that the TE_{m0} waveguide mode propagates in the elementary cavities.

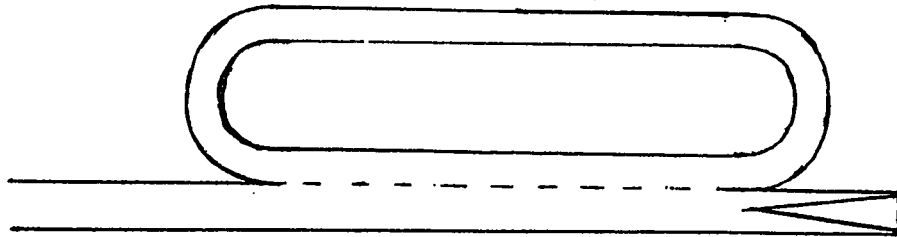


Figure 6.6

Rat-race Resonator

The problem of coupling to this structure is at least as difficult as to larger multimode cavities. Small coupling elements give the type of behavior described in Section 5.2 and cannot adequately handle detuning problems and a wide loading range. When a slow wave structure is employed, this problem can be alleviated. There is a physical problem in placing the slow wave structure in one of the elementary cavities, since it competes for space with the load. However, if the coupling structure is placed in the coupling gaps as shown in Figure 6.7 there are several frequencies at which the system becomes quite insensitive to load changes.

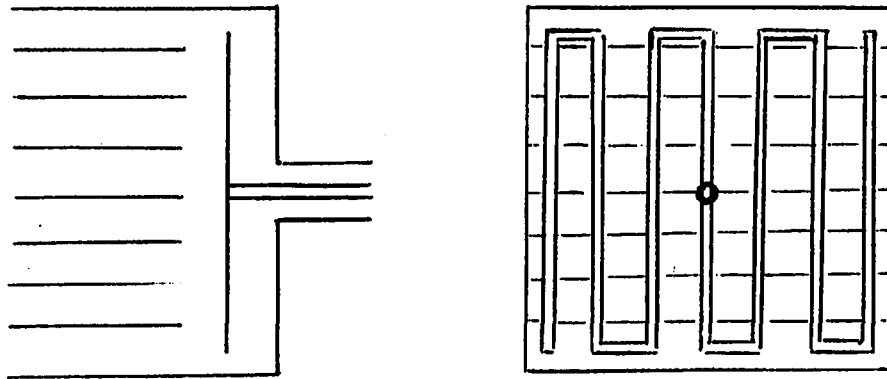


Figure 6.7 Vaned Cavity with Slow Wave Coupling Structure

6.3 Experimental Cavity

The cavity shown in Figures 6.3 and 6.7 was constructed of brass plate. The inside dimensions of the outer cavity were width $b = 16$ cm, depth $d = 17\frac{1}{2}$ cm and height $a = 17$ cm. The vanes extended the full width of the cavity and were only $13\frac{1}{2}$ cm deep, leaving coupling gaps 2 cm deep at both the front and back of the elementary cavities. Seven vanes each 1.6 mm thick, were placed equidistant in the cavity, forming 8 elementary cavities 2 cm in height. The vanes and two of the cavity walls had $2\frac{1}{2}$ cm diameter coaxial holes centered $5\frac{1}{2}$ cm from one side of the cavity; and 3 cm long cut off waveguide chokes were used to prevent leakage. The off centre location of the holes permitted good coupling to the TE_{10n} or TE_{20n} modes. However, the holes were centred front to back and the coupling to the TE_{n02} modes was very weak. Loads consisting of 7, 14 and 19 mm internal diameter pyrex glass tubes filled with water were placed through the holes. To lower the Q_0 , the structure was not soldered.

The cavity was coupled by a loop, a probe and a waveguide, as well as the third slow wave coupling structure listed in Table 5.1. When an electric probe was placed in the bottom cavity, many modes were observed, including families of modes corresponding to the resonances of the elementary cavities and various alignments of the fields. However, these modes coupled best at certain loading conditions and, as predicted by Section 5.2, the cavity was not yet insensitive to loading. When probe, loop or waveguide coupling was used in the front face in one of the coupling gaps, the same behavior was observed, with somewhat fewer modes.

The slow wave structure performed much better, however. This structure was oriented both perpendicular to the vanes, as shown in Figure 6.7, and parallel to them. The 2 cm spacing between vanes was the same as that between the long conductors of this coupler, and the middle vane and transmission line were both centred in one face. Thus for the parallel orientation these conductors of the slow wave coupling structure were centred on the planes between cavities.

Modes of the elementary cavity and mode density for the composite structure are given in Tables 6.1 and 6.2 respectively. This technique has increased the number of modes between 2 and 4 GHz from 2 to about 50. Because of rat race modes, resonances started at as low as 850 MHz and the cavity design provided three modes near 915 MHz. The other potentially usable frequencies are listed in Table 6.3. There are many modes which do not result in good coupling but for several families the cavity could be made, without tuning, to accept a heavy dielectric load.

Table 6.1 Single Resonator Resonances

TE ₁₀₁ - 1.269 GHz	TE ₂₀₃ - 3.18 GHz
TE ₁₀₂ - 1.953 GHz	TE ₃₀₂ - 3.292 GHz
TE ₂₀₁ - 2.06 GHz	TE ₃₀₃ - 3.808 GHz
TE ₂₀₂ - 2.53 GHz	

Table 6.2 Modes per 100 MHz

<u>f centre</u>	<u>Modes</u>	<u>f centre</u>	<u>Modes</u>
2.05	4	2.65	4
2.15	5	2.75	7
2.25	5	2.85	6
2.35	4	2.95	7
2.45	2	3.05	7
2.55	5		

Table 6.3 Frequency Bands for Test Cavity

<u>Empty Cavity Frequency GHz</u>	<u>Coupling Orientation</u>	<u>Effective Frequency Pulling</u>	<u>Comments</u>
1.3	parallel	-	mode separation wide
1.97	perpendicular	upward	
2.05	parallel	none	usable
2.36	perpendicular	none	usable
2.36	parallel	down	
2.53*,2.65	perpendicular	none	usable
2.53*,2.65	parallel	down	
3.0	parallel	none	usable
3.0	perpendicular	spread	separation wide

* Efficiency was low because load was centred in null.

In the empty cavity the placement of the slow wave coupling structure was designed to excite only the lowest frequency member of a family of modes, i.e. the aligned mode*. When the loads were used, the other members of the family had a reduced reflection coefficient because the fields decayed with distance from the centre of the cavity. This gave the effect of pulling the operating frequency upward to compensate for the dielectric. Since a distributed coupler was employed, the effect of the cavity Q was much less than for small element couplers and the cavity gave a base load. As a result there were frequencies at which the magnetron would be protected for none or all test loads.

In the test cavity, however, good performance was difficult to achieve and factory alignment on a reflectometer would be needed to produce an industrial cavity. As indicated in Table 6.3, the load still pulls all the resonant frequencies down and the effective centre frequency very often is pulled out of the magnetron's band. With large gaps and only seven vanes the mode separation is considerably more than that for a 80 litre rectangular cavity.

The efficiency could not be measured directly for the trial cavity because the useable bands did not correspond to an ISM band where high power was available. The mode density prevents accurate Q measurements in the useable bands but at other frequencies it was possible to isolate modes. The unloaded Q's of the cavity were between 270 and 850. A 17 mm pyrex tube filled with water gave Q's corresponding to efficiencies from 75% to 93% except for the weakly coupled TE_{m02} modes (35%) where the load was in an electric

* It could be made to excite the other modes by adjusting a single stub tuner at the input to the cavity.

field null. A 7 mm water load was only slightly less efficient, indicating that the large mass of water is reducing \hat{E} well below \hat{E}_0 in Equations 6.1 and 6.3.

6.4 Application of the Vaned Rectangular Cavity

The small test cavity gives multimode behaviour similar to that shown by the cavities used in microwave ovens. A distributed coupling structure reduces sensitivity to loading. The number of plates should be increased and the coupling gaps made smaller to decrease mode separation. (This would have made interpretation of tests difficult.) Other configurations of the slow wave coupling element should be tested to improve the number of well coupled modes in a band and waveguide slot array coupling may make construction easier. Deliberate use and splitting of degeneracies could further help.

This cavity obviously cannot be made as small as the TM_{010} cylindrical structure, and it has a large internal surface area which must carry current. Therefore it is not capable of as high an efficiency. However, there is a wide range of loads between the filaments described by Huang and the sort of loads that are heated in 20 litre or larger microwave oven cavities. The single mode cavities suggested for this range are very susceptible to detuning, and the previous coupling elements are affected by Q changes. There is now no need to use a single mode cavity if the load gives $\epsilon_r'' \epsilon_s^2 F$ larger than $1/Q_0$ in a TE_{101} cavity.

There are bands for which, in the empty cavity, the upper member of the family is coupled best. Such a band could be used to ignite and efficiently sustain a plasma, which would pull all the modes up in frequency.

CHAPTER SEVEN

Conclusions

Microwave travelling wave web-heating systems were found to be limited by poor control of heating rates in the applicator; through both the filling factor F and the field concentration factor ξ^2 . It was shown that the TEM mode facilitates the control of both factors. Of the possible designs examined, the rectangular coaxial structure was found to be best suited for many purposes. Detailed analysis of this structure was presented and charts were prepared for the design of practical rectangular coaxial applicators. The computer technique developed may be used for other TEM applicators by simply modifying the subroutines that assign charge and measurement locations.

The cutoff frequencies of higher order modes have not been calculated for the rectangular TEM structure⁽⁶⁾. Perturbation analysis has been used throughout, and the analysis should be extended to predict the effect of very heavy loads^{(13),(63),(67)}. Other TEM structures, such as those suggested in Chapter 2 could be used to overcome the problem of energy concentration at corners of the conductors. When the web is oriented at an angle to the electric field, the attenuation may be greatly reduced, and a structure to accomplish this was suggested in Appendix II.

It was shown that although the physical process is different, the inhomogeneity in moisture content in a drying web can be conservatively estimated by assuming that it is the same as the inhomogeneity in the initial heating profile. Design charts

have been prepared to assist in choosing an applicator attenuation, and the effect of reflections from the edge of the web have been examined. The non-electrical variables such as temperature and air flow have been related to the applicator design and their effect on homogeneity can be predicted theoretically, although it was necessary to assume batch heating, which is not very general.

Cavity applicators were found to be limited by the reflection coefficient of the coupling structure. It has been shown that a slow wave coupling structure can reduce reflected power, but some base load is still needed to protect the magnetron. Several slow wave coupling structures have been constructed and tested and one of them was found to improve the performance of a biomedical microwave heating system.

It has been shown that it is unnecessary to use single mode applicators for rodlike materials in many instances where this has been done to improve efficiency. The alternative small multimode cavity has only demonstrated the feasibility of such an applicator, however, and must be redesigned to produce a practical model. Enough detail has been given to guide such a design.

Three patent disclosures have been filed with Canadian Patents and Development Corporation in the interest of the University of Alberta. These cover the use of the TEM mode in web applicators, the use of slow wave structures as coupling elements for cavities and the small multimode cavity for rodlike materials.

REFERENCES

- 1 Allan, G.B., Microwave Drying of Solids, M. Sc. Thesis, University of Alberta, June 1967.
- 2 Altman, J.L., Microwave Circuits, Van Nostrand, N.Y., 1964.
- 3 Anon, "Survey of Selected Industrial Applications of Microwave Energy", US Dept. HEW Publication BRH/DEP 70-10, 1970.
- 4 Anon, "Leakage Variations from Microwave Ovens", US Dept. HEW Bulletin BRH/DEP 70-10, 1970.
- 5 Aslan, E.E., "Electromagnetic Radiation Meter". IEEE Trans. MTT 19(2) pp249-250 (Feb.1971).
- 6 Beaubien, M.J. and Wexler, A., "An Accurate Finite-Difference Method for Higher Order Waveguide Modes", IEEE Trans. MTT 16(12) pp1007-1017 (Dec. 1968).
- 7 Bhartia, P., Kashyap, S.C., Stuchly, S.S., and Hamid, M.A.K., "Tuning, Coupling and Matching of Microwave Heating Applicators Operating at Higher Order Modes", JMP (Journal of Microwave Power) 6(3) pp221-228 (Oct. 1971).
- 8 Bleackley, W.J., VanKoughnett, A.L., and Wyslouzil, W., "Ridged Waveguide Microwave Applicators" JMP 7(1) pp23-28 (March 1972).
- 9 Bosisio, R.G., Weissfloch, C.F., and Wertheimer, M.R., "The Large Volume Plasma Generator (LMP)", IMPI Symposium, Ottawa, Canada (May 1972), paper 5.2
- 10 Bostian, C.W. and Wiley, P.H., "Concerning the Moment Solution for the Charge Distribution on a Square Conducting Plate", Proc. IEEE 59(11) p1639 (Nov. 1971).

- 11 Boswell, J.M., "Low Voltage Magnetron for Consumer Microwave Ovens", JMP 6(4) pp305-312 (Dec. 1971).
- 12 Brown, W.C., "High Power Microwave Generators of the Crossed-Field Type", JMP 5(4) pp245-259.(Dec. 1970: 8 refs.)
- 13 Chatterjee, S.K. and Chatterjee,R., "Dielectric Loaded Waveguide-a Review of Theoretical Solutions", Radio Electron. Eng. 30 pp145-160 (Sept, 1965), pp195-205 (Oct.), pp259-288(Dec.) and pp353-364 (Dec. 1965). Includes 165 refs.
- 14 Collin, R.E., Foundations for Microwave Engineering, McGraw-Hill 1966.
- 15 Copson, D.A., Decareau, R.V., "Microwave Ovens" in Okress (Ref. 51) Microwave Power Engineering (Vol. II) pp6-27 1968.
- 16 Crapuchettes, P.W., "Magnetrons as Generators of Microwave Power" in Okress (Ref. 51) Microwave Power Engineering (Vol I) pp18-42.
- 17 Cumming, W.A., "Apparatus for Dielectric Heating" US Pat. 3,457,385 (1969).
- 18 Davies, J.B. and Muilwyck, C.A., "Numerical Solution of Uniform Hollow Waveguides with Boundaries of Arbitrary Shape", Proc. IEE (Lond.) 113 pp277-284 (Feb. 1966).
- 19 Dunn, D.A., "Slow Wave Couplers for Microwave Dielectric Heating Systems", JMP 2(1) p7 (1967).
- 20 Fehsenfeld, F.C. and Broida, H.P., "Microwave Discharge Cavities Operating at 2450 MHz", Rev. Sci.Instr. 36(3) pp294-298 1965.
- 21 Foulds, K. and da S. Sampaio, P., "Measurement of Electric Field Distribution in a Waveguide Containing a Dielectric Slab", Proc. IRE 47 pp1663-1667 (1959).

- 22 Frey, A.H., "Biological Function as Influenced by Low-Power Modulated R.F. Energy", IEEE Trans. MTT 19(2) pp153-164 (Feb. 1971)
- 23 Gerling, J.E., "Microwave Heating Patents" and "Applicators and Their Design", Genesys Systems, Mountain View, (1970: 428 refs.).
- 24 Gerling, J.E., "Striping Apparatus for Highways", US Pat. 3,472,200 (1969).
- 25 Goubau, G., "Surface Waveguides", in Okress (Ref. 51), Microwave Power Engineering (Vol. I), pp214-227 1968.
- 26 Grant, E.H., et al "Dielectric Behavior of Water at Microwave Frequencies", J. Chem. Phys. 26 p261 (1957).
- 27 Green, H.E., "Numerical Solution of Important Transmission Line Problems", IEEE Trans. MTT 13(5) pp676-692.(Sept. 1965 28 refs.)
- 28 Grimm, A.C., "RCA 915 MHz Power Oscillator for Microwave Cooking and Industrial Heating Applications", JMP 4(1) pp5-10 (Mar. 1969).
- 29 Guenard, P., "High Power Linear Beam Tube Devices", JMP 5(4) pp261-267 (Dec. 1970).
- 30 Gupta, R.R., "Accurate Impedance Determination of Coupled TEM Conductors", IEEE Trans. MTT 17(8) pp479-489 (Aug. 1969).
- 31 Hamid, M.A.K., Stuchly, S.S., Bhartia, P., and Mostowy, N., "Microwave Drying of Leather", JMP 7(1) pp43-49 (Mar. 1972).
- 32 Hamid, M.A.K., Stuchly, S.S., and Bhartia, P., "Tuning and Excitation of a Prolate Spheroidal Cavity Resonator for Microwave Drying" JMP 6(3) pp213-220 (Oct. 1971).
- 33 Harrington, R.F., Field Computation by Moment Methods, Macmillan, NY 1968.

- 34 Harris, J.Y., "Electronic Product Inventory Study",
US Dept. HEW Publication BRH/DEP 70-29 (1970).
- 35 Heenan, N.J., "Travelling Wave Driers" in Okress (Ref. 51),
Microwave Power Engineering (Vol II) pp126-144 1968.
- 36 Huang, H.F., "A Microwave Apparatus for Rapid Heating of Thread-
lines", JMP 4(4) pp288-293 (Dec. 1969).
- 37 International Microwave Power Institute, Proceedings of IMPI
Short Course for Users of Microwave Power, IMPI, Box 1556
Edmonton . (See article by Kumpfer, Nov. 1970 and May 1972.)
- 38 James, C.R., Voss, W.A.G. and Tinga, W.R., "Some Factors Affecting
Energy Conversion in Multimode Cavities" JMP 1(3) pp97-107 (1966)
also in Okress (Ref. 51), Microwave power Engineering (Vol. II)
pp28-37 1968.
- 39 Johnston, D.A., Bibliography II Microwave plasmas,
JMP 5(1) pp17-22 and 5(3) pp192-197.(1970: 288 refs.)
- 40 Johnston, D.A. and Voss, W.A.G., "Use of the TEM Mode in Microwave
Heating Applicators", Paper 8.4 IMPI Symposium Monterey, May 1971
and IEEE Trans. MTT 20(8) pp547-548 (Aug. 1972).
- 41 Jull, E.V., Bleackley, W.J., and Steen, M.M., "The Design of
Waveguides with Symmetrically Placed Double Ridges", IEEE Trans.
MTT 17(7) pp397-399 (July 1969).
- 42 Jurgensen, P., "Fringing Field Applicators", Paper 8.2, IMPI
Symposium (Monterey, Cal. May 25, 1971).
- 43 Kretzschmar, J.G. and Pietermaat, F.P., "Concentrated Heating in
Elliptical Waveguides", JMP 6(3) pp207-211 (Oct. 1971).

- 44 Levine, H. and Moore, R.L., "Microwave Oven Test Load Evaluation and Determination of Internal Microwave Energy Distribution", US Dept. HEW Publication BRH/DEP 70-23 (Aug. 1970).
- 45 de Loor, G.P., "Dielectric Properties of Heterogeneous Mixtures Containing Water", JMP 3(2) pp67-73 (July 1968).
- 46 McConnel, D.R., Foerstner, R.A., and Bucksbaum, A.M., "A Dielectric Filled Inserted Choke Seal for the Microwave Oven", JMP 5(3) pp183-187 (Nov. 1970).
- 47 Metcalf, W.S., "Characteristic Impedance of Rectangular Transmission Lines", Proc. IEEE 112 (11) p2033 (Nov. 1965).
- 48 Metcalf, W.S., "Why Not Use Rectangular Coax?" Microwaves, April 1968.
- 49 Mobley, M.C., "FCC Equipment Type Approval Program with Reference to Microwave Oven Tests", JMP 6(4) pp297-303 (Dec. 1971).
- 50 Nielsen, E.D., "Scattering by a Cylindrical Post of Complex Permittivity in a Waveguide" IEEE Trans. MTT 17(3) pp148-153 (March 1969).
- 51 Okress, E.C. (Ed.), Microwave Power Engineering, Volumes I and II, Academic Press 1968.
- 52 Piaser, B., "Microwave Oven Coupling Procedures", Engineering and Laboratory Report #468, Amperex Electronic Corporation, Hicksville, NY 1964.
- 53 Pohl, W.J., "Power Klystrons and Related Devices", in Okress (Ref. 51) Microwave Power Engineering (Vol. I) pp84-106 1969.
- 54 Puschner, H., Heating With Microwaves, Springer-Verlag 1966.

- 55 Rajotte, R., Voss, W.A.G., Dossetor, J.B., and Stiller, C.R., "Microwave Defreezing of Canine Kidneys", IMPI Symposium, Ottawa, Canada, May 1972, paper 10.3
- 56 Ramo, S., Whinnery, J.R. and VanDuzer, T., Fields and Waves in Communication Electronics, John Wiley, 1965.
- 57 Saxton, J.A., "Dielectric Dispersion in Pure Polar Liquids at Very High Radio Frequencies Pt. 2- Relation of Experimental Results to Theory" Proc. Roy. Soc. 213A p473 1952.
- 58 Seabron, L.C., and Coopersmith, L.W., "Results of the 1970 Microwave Oven Survey", US Dept. HEW Publication BRH/DEP 72-2 1971.
- 59 Stiefel, K.J., "Microwave Heating Apparatus", US Pat. 2,480,682 1949.
- 60 Silvester, P., and Cermak, I.A., "Analysis of Coaxial Line Discontinuities by Boundary Relaxation", IEEE Trans MTT 17(8) pp489-495 (August 1969).
- 61 Tinga, W.R., "Dielectric Properties of Douglas Fir at 2.45 GHz", JMP 4(3) pp162-164 (Oct.1969).
- 62 Tinga, W.R., Multiphase Dielectric Theory - Applied to Cellulose Mixtures, Ph. D. Thesis, University of Alberta, Fall 1969.
- 63 Tsandoulas, G.N., Temme, D.H. and Willwerth, F.G., "Longitudinal Section Mode Analysis of Dielectrically Loaded Rectangular Waveguides with Application to Phase Shifter Design" IEEE Trans. MTT MTT18(2) pp88-95 (Feb. 1970).
- 64 Valles, B., "A 2450 MHz Low Cost Magnetron for Consumer Use", JMP 6(4) pp313-320 (Dec. 1971).
- 65 VanKoughnett, A.L., "A Microwave Applicator for Filamentary Materials", JMP 7(1) pp17-22 (March 1972).

- 66 VanKoughnett, A.L. and Wyslouzil, W., "An Automatic Tuner for Resonant Microwave Heating Systems", JMP 6(1) pp25-30 (Mar. 1971).
- 67 Vartanian, P.H., Ayres, W.P. and Helgesson, A.L., "Propagation in Dielectric Slab Loaded Waveguide", IEEE Trans. MTT 6 pp215-222 (April 1958).
- 68 Von Hippel, A.R., Dielectric Materials and Applications, MIT 1954.
- 69 Voss, W.A.G., "Advances in the Use of Microwave Power" US Dept. HEW Seminar Paper 008, Feb. 1970.
- 70 Voss, W.A.G. and Tinga, W.R., "Materials Evaluation and Measurement Techniques", in Okress, Vol II (Ref. 51) pp189-199 1968.
- 71 Weast, R.C.(Ed.), Handbook of Chemistry and Physics (49th Ed.), p D110. Chemical Rubber Company 1968.
- 72 White, J.R., "Sealing of Plastics", in Okress (Ref. 51) Microwave Power Engineering Vol II, pp115-125 1968.
- 73 Williams, N.H. and Warner, H.C., "Moisture Levelling in Paper, Wood and Other Mixed Dielectric Sheets", JMP 1(3) pp73-80 (1966) (Also in Okress, Vol II (Ref 51) pp175-188.)
- 74 Williams, N.H., "Curing Epoxy Resin Impregnated Pipe at 2450 MHz", JMP 2(4) pp123-127 (Nov. 1967).
- 75 Zahn, C.T. and Schweitzer, J.R., "Excitation and Separation of High Order Modes in Large High-Q Cavities", J. App. Phys. 27(8) pp929-937 (Aug. 1956).

APPENDIX ILIMIT OF VALIDITY OF THE PERTURBATION ANALYSIS

In the first four chapters of this thesis it was assumed that the electric fields existing in the empty applicator would be the same as those in the loaded structure. This is an example of the perturbation method, which Chatterjee and Chatterjee⁽¹³⁾ present by eigenfunction expansions and Altman⁽²⁾ by vector products. A perturbation term may be added to the solution of a known case, which must differ only slightly from the actual situation. The new term may then be obtained by using the original solution functions with the new boundary conditions.

The variational method⁽¹³⁾ is an alternative approximate method. Here the values of certain integrals are known to be stationary. The calculus of variations is used to find solution equations which guarantee this. In electrostatic systems one of these stationary integrals is the potential energy, and in this appendix the change in the potential energy will be used to see if a perturbation is small.

In an inhomogeneously loaded waveguide the TE, TM and TEM modes do not propagate. For small perturbations new modes exist which resemble these modes. Some may be classified as LSE(longitudinal section electric), where the electric fields are parallel to the web boundaries, and LSM modes where the magnetic fields are parallel to the web boundaries⁽⁶³⁾. Mixed modes also exist. A small dielectric perturbation will leave the electric fields nearly unchanged in the LSE modes and the electric flux \hat{D} unchanged in LSM modes⁽²¹⁾.

The energy in a wave in free space travels faster than in the dielectric portion of a loaded applicator. As a result, the energy is refracted at interfaces. In the dielectric, waves approaching the interface at an angle of incidence greater than the critical angle⁽⁶⁹⁾ will be totally internally reflected, with non-propagating fringing fields outside the dielectric decaying exponentially with distance⁽²⁵⁾. For lightly loaded rectangular structures Vartanian et al⁽⁶⁷⁾ found that the electric fields of the LSE modes were nearly the same as the sinusoidally distributed fields of the TE modes of the empty waveguide. As the amount of dielectric increased, the distribution in the free space portion of the structure at first became linear and then exponential. In other words the perturbing element is the web in lightly loaded rectangular waveguides while for a heavily enough loaded structure the web carries a dielectric mode which is perturbed by the metal waveguide in the fringing fields.

If the empty applicator fields predict that a large fraction of the power is carried in the web, the perturbation is too heavy⁽⁷⁰⁾. However, this does not imply that the resulting energy integral is equally far from the actual (stationary) value. For LSE modes ξ is higher than predicted, but the perturbed dielectric mode may be quite similar and the accuracy may still be good. Thus the error criterion that follows is conservative.

$$\text{Let } \xi^2 = \lim_{\Delta S \rightarrow 0} \frac{S}{\Delta S} \frac{\int_{\Delta S} \hat{E} \cdot \hat{E}^* dS}{\int_{\Delta S} \hat{E} \cdot \hat{E}^* dS} \quad (\text{A1.1})$$

where the electric fields are determined in the empty applicator. The electric energy stored in the electric fields in one meter of the web is

$$N_{\text{web}} = \frac{1}{2} \epsilon_0 \epsilon_r' \int_{\Delta S} \hat{E} \cdot \hat{E}^* dS \quad (\text{A1.2a})$$

The energy stored in the rest of the structure, $S-\Delta S$, is given by

$$N_{\text{app}} = \frac{1}{2} \epsilon_0 \int_{S-\Delta S} \hat{E} \cdot \hat{E}^* dS \quad (\text{A1.2b})$$

Let the perturbed electric fields be given by $k\hat{E}$, where the perturbed field distribution differs from the original fields only by a constant. If the web is parallel to the original fields, the total energy in the perturbed fields is given by

$$N_{\text{total}} = k^2 \frac{1}{2} \epsilon_0 \left[\int_S \hat{E} \cdot \hat{E}^* dS + (\epsilon_r' - 1) \int_{\Delta S} \hat{E} \cdot \hat{E}^* dS \right] \quad (\text{A1.3a})$$

Assuming that no energy has been lost in launching the wave, the original total energy is given by

$$N_{\text{total}} = \frac{1}{2} \epsilon_0 \int_S \hat{E} \cdot \hat{E}^* dS \quad (\text{A1.3b})$$

Then, for a web thin enough so that the electric field is constant inside it, we may equate A1.3a and A1.3b and solve for k in terms of ξ . This gives

$$k = \frac{1}{\sqrt{1 + \xi^2 F (\epsilon_r' - 1)}} \quad (\text{A1.4})$$

In the resulting value of k is nearly unity, we may assume that the analysis is valid. If for example, the value of k is less than 0.707, the perturbation analysis predicts that less than half of the power will be transported in the web fields. The actual value will, however, be more and the error is large. In the TE_{10} mode in a

rectangular waveguide, $\xi^2 = 2$. For a web consisting mainly of water, $\xi^2 F$ should be less than 0.012. Hence for a WR284 waveguide, this analysis is limited to soaked webs up to 0.018" thick.

This simple test applies if the surface of the web is parallel to the unperturbed electric field vectors. For the perpendicular case,

$$k = \frac{1}{\sqrt{1 + \xi^2 F \left(\frac{1}{\epsilon_r} - 1 \right)}} \quad (\text{A1.5})$$

which again should be nearly unity for the perturbation analysis to be valid. In either case, if excessive error is predicted, the solution can be obtained by other methods⁽¹³⁾.

APPENDIX II
THE TWIN-LINE APPLICATOR

In Chapter 2 the circular coaxial line was examined and a closely related rectangular structure was analyzed. This has also been done with the familiar twin-line, and the results are given in this appendix. In contrast to coaxial structures, twin-line structures do not give a levelling effect; the wetter spots are heated less. In twin-line applicators the attenuation can also be rather low.

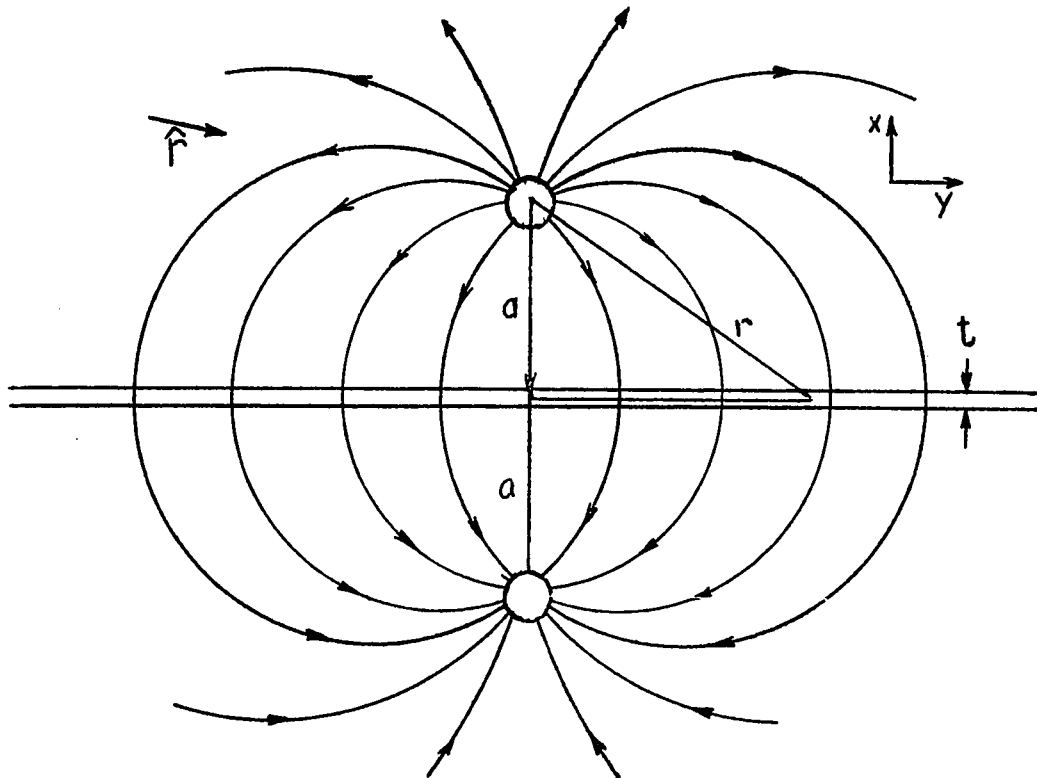


Figure A2.1

Twin-Line Applicator

To provide mixed boundary conditions, the web may be placed at an angle in the applicator. This would mean that the electric field in the web would be only partially shielded by the surface charge and the attenuation would increase with the angle of the web. This has been confirmed by experiment.

Twin-line is similar to single wire waveguides⁽²⁵⁾ in that its fringing fields extend far from the conductors but are non-radiating like near fields. Most of the energy is carried between the conductors, and a lossy dielectric placed in this region will experience heating. The boundary conditions for the electric field in the web of Figure A2.1 placed along one plane of symmetry are not the same as for the webs in the applicators in Chapter 2. The electric fields are incident perpendicular to the web and the \hat{D} vector is continuous across the interface.

Examining Figure A2.1, the power absorbed may be determined as a function of web thickness t' and spacing $2a$. Assuming a line charge of magnitude q coulombs/meter, the field \hat{E} at a distance r is given by electrostatic theory;

$$\hat{E} = \frac{-q}{2\pi\epsilon} \hat{r} \left(\frac{1}{r}\right) \quad (A2.1)$$

In the absence of the web, the magnitude of the transverse electric field at this plane of symmetry is given by

$$|E_y| = \frac{q}{\pi\epsilon} \left(\frac{a}{r^2}\right) \quad (\text{A1.2})$$

where $r = \sqrt{a^2 + y^2}$. Adding the web to the system, and assuming that it causes only a small perturbation, the normal $\hat{D} = \epsilon\hat{E}$ is nearly unchanged and is continuous across the interface. The power absorbed per unit length is given by:

$$P_{\text{web}} = \omega\epsilon_0\epsilon_r'' \int_{\text{vol.}} \hat{E}^* \cdot \hat{E} \, dV \quad (\text{A2.3})$$

$$\omega\epsilon_0\epsilon_r'' t' \int_{-\infty}^{\infty} \left(\frac{D}{\epsilon}\right)^2 dy \quad (\text{A2.4})$$

The boundary condition implies

$$\begin{aligned} P_{\text{web}} &= \omega\epsilon_0\epsilon_r'' t' 2 \int_0^{\infty} \left(\frac{q}{\pi\epsilon}\right)^2 \frac{a^2}{(a^2+y^2)^2} dy \\ &= \omega \left(\frac{\epsilon_0}{\epsilon}\right) \epsilon_r'' \left(\frac{t}{\pi a}\right) q^2 \end{aligned} \quad (\text{A2.5})$$

The characteristic impedance of the unloaded twin-line is given by

$$Z_0 = 1/\underline{C} \quad (\text{A2.6})$$

where \underline{C} , the capacitance per unit length, is

$$\underline{C} = \frac{\pi\epsilon_0}{\cosh^{-1}\left(\frac{2a}{R}\right)} \quad (\text{A2.7})$$

and R is the radius of the conductors. For $R \ll 2a$, $\cosh^{-1}(2a/R)$ behaves as $\ln(2a/R)$, and changes in a affect the values of q negligibly for constant transmitted power. The power carried by

the structure is

$$P_f = \frac{\phi^2}{Z_0} \quad (\text{A2.8})$$

at ϕ volts and the charges are given by

$$q = \phi C \quad (\text{A2.9})$$

Solving for power attenuation at 1 volt between the conductors,

$$2\alpha = \frac{P_{web}}{P_f} = \omega \left(\frac{\epsilon_0}{2} \right) \epsilon_r'' \left(\frac{t'}{2\pi a} \right) Z_0 C^2 \quad (\text{A2.10})$$

or,

$$\alpha = \left(\frac{\epsilon_r \epsilon_0}{2} \right) \omega \left(\frac{t'}{4\pi a} \right) \left(\frac{\pi \epsilon_0}{C} \right) \text{Cosh}^{-1} \left(\frac{2a}{R} \right)$$

or,

$$\alpha = \frac{1}{4\pi} \frac{\omega \epsilon_r}{C} \left(\frac{\epsilon_0}{\epsilon} \right)^2 \left(\frac{t'}{2a} \right) \text{Cosh}^{-1} \left(\frac{2a}{R} \right) \quad (\text{A2.11})$$

For constant Z_0 , this permits attenuation control through control of (t'/a) .

The power drops away rather rapidly as one moves away from the applicator. If P_{\max} is the maximum obtainable power absorption per square meter,

$$\frac{P}{P_{\max}} = \frac{E_y^2}{E_{m_y}^2} = \frac{a^4}{(a^2 + y^2)^2} \quad (\text{A2.12})$$

This function is plotted in Figure A2.2. The power concentration and non-radiating geometry permit the use of this structure as a television transmission line, but at high power, this unshielded line is unsafe.

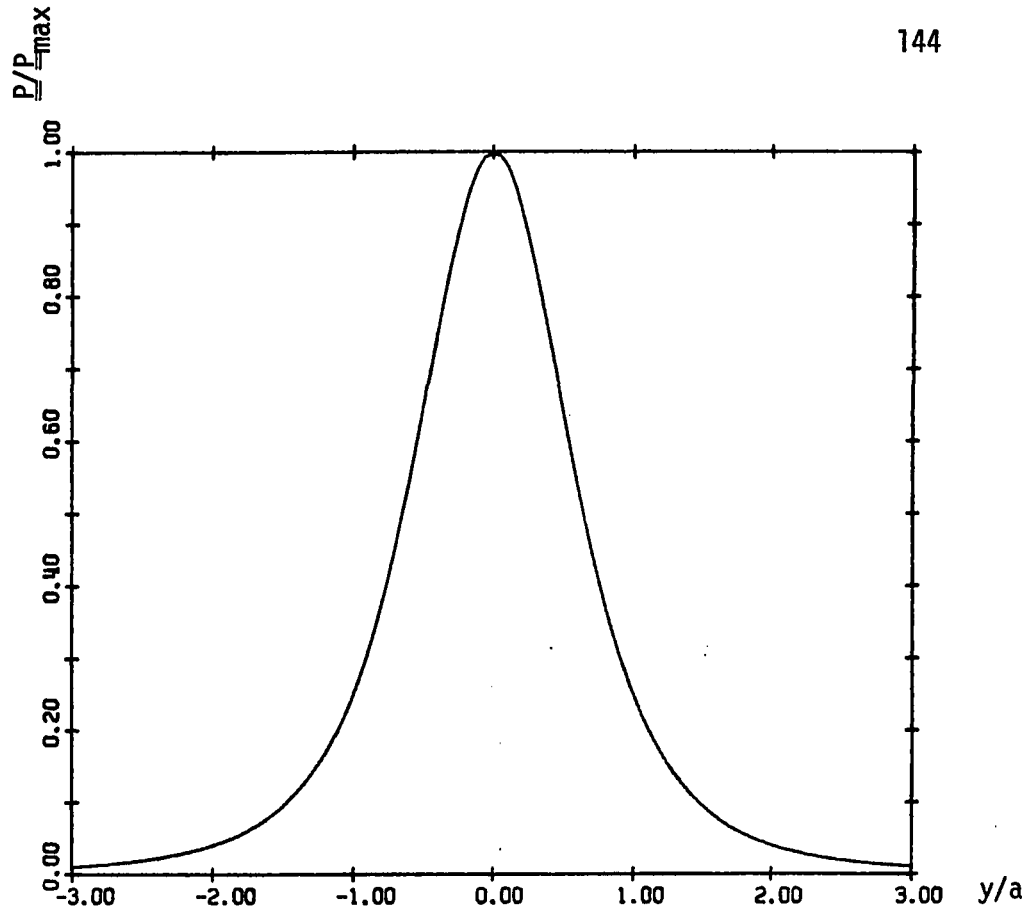


Figure A2.2 Twin-line Power Concentration Effect

The simple cylindrical twin-line gives attenuation control which is as sensitive to (t'/a) as the rectangular coaxial structure is to t/c . It does not have the effect of concentrating energy in a region away from the web, and indeed all flux lines must pass through the web. (ϵ^2 and F are meaningless here where the regions are infinite.) To control web field strengths we may use the walls of the applicator as shown in Figure A2.3. This has the advantage that Z_0 is more sensitive to b than a . To prevent much change in Z_0 we must move the walls as we adjust a , or else change w to compensate for this effect. For w/b large, Z_0 is proportional to $\sqrt{b/w}$.

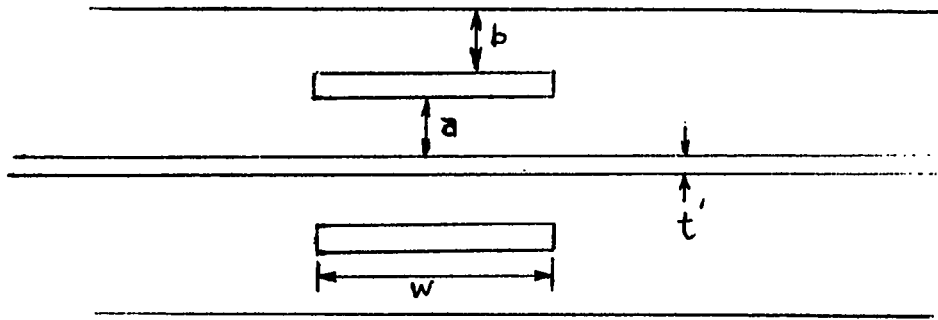


Figure A2.3 Shielded Twin-Line Structure

A simple twin-line applicator was built as shown in Figure A2.4. The characteristic impedance was set to 200 ohms to facilitate matching to a 50 ohm measurement system. A tee was connected to the input, one conductor and a section of line. This line was a phase inverter connecting to the other conductor. At frequencies where it was $n/2$ wavelengths long the desired mode was launched. A moving detector measured the amplitude of the electric fields in the vicinity of the conductors. Water and ethyl alcohol were poured into specially constructed glass tanks 1/8" and 1" wide. No detectable attenuation was observed and indeed the water helped to balance the line and reduce radiation.

Equation A2.11 predicts this very low attenuation, and shows that the applicator must not be used where ϵ_r' is high. Furthermore, it shows that spots with low ϵ_r' are selectively heated and these are the already dry areas. Due to the continuity of \hat{D}_m the wet spots dry more slowly. This is the exact opposite to the desired levelling effect.

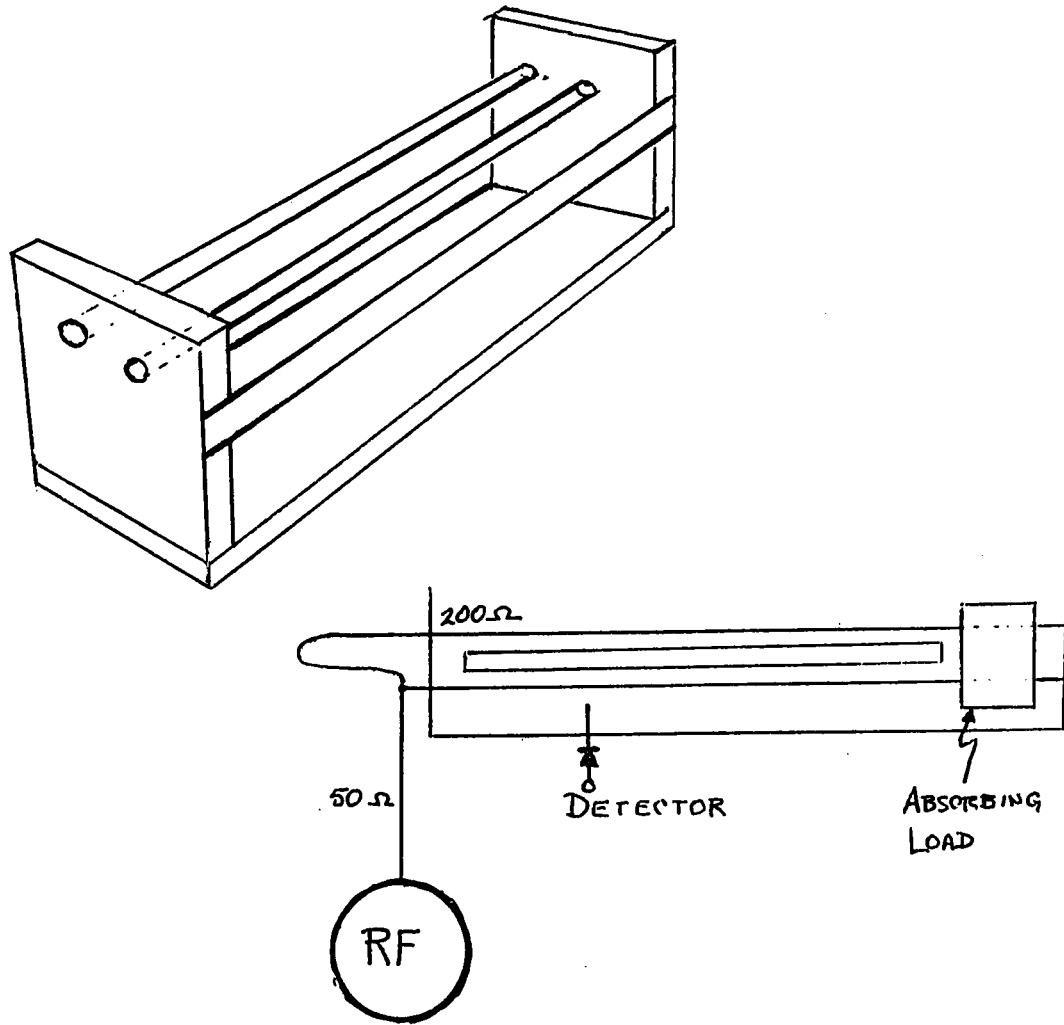


Figure A2.4 Test Setup for Twin-line Applicator

APPENDIX III

CORRECTION FOR LINE CHARGE APPROXIMATION

In Chapter 3, if two strips of charge are adjacent, the error in approximating them by line charges may be significant. A correction term for Eq. 3.10 can be derived as follows.

The voltage for a nearby strip of charge of density σ can be evaluated for a length $\pm c$, giving

$$\phi = \frac{\sigma}{2\pi\epsilon_0} \int_0^c \{ \ln(\sqrt{z^2 + a_2^2} + a_2) - \ln(\sqrt{z^2 + a_1^2} + a_1) \} dz \quad (A3.1)$$

where the voltage is evaluated at $y = 0$ and $c \rightarrow \infty$. It can be shown that

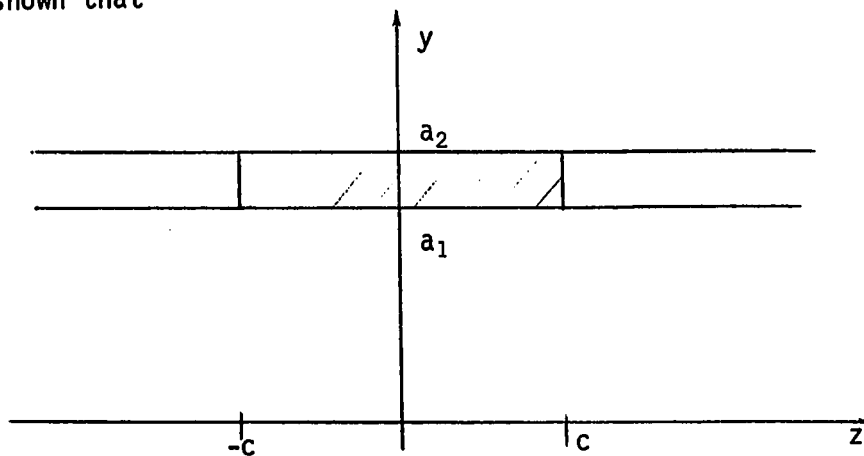


Figure A3.1 Potential Due to a Strip of Charge

$$\int_0^c \ln(\sqrt{x+a} + a) dx = c \sinh^{-1} \left(\frac{a}{c} \right) + c(\ln\{c\} - 1) \\ + a(\ln|c + \sqrt{a^2 + c^2}| - \ln\{a\} - 1) \quad (A3.2)$$

Then

$$\begin{aligned} \phi = \frac{\sigma}{2\pi\epsilon} \{ & a_1 \ln a_1 + a_2 \ln(c + \sqrt{a_2^2 + c^2}) - a_2 \ln a_2 \\ & - a_1 \ln(c + \sqrt{a_1^2 + c^2}) - (a_2 - a_1) \\ & + c \operatorname{Sinh}^{-1}\left(\frac{a_2}{c}\right) - c \operatorname{Sinh}^{-1}\left(\frac{a_1}{c}\right) \end{aligned} \quad (\text{A3.3})$$

Subtracting the approximate value given by Eq. 3.8 and taking limits, we obtain

$$F_2 = \left\{ 1 + \left(\frac{a_1 \ln(a_1) - a_2 \ln(a_2)}{a_2 - a_1} \right) + \ln\left(\frac{a_1 + a_2}{2}\right) \right\} \quad (\text{A3.4})$$

where F_2 is the correction term in Eq. 3.8, i.e.

$$\phi = \frac{\sigma w}{2\pi\epsilon} \lim_{c \rightarrow \infty} \left\{ F_2 + \ln\left(\frac{c + \sqrt{r^2 + c^2}}{r}\right) \right\} \quad (\text{A3.5})$$

and $r = (a_1 + a_2)/2$ and $w = (a_2 - a_1)$. For a set of strips of equal width, the corrections to Eq. 3.8 are given in Table 3.1, where $n = 1$ for adjacent strips, 2 for the next further away, etc. The correction $F_2/2\pi\epsilon$ must be added to L_{ij} for adjacent strips (but not their images). When this was done, Z_0 was only changed by 0.5%.

Table A3.1		Correction for Strip Width			
n	1	2	3	4	
F ₂	0.0452287	0.0106180	0.0046687	0.0026165	
n	5	6	7	8	
F ₂	0.0016717	0.0011598	0.0008516	0.0006518	
n	9	10	11	12	
F ₂	0.0005149	0.0004170	0.0003446	0.0002895	
n	13	14	15	16	
F ₂	0.0002467	0.0002127	0.0001852	0.0001628	